

Numerical investigation of strengthening mechanisms in metallic heterostructured materials

Shuai Zhu
Cardiff University
School of Engineering



**A thesis submitted for the degree of Doctor of Philosophy
December 2024**

Abstract

Metallic heterostructured materials (HSMs) are composed of multiple heterogeneous zones. These zones can be made of various phases of the same constituent metallic element with different grain sizes or can consist of different metals. Through the suitable design and synergistic integration of various phases/metallic compositions, HSM components can be developed to exhibit beneficial and tailored structural and functional properties at predetermined locations, such as an enhanced balance of strength and ductility, higher wear and corrosion resistance, higher thermal conductivity and reduced coefficient of friction. While such advanced structural configurations have been shown to be beneficial in numerous scientific reports and heterogeneous deformation has been widely proven to provide extra strengthening in heterostructured metallic materials, the explicit modelling of underlying plasticity mechanisms for HSMs at both grain and sample levels remains a challenge for the scientific community.

In this context, the focus of this Thesis is on developing numerical frameworks to investigate the strengthening mechanisms and underlying damage evolution of HSMs. To start with, the research presented in Chapter 3 proposes a methodology to compute explicitly the plastic strain gradient value in real time at every simulation iteration within a three-dimension strain gradient modified Johnson-Cook (JC) computational framework to capture size effect. The advantages of this method are that 1) no calibration from experimental data is required, 2) it is intrinsically physically based, as not restricted to any material deformation scenarios, and 3) it provides practitioners with the means to extend existing continuum-based models for the simulation of material behaviour on the microscale when both size and strain rate effects are present. The proposed

approach was shown to agree well with experimental data reported in the literature on the deformation of microscale copper wires in both tension and torsion.

In Chapter 4, a novel 3D numerical framework for heterostructured laminates (HSLs) is proposed by considering the evolution of various types of dislocations and back stress while being coupled with the JC damage criterion. Overall, a good correlation between numerical and experimental results was achieved under indentation and uniaxial tensile loading scenarios. Through the evaluation of the damage accumulation factor, the simulation results yielded quantitative information which aligned with the following known experimental observations: 1) the smaller the layer thickness, then the smaller the internal damage and 2) the internal damage increases with the increase in volume content of the nanograined (NG) layer. For a set simulated strain of 10%, it was also shown that the damage accumulation factor in the NG layer was 10 times lower than that in its counterpart, i.e., a stand-alone NG layer not sandwiched between two coarse grained (CG) layers.

The research presented in Chapter 5 reports on the development and testing of a novel non-local crystal plasticity finite element model (CPFEM) to simulate the deformation of HSMs. This model explicitly includes geometrically necessary dislocations (GNDs), back stress hardening and damage criterion and does not rely on a homogenisation scheme. This approach enables the numerical investigation of dislocation-mediated plasticity simultaneously at both grain and sample levels. The model was validated against experimental data when simulating the deformation of a bi-layered high entropy alloy (HEA). The obtained results aligned well with experimental findings. In particular, the simulations confirmed that shear bands (SBs) preferably propagate along grains sharing similar orientation while causing severe damage and grain rotation.

In the last part of the thesis, presented in Chapter 6, the research investigated the strengthening mechanisms and fracture modes in HSLs through a full-field non-local CPFEM framework and incorporated progressive continuum damage

mechanics (CDM) model for crack initiation and propagation. The constitutive model was validated with simulated homogenous Twinning-Induced Plasticity (TWIP) steel and Maraging steel specimens before being applied to the TWIP/Maraging steel laminates. It was observed that the non-local CPFEM-CDM model based on maximum slip accurately captured the typical brittle and ductile damage of stand-alone Maraging and TWIP steels, respectively. It was further found that, when contained in a HSL configuration, the hard Maraging layer exhibited a fracture process of void nucleation, coalescence and propagation, hence displayed a brittle to ductile fracture trend, which is in stark contrast to the stand-alone Maraging layer where a typical brittle fracture was observed.

In summary, the modelling frameworks developed in this Thesis provide a solid theoretical framework for the future design of HSMs to achieve optimal strength-ductility balance and to predict potential crack nucleation sites and SBs evolution in such materials.

Contents

Abstract.....	2
Contents	5
List of Figures	11
List of Tables.....	17
List of Abbreviations	18
Nomenclature.....	19
List of Publications	22
Acknowledgements	23
Chapter 1 Introduction.....	1
1.1 Motivation.....	1
1.2 Research aims and objectives.....	2
1.3 Outline of the Thesis	3

Chapter 2 Literature review.....	5
2.1 The development of HSMs	5
2.2 Experimental investigations on HSMs	8
2.3 Numerical investigations on HSMs	10
2.3.1 Strain gradient plasticity	11
2.3.2 Molecular dynamics	15
2.3.3 Discrete dislocation dynamics	16
2.3.4 Crystal plasticity finite element method.....	17
2.3.5 Homogenized finite element method	19
2.3.6 Analytical modelling	10
2.4 Summary and knowledge gaps identified	21
Chapter 3 Development of a 3D strain gradient modified Johnson-Cook computational framework	24
3.1 Introduction.....	24
3.2 Constitutive relations and FEM modelling	24
3.2.1 Mechanism-based SGP modified JC constitutive model	24
3.2.2 Methodology for the explicit calculation of the plastic strain gradient.....	26
3.2.3 Finite element model set-up	28

3.3 Results and discussion.....	30
3.3.1 Size effect.....	30
3.3.2 Strain rate effect.....	33
3.3.3 Respective contribution of the size effect and the strain rate effect	37
3.4 Conclusion.....	38
Chapter 4 Development of a multiple mechanism based constitutive model coupled with damage criterion for investigating the deformation of HSLs	40
4.1 Introduction.....	40
4.2 Numerical framework and FEM model.....	41
4.2.1 Multiple mechanisms based constitutive model.....	41
4.2.2 Constitutive model for homogenous layers.....	42
4.2.3 Constitutive model for interface affected zones (IAZs)	45
4.2.4 Johnson Cook failure criterion	46
4.2.5 Implementation and finite element modelling.....	47
4.3 Results and discussion.....	50
4.3.1 Microhardness simulation on standalone homogeneous grained layers.....	50

4.3.2 Uniaxial tensile responses of standalone homogenous NG and CG copper layers.....	51
4.3.3 Quantitative analysis of uniaxial tensile responses of standalone IF.....	54
4.3.4 Uniaxial tensile response of HSLs	58
4.4 Conclusions	69
Chapter 5 A full-field non-local crystal plasticity investigation of bi-layered HEA.....	72
5.1 Introduction.....	72
5.2 Numerical framework and FEM model.....	72
5.2.1 CPFEM constitutive model.....	72
5.2.2 GND calculation.....	74
5.2.3 Back stress model.....	75
5.2.4 Damage model.....	77
5.2.5 Model implementation.....	77
5.3 Uniaxial tensile response of homogeneous HEA specimens	79
5.3.1 CPFEM modelling.....	79
5.3.2 Validation of the constitutive model and parameter calibration	82
5.3.3 Grain size effect	82

5.4 Uniaxial tensile response of a bi-layered HEA specimen.....	87
5.4.1 Finite element model	87
5.4.2 Uniaxial tensile response	89
5.5 Conclusions	101
Chapter 6 Numerical study on the strengthening and fracture characteristics of heterogeneous-structured TWIP/Maraging steel laminates using a non-local crystal plasticity and continuum damage mechanic model	104
6.1 Introduction.....	104
6.2 Constitutive relations and modelling framework	105
6.2.1 Overview	105
6.2.2 CPFEM-CDM modelling of steel phases	106
6.2.3 Model implementation for uniaxial tensile tests on TWIP/Maraging steel laminates	108
6.2.4 Determination of model parameters and validation with standalone steel specimens.....	110
6.3 Results and discussion for the simulated HSL specimen.....	115
6.3.1 Stress-strain response	115
6.3.2 Stress partition and GND distribution.....	117
6.3.3 Shear band and fracture formation	119

6.4 Conclusions	123
Chapter 7 Conclusions and Future Work	125
7.1 Conclusions	125
7.2 Future work.....	128
Appendix: mesh convergence	132
Bibliography.....	133

List of Figures

Figure 2.1: Structural and chemical gradients in typical metals and alloys. Structural gradients involve gradients in grain size, lamellar thickness, and twin thickness. Chemical gradients involve gradients in phase, chemical composition, and precipitate. Both structural and chemical gradients can coexist (Ji et al., 2023). 6

.....

Figure 3.1: Flow chart of the MSGP-modified JC algorithm. 28

Figure 3.2: (a) Schematic illustration of one of the simulated dog-bone-shaped specimens (diameter of 30 μm in tension), (b) FE model and meshing of the specimen in torsion, (c) typical stress distribution during torsion simulation. 29

Figure 3.3: (a) Stress-strain curves under quasi static strain rate for copper wires in tension with diameters of 18 μm , 30 μm 42 μm and 105 μm , (b) Plots of normalized torque-twist curves for copper wires with diameters of 18 μm , 30 μm 42 μm and 105 μm . The simulated results are plotted with solid lines and experimental data..... 32

Figure 3.4: (a) Stress-strain curves for copper wires in tension with diameters of 18 μm , 30 μm 42 μm and 105 μm under the strain rate of 100 s^{-1} (dashed lines) and 1000 s^{-1} (solid lines), (b) Plots of normalized torque-twist curves for copper wires with diameters of 18 μm , 30 μm 42 μm and 105 μm under the strain rate of 100 s^{-1} (dashed lines) and 1000 s^{-1} (solid lines)..... 34

Figure 3.5: Simulated final yield stress data (for a strain of 0.1 in tension and a surface shear strain of 0.19 in torsion) for copper wires with diameters of 18 μm , 30 μm 42 μm and 105 μm under quasi-static strain rate (dot marker), and strain rate values of 100 s^{-1} (cube markers) and 1000 s^{-1} (tetrahedron markers)..... 36

Figure 3.7: Relative contributions of size and strain rate effects to the increase in the flow stress value for different copper wire diameters. The plotted increase

in flow stress was obtained by comparing the simulated data against a baseline simulation scenario defined as that using the classical JC method under quasi-static strain rate..... 38

.....

Figure 4.1: (a) Schematic diagram of the modelled tensile dog-bone specimen; (b) layers of the integrated FEM model with a NG volume content of 10 %; (c) schematic of piled-up GNDs near the boundaries of NG and CG layer; (d) schematic of the various dislocations considered in the presented work. 41

Figure 4.2: Flow chart of the developed 3D multiple physical mechanisms algorithm. 48

Figure 4.3: (a) FEM model of indentation; (b) detailed Berkovich indenter with consideration of tip bluntness 49

Figure 4.4: (a) Simulated reaction force-displacement curves during indentation and (b) comparison between numerical and experimental microhardness values for homogenous-grained CG and NG copper. 51

Figure 4.5: Simulated and experimental (a) true stress-true strain curves (b) back stress-true strain for homogenous-grained copper with grain sizes of 100 nm, 4 μm and 4.8 μm and for the IAZ..... 53

Figure 4.6: Specimen deformation and corresponding JC damage accumulation factor (i.e., SDV 24) at 10% tensile strain for homogenous copper layers with grain size of (a) 100 nm (b) 4 μm and (c) 4.8 μm using..... 54

Figure 4.7: The predicted curves of (a) stress-strain and (b) back stress-plastic strain for homogeneously grained IF-steel with the grain size varies from 0.096 μm -35 μm 56

Figure 4.8: The evolution of contribution from different factors to the flow stress of homogenous IF-steel with different grain sizes, (a) $d=35 \mu\text{m}$, (b) $d=0.096 \mu\text{m}$ 57

Figure 4.9: The contributions of different factors to the flow stress of homogenous IF-steel with different grain sizes..... 58

Figure 4.10: Plots of simulated stress-strain curves using modified ROM

method for copper-based HSL composites with different layer thicknesses against (a) experimental results from (C. X. Huang et al., 2018) and (b) ROM predictions from (Zhao, Zaiser, et al., 2021)..... 59

Figure 4.11: Evolution of (a) back stress and (b) effective stress for the simulated copper-based HSLs with different layer thickness and comparison with experimental findings from (C. X. Huang et al., 2018). 62

Figure 4.12: Comparison of the results obtained between the modified ROM method predictions, ROM results from (Zhao, Zaiser, et al., 2021) and experimental results from (Ma et al., 2015) for laminates with different volume content of NG layer..... 63

Figure 4.13: (a) Plots of simulated stress-strain curves for copper-based HSLs using the integrated FE model with (a) different layer thicknesses against experimental results from (C. X. Huang et al., 2018) and (b) different NG volume contents against experimental results from (Ma et al., 2015) 65

Figure 4.14: (a) Comparisons of simulated lateral stress distribution of 10 % NG volume content of a copper-based HSL at the true strain of 0.5 % with numerical results presented in (Zhao, Zaiser, et al., 2021); (b) lateral stress distribution of simulated copper-based HSLs with different NG volume contents at the true strain of 0.5 %..... 66

Figure 4.15: (a) The simulated JC damage accumulation factor of the NG layer in HSLs with layers of different thicknesses, (b) The simulated JC damage accumulation factor of the NG layer in HSLs with 10 %, 22 % and 47 % NG volume content using the integrated FE model developed in this research. ... 68

.....

Figure 5.1: (a) RVE containing 32 randomly orientated grains generated using the Voronoi algorithm and boundary conditions adopted during the finite element simulations. Simulated (b) stress-strain curves and (c) GND densities for homogeneous polycrystals with grain sizes ranging from 5 μm to 100 μm . Results without GND hardening are also shown in (b). Contribution of (d) back stress hardening and (e) GND-induced isotropic hardening to the flow stress

for homogeneous specimens with grain sizes in the range of 5 μm to 100 μm	81
Figure 5.2: (a) Distribution of (a) the total GND density, (b) von Mises stress and (c) ϵ_y in the homogeneous grained HEA with grain size of 5 μm , 14 μm and 100 μm at a strain of 20%, (d) Example of experimental ϵ_y distribution on copper with a grain size of 4.8 μm	86
Figure 5.3: (a) Finite element model of the bi-layered specimen with different grain size, d , between both regions and adopted boundary conditions. Comparison of simulated and experimental engineering stress-strain curves for (b) as-cast and RA homogeneous HEA specimens; (c) bi-layered and stand-alone HEA regions 1 and 2. 4-LSP indicates four repetitions of the laser shock peening operation.	88
Figure 5.4: Distributions of (a) ϵ_x and (b) ϵ_y in the simulated bi-layered HEA at strains of 2%, 5%, 10%, 15% and 20%.	91
Figure 5.5: Distributions of local strain ϵ_x (thickness direction) on (a) "Path C" i.e., within region 1 along the tensile direction, and (b) "Path A" i.e., along the thickness of the specimen across both regions, for the simulated bi-layered HEA at different tensile strains. Distributions of local strain ϵ_y (loading direction) on (c) "Path C" i.e., within region 1 along the tensile direction, and (d) "Path A" i.e., along the thickness of the specimen across both regions, for the simulated bi-layered HEA at different tensile strains.	93
Figure 5.6: GND density in the modelled bi-layered HEA at a strain of 20% along (a) "Path A", and (b) "Path B". (c) Distributions of GNDs at strains of 2%, 5%, 10%, 15% and 20%. Simulated (d) von Mises stress along "Path A" for a strain of 20% and (e) distributions of von Mises stress at strains of 2%, 5%, 10%, 15% and 20% for the entire bi-layered HEA modelled.	96
Figure 5.7: Simulated distributions of back stress on the 12 slip systems in the modelled bi-layered HEA at a strain of 20%.	98
Figure 5.8: (a) Distribution of JC damage factor values for an applied strain of 20%; (b) a locally enlarged region composed of 5 grains with one of them	

displaying strong misalignment relative to the other four; evolution of (c) SBs and (d) damage within this region for strain values between 0.2 % and 20%; (e, f, g) crystal orientation within this region along the x, y and z direction, respectively, for an applied strain of 20%, and (h) accumulated slip, again for 20% strain. 101

.....
Figure 6.1: Overall framework of the developed non-local CPFEM-CDM model for the investigation of the fracture characteristics in TWIP/Maraging steel laminates..... 106

Figure 6.2: Finite element model of the TWIP/Maraging steel laminate and adopted boundary conditions. 110

Figure 6.3: Comparison of the obtained numerical stress-strain responses against corresponding experimental data from (Yu et al., 2024) for individual homogenous grained TWIP and Maraging steels. 112

Figure 6.4: Simulated deformation and von Mises stress for (a) TWIP steel and (b) Maraging steel as a function of the strain until fracture..... 114

Figure 6.5: Simulated fracture process and evolution of SB for (a) TWIP steel and (b) Maraging steel..... 115

Figure 6.6: Simulated stress-strain curve compared against the experimental data from (Yu et al., 2024) for the multilayer TWIP/Maraging steel HS. The inset figure shows the CDM damage factors of laminates at fracture..... 117

Figure 6.7: Simulated distribution of the von Mises stress for (a) the entire HSL specimen and (b) along "Path A"; simulated GND density for (c) the entire HSL specimen and (d) along "Path A". Both the von Mises stress and the GND density data are provided just before fracture, i.e. for a strain of 9.4 %. 118

Figure 6.8: Evolutions of ϵ_y i.e., shear bands, in the simulated TWIP/Maraging steel laminates at strains of (a) 1%, (b) 3%, (c) 5%, (d) 7%, (e) 9.6% and (f) ϵ_y profile for a strain of 9.6% along "Path A" 120

Figure 6.9: Distribution of CDM damage factor values at fracture for (a) the entire HSL specimen and (b) (b) along Path A; locally enlarged regions

displaying the evolution of cracks in the simulated TWIP/Maraging steel laminates for strain values between of (c)7 %, (d) 7.8%, (e) 9.4% and (f)9.6%.
..... 121

List of Tables

Table 3.1: Adopted unit system in ABAQUS.	29
Table 3.2: Material properties used in this Chapter.	30
.....	
Table 4.1: Material properties	49
.....	
Table 5.1: Material properties.	78
.....	
Table 6.1: Parameters of the CPFEM model for TWIP and Maraging steel...	111
Table 6.2: Parameters of the CDM model for TWIP and Maraging steel.....	111

List of Abbreviations

CDM	Continuum damage mechanics
CG	Coarse grained
CMSG	Conventional mechanism-based strain gradient
CPFEM	Crystal plasticity finite element method
CRSS	Critical resolved shear stress
DDD	Discrete dislocation dynamics
EBSD	Electron Backscatter Diffraction
FCC	Face centred cubic
GND	Geometrically necessary dislocations
GBs	Grain boundaries
HDI	Heterogeneous deformation-induced
HEA	High entropy alloy
HSLs	Heterogeneous-structured laminates
IAZs	Interface affected zones
ISE	Indentation size effect
JC	Johnson Cook
KME	Kocks-Mecking-Estrin
MD	Molecular dynamics
NG	Nanograined
PEEQ	Equivalent plastic strain
ROM	Rule of mixture method
RVEs	Representative volume elements
SBs	Shear bands
SEM	Scanning Electron Microscopy
SSD	Statistically stored dislocations
TWIP	Twinning-Induced Plasticity
UMAT	User-defined material subroutine

Nomenclature

σ_0	Lattice friction stress
M	Taylor factor
α	Material constant
G	Shear modulus
b	Magnitude of the Burgers vector
σ^b	Back stress
d	Grain size
ν	Poisson's ratio
N	Dislocation number within a pile-up
\dot{N}	The rate of change of dislocation number within a pile-up
N_Δ	Initial evolution rate of dislocation number within a pile-up
N^*	Saturated pile-up dislocation number
\dot{p}	Equivalent plastic strain rate
k_{HP}	Hall-Petch constant
λ	Distance between slip lines
ρ_{GNDs}^{sam}	Sample level GNDs density
ρ_{GNDs}^{gra}	Grain level GNDs density
\bar{r}	Nye's factor
η^p	Strain gradient
$\Delta\eta_{ijk}^p$	Strain gradient components
k_{mfp}^g	Geometric factor
k_{mfp}^{dis}	Proportional factor
$\dot{\epsilon}_{ref}$	Reference strain rate
d_{ref}	Reference grain size
k_{ann}	Dislocation annihilation factor
d_{NG}	Size of a nano grain

d_{CG}	Size of a coarse grain
$\Delta\sigma_0$	Difference of lattice friction stress between the NG and the CG layers
d_1 to d_5	Material damage parameters
γ	Stress triaxiality ratio
$\dot{\bar{\epsilon}}^{pl}$	Equivalent plastic strain rate
$\dot{\epsilon}_0$	Equivalent reference strain rate
T	Current temperature
T_r	Reference temperature
T_m	Material melting temperature
$\Delta\bar{\epsilon}_f^{pl}$	Incremental failure strain
H_i	Indentation hardness
F_N	Normal reaction force
A_p	Projected area
V_i	The volume fraction of component i
$\sigma'_{i,ys}$	Flow stress of component i alone at 0.2 % plastic strain of the composite sample
σ_i	True stress of component i
$\sigma_{i,UE}$	True stress of the sample at necking
$\epsilon_{i,UE}$	True strain of the sample at necking
$\sigma_{laminar}$	The stress of the laminate
V_{total}	Total volume of the integrated sample
σ_{CG}	Stress for the coarse-grained region
σ_{IAZ}	Stress for the interface-affected zone
σ_{NS}	Stress for the nano-grained region
V_{CG}	Stress for the coarse-grained region
V_{IAZ}	Stress for the interface-affected zone
V_{NG}	Stress for the nano-grained region
$\dot{\gamma}^a$	Shear strain rate
$\dot{\gamma}_0$	Reference shear rate

n	Power law exponent
τ^a	Shear stress acting on the slip system
τ_c^a	CRSS
$(\tau_c^a)^0$	Initial CRSS
τ_{for}^a	Forest dislocation interaction stress
τ_{sub}^a	Dislocation substructure interaction stress
k_1	Hardening constant
Δt	Step time increment
k_2	Annihilation constant
g^a	Effective activation enthalpy
D^a	Drag stress
ζ	Dislocation interaction parameter
G^a	Shear modulus
b^a	Magnitude of the Burgers vector
q	Rate coefficient
f^a	Fraction of recovery rate that leads to substructure formation
\mathbf{t}^b	Dislocation line direction
\mathbf{n}^a	Slip plane normal
\mathbf{s}^b	Slip direction
$\rho_{\Delta e}^\alpha$	Edge dislocations
$\rho_{\Delta s}^\alpha$	Screw dislocations
γ_m	Maximum shear strain, i.e., the maximum shear strain among all slip systems
D	Damage factor
D_{\max}	Maximum damage value
γ_{ini}	Maximum shear strain over which damage initiates
γ_{\max}	Maximum shear strain at which the damage value reaches the maximum value
\mathbf{H}_b^a	Slip hardening moduli

List of Publications

Journal Publications directly related to the work reported in the Thesis

- **Zhu S**, Brousseau E, Shao Y, Peng W. Numerical investigation of internal damage in heterogeneous-structured laminates using a 3D multiple physical mechanisms based constitutive model. *Composite Structures*. 2024;336.
- **Zhu S**, & Brousseau E. A full-field non-local crystal plasticity investigation of bi-layered HEA. *International Journal of Mechanical Science*. 2025;288.
- **Zhu S**, & Brousseau E. Numerical study on the fracture mode of heterogeneous-structured TWIP/Maraging steel laminates using a non-local crystal plasticity model. (Ready to submit).

Conference Publications

- **Zhu S** & Brousseau E. Slip system level strengthening in nano-indentation of single crystalline copper: Numerical study via a non-local CPFEM model, *MATEC Web of Conferences*, 401 (2024) 03005.
- **Zhu S** & Brousseau E. 2024. Numerical Investigation of Size Effects in Tension and Torsion of Micro-scale Copper Wires using a Strain Gradient Modified Johnson-Cook Constitutive Model. In: Spezi E. & Bray M (eds.), *Proceedings of the Cardiff University Engineering Research Conference 2023*. Cardiff: Cardiff University Press. DOI: <https://doi.org/10.18573/conf1.ap>
- **Zhu S** & Brousseau E. 2023. Development of a multiple mechanism based constitutive model coupled with damage criterion for investigating the deformation of polycrystalline steel with μm to sub- μm grain size. Presented at: World Congress on Micro and Nano Manufacturing - WCMNM 2023, Evanston, IL, U.S. 18-21 September 2023.

Acknowledgements

First and foremost, I would like to express my deepest gratitude to my supervisor, Professor Emmanuel Brousseau for his invaluable guidance, encouragement, and support throughout the course of my research. His expertise, patience, and unwavering belief in my abilities have been instrumental in the completion of this Thesis.

I am also deeply indebted to Prof Carol Featherston and Dr Zhangming Wu, whose continuous mentorship have helped me grow both personally and professionally. I wish to extend my heartfelt thanks to the school research/teaching and IT staff. Their involvement helped improve the rigor and clarity of my research.

Special thanks go to my colleagues and friends in the High Value Manufacturing group and office W.1.33 for their camaraderie, support, and helpful discussions. The collaborative atmosphere of the group has made my research journey more enriching and enjoyable.

I would like to acknowledge China Scholarship Council, taxpayers in China and Supercomputer Wales for providing the financial support and necessary resources and that allowed me to pursue this research. Lastly, I want to express my profound appreciation to my families and friends, for their constant love, patience, and encouragement. Their belief in me gave me the strength to persevere during this journey.

Chapter 1 Introduction

1.1 Motivation

Metallic HSMs consist of multiple zones of different metals or of various phases of the same constituent. These zones typically display different grain sizes and significant variation in their mechanical properties (Ji et al., 2023; Zhu & Wu, 2023). While conventional metallic materials can be engineered to exhibit some degree of heterogeneous microstructure, the distinguishing characteristic of HSMs lies in the significant synergistic effect that results from the interactive coupling of their heterogeneous zones. Heterostructured laminates (HSLs), gradient, bi-modal grain size distribution and metal matrix composite structures are examples of such class of materials (Zhu & Wu, 2023). The mechanical properties of metallic HSMs largely exceed those predicted by the rule-of-mixtures of the properties of individual constitutive zones (Zhu & Wu, 2023). Under load, such materials also exhibit important hetero-deformation induced (HDI) synergistic strengthening (Zhu & Wu, 2023). Many studies have revealed that GNDs are essential features of the micromechanics of HSMs subjected to various loading conditions (Fu, Huang, et al., 2022; Fu et al., 2023; Zhang, Zhao, et al., 2023). Heterostructures lead to strain partitioning between the harder and softer regions and in this case, an applied uniaxial strain is converted into multiaxial strains, activating multiple slip systems and encouraging dislocation hardening. SBs are also considered as an important feature of strain localisation in heterostructures (Chen & Li, 2021; Wang, Huang, Li, Guo, et al., 2020; Wang, Huang, Li, Fang, et al., 2020). The microstructure of such materials dominates the deformation mechanisms and the resulting macroscopic mechanical response (Zhu & Wu, 2023).

For this reason, understanding the deformation mechanisms at play and their

contribution on the microstructural level is key to correlating microstructure with mechanical properties. However, existing investigations towards this endeavour have been mostly experimental and primarily focussed on the processing and macroscopic mechanical behaviour of HSMs (Fu, Li, et al., 2022). Thus, it is contended that complementary simulations and theoretical investigations are essential to advance the understanding of underlying microscopic mechanisms, particularly to discern the influence of distinct hardening effects, as these phenomena are not readily isolatable or observable through experimental approaches alone.

All motivations behind the work reported in this Thesis are ultimately focussed on investigating the deformation characteristics of HSMs where size effect, dislocations, SBs play dominant roles.

1.2 Research aims and objectives

As introduced above, this Thesis proposes to develop computational frameworks on different length scale for conducting a number of numerical simulations, i.e. mechanism-based strain gradient plasticity (MSGP), FEM, CPFEM, on metallic HSMs with the overall aim to investigate the sources of strengthening of HSMs. The specific objectives of this research include:

- I. To numerically study the size effect existing in the uniaxial tensile experiments of microscale copper wires with a view to provide the micro-machining community with a numerical tool for the prediction of size effect.
- II. To quantitatively investigate the contribution of strengthening mechanisms and explore the effect of layer thickness and NG volume fraction on the strengthening of copper laminates.
- III. To investigate the non-local CPFEM as a numerical method to explore underlying mechanisms responsible for strengthening of bi-layered HEA.

-
- IV. To investigate the fracture characteristics of HSLs, and also to investigate associated deformation mechanisms induced by heterogeneous deformation via a non-local CPFEM-CDM model.

1.3 Outline of the Thesis

The remaining Chapters of this Thesis are organised as follow:

Chapter 2: This Chapter reviews the relevant literatures about the development of HSMs, especially computational efforts. The use of numerical methods, i.e. molecular dynamics (MD), discrete dislocation dynamics (DDD), CPFEM, homogenized FEM and analytical methods for the investigation of HSMs to promote their optimization and applications are also discussed. Finally, several knowledge gaps in the specific field of numerical modelling of HSMs are presented.

Chapter 3: This Chapter addresses the first objective of the work by investigating the uniaxial tensile response of microscale copper. A mechanism strain gradient plasticity (MSGP)-modified JC model is developed to predict the size effect within the material, including strain rate effect.

Chapter 4: This Chapter addresses the second objective, focusing on the study of the strengthening mechanisms of copper laminates. The contribution of different mechanisms to the strengthening is quantified and discussed first. Importantly, the mechanisms driving the strengthening of copper laminates are discussed based on the developed multiple mechanisms based numerical framework. In addition, the effect of layer thickness and NG volume fraction are investigated.

Chapter 5: This Chapter addresses the third objective. It reports the investigation into the response of bi-layered HEA fabricated via laser shock peening (LSP) with the considered mechanisms including size effect. This Chapter also discusses the interactions between grain misorientations, GNDs, SBs and damage.

Chapter 6: This Chapter addresses the last objective. It presents a numerical study investigating the influence of strengthening mechanisms on the fracture characteristics of TWIP/Maraging steel laminates, namely GNDs, stress partitioning, and shear banding behaviour.

Chapter 7: This Chapter provides a comprehensive summary of the key conclusions and contributions of this Thesis, emphasizing its significance within the broader research context. Additionally, it offers recommendations for future work, aims at advancing the field and addressing the limitations identified in this study.

Chapter 2 Literature review

To achieve the research objectives outlined in Chapter 1, a comprehensive understanding of various research domains is essential. These include the fundamental characteristics of HSMs, the integration of MSGP and JC models, as well as the numerical modelling of HSMs. Consequently, this Chapter presents a detailed review of the existing literatures on HSMs, focusing on the application of numerical methods to explore the underlying strengthening mechanisms.

The Chapter begins by discussing the development of HSMs, with a particular emphasis on HSLs. It then examines the numerical investigation of HSMs using various methods across multiple length scales, including MD, DDD, CPFEM. Finally, the Chapter identifies key knowledge gaps, specifically in the application of numerical techniques for elucidating the strengthening mechanisms of HSMs.

2.1 The development of HSMs

Examples of metallic HSMs include heterogeneous structured laminates (HSLs), gradient, bi-modal grain size distribution and metal matrix composite structures as shown in Figure 2.1. Importantly, such zones display significant differences in their respective mechanical or physical properties (Ji et al., 2023; Zhu & Wu, 2023). While it is well-known that conventional metallic materials can be engineered to exhibit some degree of heterogeneous microstructure, the distinguishing characteristic of HSMs lies in the significant synergistic effect that results from the interactive coupling of their heterogeneous zones. This effect is significant in the sense that the mechanical or physical properties of metallic HSMs largely exceed those predicted by the rule-of-mixtures (ROM) of the properties of the individual constitutive zones.

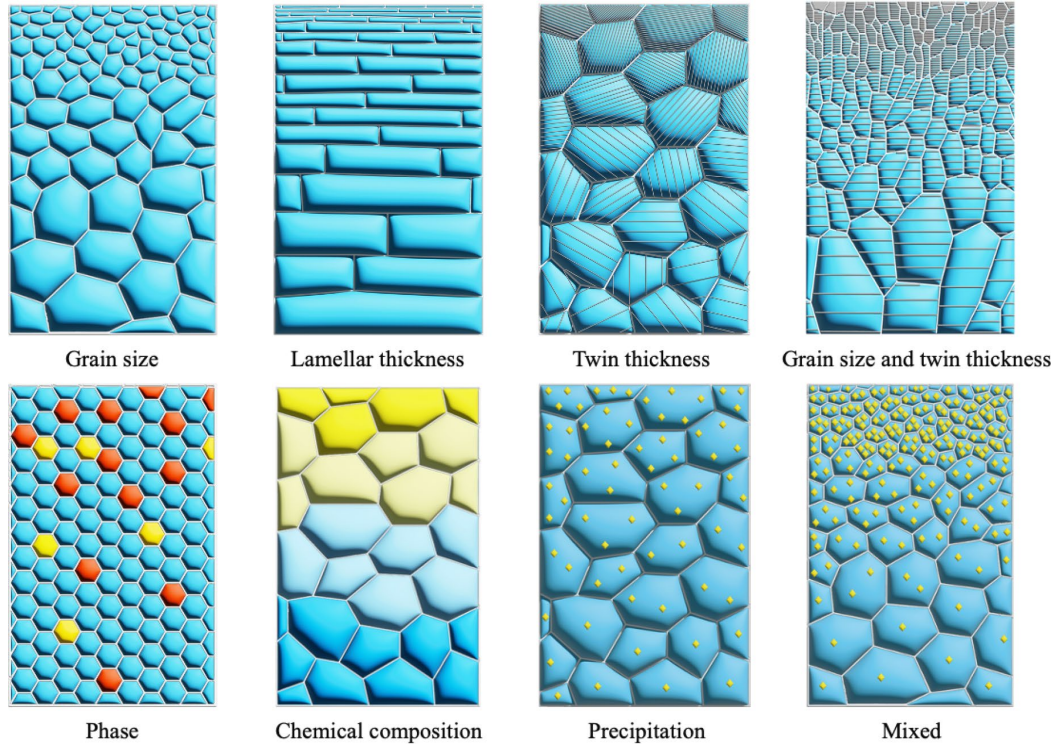


Figure 2.1: Structural and chemical gradients in typical metals and alloys. Structural gradients involve gradients in grain size, lamellar thickness, and twin thickness. Chemical gradients involve gradients in phase, chemical composition, and precipitate. Both structural and chemical gradients can coexist (Ji et al., 2023).

HSLs have been reported to display excellent material properties and the potential to achieve an advantageous strength-ductility trade-off (C. X. Huang et al., 2018; J. Li et al., 2019; Liang et al., 2019; Ma et al., 2016). The interesting property of HSLs originates from the synergy between the successive coarse grained (CG) and NG components as the CG layer exhibits remarkable ductility but low yield strength, while its NG counterpart is associated with reduced ductility but increased yield strength (Zhao et al., 2022). When under strain, this significant difference in the mechanical response between layers leads to the formation of interface affected zones (IAZs). More specifically, an IAZ, which is located near the interface in a CG layer, exhibits a large number of

dislocations and resulting back stress. The size of an IAZ is typically on the order of 5 μm to 6 μm (C. X. Huang et al., 2018), or the size of a coarse grain (Zhao, Zaiser, et al., 2021), and is believed to play a crucial role in the strengthening of such laminate materials. It was also reported that the tensile yield strength of HSLs increases significantly with decreasing layer thickness (C. X. Huang et al., 2018). However, its uniform elongation was found to be non-monotonic and changes as a function of layer thickness (C. X. Huang et al., 2018; Kümmel et al., 2016; Ma et al., 2016; Ma et al., 2015). This means that there is an optimum value for the layer thickness of HSLs and more systematic studies are required to identify such ideal design configuration depending on the specific material, or combination of materials, considered in such composite laminates. When studying the strengthening behaviour and attempting the quantitative prediction of the laminate properties, the rule of mixture (ROM) has generally been adopted by the research community (Ma et al., 2015; Nyung Lee & Keun Kim, 1988; Semiatin & Piehler, 1979; Zhao, Lu, et al., 2021). However, it should be noted that only the parameters CG and NG volume contents are considered when implementing the ROM method and the actual layer thickness is not taken into account. As a result, for a given ratio of volume content, the outcome of the ROM method is constant regardless of the change in layer thickness. This is a limitation of the ROM approach because, as reported in the experimental data from Huang and co-workers (C. X. Huang et al., 2018), the tensile strength of HSLs depends on the layer thickness for a given volume content. In addition, the ROM method is only applicable when the layer thickness is relatively large and the volume content of the IAZs is negligible (Ma et al., 2015). Besides, a larger hardening than that predicted by the ROM method was observed by Ma et al. (Ma et al., 2015). Thus, it is argued that there is still a need for further research to develop our understanding and modelling of the underlying strengthening mechanisms and the evolution of internal damage in HSLs such that the optimum design of these types of composite structures can be achieved.

2.2 Experimental investigations on HSMs

A number of experimental efforts have been reported in the literature to study the structural properties of HSMs (Liang et al., 2019; Zhao et al., 2022). Such investigations include that of Ma and co-workers who fabricated HSLs using high-pressure torsion, rolling and annealing (Ma et al., 2015). These authors found that different volume content of the NG layers and the resulting IAZs were crucial in determining the tensile deformation behaviour of HSLs. In addition, Huang et al. further investigated the deformation mechanism of HSLs using an in-situ micro tensile set-up combined with digital image correlation (DIC) technique (C. X. Huang et al., 2018). These authors found that the thickness of the layers should be about twice that of the IAZs to achieve optimal design in terms of strength-ductility trade-off.

More generally, the fabrication of HSMs includes bonding/joining of different materials (Kasaei et al., 2023; Meschut et al., 2022) or introduction of external factor to produce region with different grain size/phase. Depending on the significant difference in mechanical properties or physical properties, the HSMs can be further classified into structural and functional. Apart from the balanced strength-ductility, fracture resistance introduced before, the HSMs also bear advantages of being feasible by numerous thermomechanical large-scale, low cost processing techniques (Romero-Resendiz et al., 2023). Many different manufacturing methods are adopted to manufacture such HSMs such as severe plastic deformation (SPD) (Valiev et al., 2022) including equal channel angular pressing (ECAP), high pressure torsion (HPT), accumulative roll-bonding (ARB) etc. One fundamental advantage of Severe Plastic Deformation (SPD) techniques is the production of various scales of HSMs without the necessity for alloying elements or employing materials ranging from single-phase to multi-phase compositions. (Kasaeian-Naeini et al., 2022). A review of different processing methods and microstructure-property relationships focus on heterostructured stainless steel (HS SS) is provided in (Romero-Resendiz et al.,

2022).

Conventional methods such as SPD techniques are widely adopted for the manufacturing of HSMs as above mentioned. However, the obtained products usually have complicated residual deformation microstructure and strong deformation textures (Ma & Zhu, 2017). Moreover, it is difficult to fabricate HSMs with complex geometries and desirable spatial distribution of materials (D. Wang et al., 2022) using conventional methods. Currently, most conventional techniques, whether they are bottom-up (such as physical vapor deposition, electrodeposition) or top-down plastic deformation techniques (such as surface plastic deformation), result in HSMs that often struggle to meet the dimensional requirements for engineering applications. Hence, the limitations of preparation techniques pose significant challenges for the industrial application of HSMs.

Recent progress in additive manufacturing (AM) enables practitioners to purposely design inhomogeneous composition and complex geometry in an otherwise single-phase metal on a relatively large scale. AM can achieve high design freedom and flexibility in manufacturing HSMs using layer by layer or point by point principle on the micro/submicron scale, which makes it an ideal candidate for the precise control of spatial material distribution. However, there are currently some challenges in AM of HSMs, specifically, the powder delivery system, data preparation of HSMs before printing (D. Wang et al., 2022), process simulation, powder cross contamination/reaction and recycling, partially melted powder (Fan et al., 2023), material-structure-performance integrated prediction (Gu et al., 2021). To date, numerous efforts have been spared on AM of HSMs. The mechanical properties and deformation mechanisms of gradient nanostructures were reviewed in (Li et al., 2020). A more recent review is provided in (Ji et al., 2023) with a focus on AM methods. A review on AM of heterogeneous metallic parts is provided in (Karthik & Kim, 2021).

2.3 Analytical modelling

The analytical method is a systematic approach to solving problems by breaking them down into smaller, manageable components. It involves the application of mathematical, logical, and theoretical principles to derive solutions or gain insights into a problem. This method is often used to simplify complex systems, enabling precise and predictable outcomes, and is widely employed in fields such as engineering, science, and economics. Yuan and Du developed an analytical model for heterogeneous laminates and revealed their hardening mechanism (Yuan & Du, 2020). Another analytical model for gradient-nanostructured 304 stainless steels was proposed by Zhu and co-workers by taking into account the depth-dependent grain size and nano scale structure. The predictions obtained by these authors agreed well with experimental results in terms of yield stress, ductility and strain hardening rate. In spite of this, analytical methods have typical limitations for investigating the spatial distribution of field variables and are restricted to the modelling of relatively simple deformation scenarios. Some other researchers adopted the rule of mixture (ROM) (Li et al., 2017) to investigate the mechanical properties of polycrystalline materials. However, an under-estimation in strength is reported in this case because interactions between grains are excluded (X. Wu et al., 2014).

2.4 Numerical investigations on HSMs

To complement experimental research, numerical methods stand as a valuable tool for quantitatively establishing connections between microstructure and the macroscopic mechanical response of HSMs, as well as for fine-tuning their microstructural arrangement. Furthermore, the plastic deformation of HSMs contains complex interactions coupled across various length scales. This scale-coupling calls for multiscale frameworks to effectively investigate the mechanical behaviour of such materials. Therefore, the systematic investigation

of dislocation behaviour within heterostructures is an important scientific endeavour, which entails conducting thorough numerical investigations coupling multiple mechanisms. Different numerical tools at various length scales have been adopted by the research community to attempt such studies on heterostructured materials, including MD, DDD, CPFEM/FEM and analytical methods.

2.4.1 Strain gradient plasticity

The development of small scale and miniaturised devices over the past few decades has triggered a significant growth in the development of manufacturing processes for the fabrication of microscale components and the generation of sub-micrometre surface structures (Lai et al., 2008). The production of small scale parts and features may rely on processes, such as micro forming and micro mechanical machining, for which the plastic deformation of the bulk material is not only affected by high strain rates but also by the well-documented “size effect” as the volume of the strained region reduces (Joshi & Melkote, 2005; Wang et al., 2015). For metallic materials in particular, it is known that an increase in strain rate results in a hardening behaviour, while the size effect has also been reported to lead to such an increase in flow stress. In this context, well-defined mechanical properties at macroscopic level no longer apply for the simulation of material behaviour on the microscale because of the non-linear evolution of these properties with the reduction in dimension of the strained volume. In other words, this means that a typical constitutive material model, such as the Johnson-Cook model (Johnson & Cook, 1985), which is widely used by practitioners on the macroscale, becomes less suited to simulate strain rate dependent microscale phenomena because it does not account for the size effect.

Undertaking mechanical tests on small specimens, where the dimension of the strained region is relevant to plastic deformation-based micro fabrication processes, is one possible way to re-evaluate and calibrate material parameters

of the JC constitutive model. A number of experimental research efforts have been reported in the past 30 years to investigate material properties on small scales, i.e., typically in the range from a few hundred nanometres to a few tens of micrometres. This body of knowledge, which includes the investigation of material properties in tension (Kiener et al., 2008; Kiener et al., 2006; Molotnikov et al., 2008), torsion (Guo et al., 2017; Lu & Song, 2011), compression (Li et al., 2022; Q. Liu et al., 2021), fracture (Peng et al., 2012) and fatigue (Huang et al., 2020; Yan et al., 2020) on small scales suggests that microstructure evolution can be caused by size effect, strain rate effect and temperature. For example, Hou et al (Hou et al., 2022) found that the ultimate tensile yield stress of micro-scale pure copper becomes weaker with a decreased diameter while the yield stress increased. El-Deiry and Vinci (El-Deiry & Vinci, 2001) reported variations of the effective moduli of microscale Al and Cu wires at different strain rates. Chang et al (Chang et al., 2022) prepared micro-size copper fibres using cold drawing and a ‘smaller but stronger effect’ was observed with the conducted tensile tests. The reduced grain size and preferred texture orientation caused by cold drawing were attributed to this hardening effect. Fleck and co-workers (Fleck & Hutchinson, 1993; Fleck et al., 1994) and Liu and co-workers (Liu et al., 2013; Liu et al., 2012) reported different amplitudes of size effects in microscale copper wires in tension and torsion experiments under quasi-static strain rates. Liu et al (Q. Liu et al., 2021) pointed out that the structural evolution of AISI 1045 steels presented a strong strain rate effect, which in turn should influence material behaviour on the microscale. Overall, the research reported above shows that material behaviour at small scales under dynamic loading can be quite different from that under quasi-static loading. In addition, it is fair to say that while experimental approaches are important, conducting microscale tests in a reliable manner under high strain rate scenarios is a challenging task to achieve in practice. Indeed, such tests are associated with implementation complexity and the general limited availability of equipment outside specialist research facilities.

For these reasons, numerical methods can be a useful complementary tool to experimental investigations for predicting the response of microscale specimens to plastic deformation for a range of processing scenarios, such as those under high strain rate conditions. Various numerical tools, which include molecular dynamics (MD) (P. Fan et al., 2022; Geng et al., 2015; Goel et al., 2017; Liang & Zhou, 2004), crystal plasticity finite element method (CPFEM) (Lin et al., 2020), discrete dislocation dynamics (DDD) (Lu, Kan, et al., 2022; S. Lu et al., 2019), and multiscale approaches such as finite element combined with atomistic method (FEAt) (Kohlhoff et al., 1991), bridging scale method (BSM) (Wagner & Liu, 2003), coupled atomistic and discrete dislocation plasticity (CADD) approaches (Miller et al., 2004) and quasi-continuum (QC) method (Tadmor et al., 1996), have been developed to model and investigate the behaviour of strained material at such small scales. The general limitation of these methods mainly lies in the complexity associated with their implementation and in some cases, with the adoption of spatiotemporal scales, which do not reflect actual deformation conditions. For example, the strain rate involved in MD simulations can be unrealistically high, such as 10^7 s^{-1} to 10^9 s^{-1} (Peng et al., 2012). Besides, the necessity to acquire specific material properties on the atomistic scale can be a further limitation of these simulation techniques. In contrast, the low order mechanism-based strain gradient plasticity theory (MSGP) (Huang et al., 2004) can be employed to alleviate the issues associated with the aforementioned numerical methods. More specifically, MSGP is relatively straight forward to implement within a continuum-based modelling framework for simulating plastic deformation on realistic space and time scales (Voyiadjis & Song, 2019, 2020). As a result, MSGP has been employed to simulate a wide range of processes where inhomogeneous plastic flow is present within a small strained region such as in indentation (Backes et al., 2009; Ding et al., 2021; Harsono et al., 2011; Qu et al., 2006; Tang et al., 2021), wire drawing (Byon et al., 2009), blanking (S. Wang et al., 2017) and fracture (Martínez-Pañeda & Betegón, 2015; Qu et al., 2004; Wu et al., 2023) and also in

specific material structures such as metallic composites (Zhang et al., 2007) and gradient structured metals (Cheng et al., 2023; Y. Zhang et al., 2020). At the same time, it should be noted that most MSGP-based simulations are rate independent. Consequently, this does not truly reflect the nature of plastic deformation conditions under certain microscale scenarios and particularly in the context of microscale manufacturing processes, such as forming and mechanical machining. At the same time, and as mentioned above, the classical Johnson-Cook (JC) constitutive material model, which based on continuum mechanics and which takes into account of varying strain rate and temperature conditions, has been used widely and shown to be robust in the modelling of conventional metal-based deformation processes.

In this context, the prospect of combining the strain gradient plasticity and the JC theories would seem to be a natural and promising avenue of investigations to simulate the plastic flow of microscale specimens under high strain rate conditions. This approach has only been adopted by a few researchers until now. More specifically, Wang (Wang, 2007) included the gradient plasticity model of second and fourth order in the JC model analytically. In addition, this approach was followed by Lai et al (Lai et al., 2008), Khandai et al (Khandai et al., 2022) and Fan et al (Y. Fan et al., 2022b) in the modelling of microscale machining; by Chakrabarty and Song (Chakrabarty & Song, 2020) for the numerical simulation of the cold spray process; and by Guo and co-workers (Guo et al., 2016; Guo et al., 2015) for the simulation of the ballistic performance of nanostructured metals. The majority of these endeavours accounted for the strain gradient by introducing 'strain gradient correction terms'. This means that the value of the plastic strain gradient was considered either to be constant and or expressed as a function of the specific problem investigated. Indeed, Guo and co-workers derived the plastic strain gradient value from experimental calibration (Guo et al., 2016; Guo et al., 2015), while Lai et al (Lai et al., 2008), Khandai et al (Khandai et al., 2022) and Fan et al (Y. Fan et al., 2022a) based its determination on the length of the primary machining deformation zone.

Finally, when considering the cold spray process, Chakrabarty et al (Chakrabarty & Song, 2020) related the strain gradient value on a flattening parameter. In the present research, it is argued that there are two issues associated with this specific body of literature which attempted to combine the strain gradient plasticity and the JC theories. First, considering the plastic strain gradient to be a constant value as in is likely not a fully robust approach from a physical viewpoint. Second, the approach of determining the value of the plastic strain gradient based on specific material deformation scenarios, as exemplified in (Chakrabarty & Song, 2020; Y. Fan et al., 2022a; Khandai et al., 2022; Lai et al., 2008), may be regarded as overly restrictive. This is because such a methodology inherently limits the ability to predict material responses at small scales and high strain rates within a generalized framework.

2.4.2 Molecular dynamics

Molecular Dynamics (MD) is a computational simulation method used to study the physical movements of atoms and molecules over time (Jiang et al., 2023; Plimpton, 1995; Thompson et al., 2022). By solving Newton's equations of motion for a system of particles, MD provides insights into their dynamic behaviour and interactions at the atomic scale. The MD method can be adopted to investigate the mechanical response of gradient structures as reported by Fang and co-workers (Fang et al., 2018). More specifically, these authors employed a 2D model to address constraints of computational efficiency and mismatch on the spatiotemporal level since the consideration of only tens of grains would otherwise be achievable in a typical 3D MD model. Despite the efforts presented by these authors, the classical MD method remains not well suited for the quantitative investigation of dislocation activities and back stress observed during experiments. On the other hand, the MD method (Geng et al., 2022) can only be used on the nanoscale and thus, is restricted to a few tens of grains due to constraints linked to its computational efficiency and mismatch on the spatiotemporal level. More importantly, as mentioned earlier, the

deformation mechanisms for nanograined polycrystalline material is significantly influenced by activities on grain boundaries (GBs) (Meyers et al., 2006). Thus, it can be said that the associated deformation mechanisms, i.e., dislocations and related back stress, cannot be readily investigated using MD. In summary, conventional MD simulations encounter two major challenges when investigating dislocation behaviours. Firstly, the high strain rate nature of MD simulations often lacks relevance to the grain-level dislocation motion typical of heterostructured materials under quasi-static loading. Secondly, current studies have primarily focused on limited examples of dislocation motion due to computational costs. For example, the largest grain size adopted was 105 nm in (Li et al., 2015), which is smaller than the range of grain size typically considered in heterostructured materials.

2.4.3 Discrete dislocation dynamics

The Discrete Dislocation Dynamics (DDD) method is a computational approach used to model and simulate the behaviour of dislocations, which are line defects in crystalline materials (Giessen & Needleman, 1995; Quek et al., 2014; Tarleton et al., 2015). By representing individual dislocations and tracking their interactions, movements, and reactions under various stress and temperature conditions, DDD provides insights into the microscopic mechanisms governing plastic deformation. This method is particularly valuable for bridging the gap between atomic-scale simulations and continuum plasticity theories, offering a detailed understanding of phenomena such as dislocation multiplication, annihilation, and pattern formation (Miller et al., 2004). In DDD simulation, plastic deformation is usually constrained to be smaller than 3%, restricting the range of investigations on strain hardening behaviour under larger deformation (Lu, Zhao, et al., 2022). Thus, while informative, studies on HSMs through this method have limitations for providing a comprehensive understanding of dislocation behaviour on larger strain ranges. Simulating and understanding the contribution of individual mechanisms towards overall strain hardening

requires a comprehensive numerical framework.

2.4.4 Crystal plasticity finite element method

The Crystal Plasticity Finite Element Method (CPFEM) is a computational technique used to model the mechanical behaviour of crystalline materials at the grain scale (Roters et al., 2010; Roters et al., 2012). It integrates the principles of crystal plasticity, which accounts for the anisotropic deformation mechanisms like slip and twinning, with finite element analysis to simulate material responses under various loading conditions. CPFEM provides insights into microstructural phenomena, such as texture evolution and stress-strain localization, enabling the study of structure-property relationships in polycrystalline materials. Despite extensive numerical work reported on the nanoscopic and macroscopic levels, the behaviour of grain-level interactions in HSMs is comparatively less explored. The CPFEM method typically serves as an advanced tool for investigating the impact of grain-level information on larger scales, while simultaneously capturing the spatial-temporal dynamics of dislocation-related deformation processes. Research efforts on investigating heterostructured materials via CPFEM can be classified into three categories. The first type is based on classical local CPFEM where the grain size effect is excluded. For example, CPFEM has been adopted for the investigation of cracks in gradient aluminium (L.-Y. Liu, Q.-S. Yang, X. Liu, & X.-C. Nian, 2021) and graphene/aluminium composites (L.-Y. Liu, Q.-S. Yang, X. Liu, & J.-J. Shang, 2021). A local CPFEM was employed for the investigation of interfacial characteristics of metal matrix composites (Zhang et al., 2022; Y. B. Zhang et al., 2024). Although the classical CPFEM method allows for a direct grain-level determination of interactive mechanisms, the presence of significant dislocation hardening, and the resulting size effect, is neglected. During uniaxial tension, the non-uniform deformation-induced GNDs contribute to the strain hardening of heterostructured materials through forest hardening (Cheng et al., 2018; X. Wu et al., 2014). Thus, such classical crystal plasticity models are unlikely to be

capable of capturing correctly deformations arising at grain boundaries (Liang & Dunne, 2009). The second type of CPFEM adopted for the investigation of heterostructured materials considers the grain size effect based on the Hall-Petch law (Y. Wang et al., 2017; Zeng et al., 2016; Zhang et al., 2021) or experimentally defined functions (Griesbach et al., 2024). A size-dependent crystal plasticity model containing dislocation slipping and deformation twinning was developed for the investigation of gradient nanostructured Twinning Induced Plasticity steels (Lu et al., 2020). Damage evolution and mechanically driven grain growth during the deformation of gradient nano-grained materials were also considered into the constitutive model to study the role of microstructure gradient in the overall plastic response (X. Lu et al., 2019). CPFEM was also adopted to study the strengthening mechanisms of gradient medium entropy alloys (Zhang, Gui, et al., 2023). Synergistic enhanced mechanical properties of gradient nanostructured metals were considered in (Griesbach et al., 2024) using size-dependent CPFEM where the dislocation density distribution relied on experimentally defined functions instead of a phenomenological Hall-Petch relation. This second type of CPFEM models typically introduces grain size dependent equations, which usually rely on extensive experiments and the calibration of required parameters. In comparison, the third type of CPFEM models naturally captures the extra hardening due to inhomogeneous plasticity. Such models physically describe the collective behaviour of dislocations associated with crystallographic relationships between adjacent grains. This modelling approach provides more physical meaning and represents an ideal tool for revealing the deformation mechanisms of metallic materials rather than mimicking stress-strain relations (Zhang, Zhao, et al., 2023). Such a non-local CPFEM approach coupled with GNDs and related kinematic hardening in gradient grained materials was developed in (Zhang, Zhao, et al., 2023). However, grains were not spatially resolved in this work as the authors used a homogenisation scheme when modelling the whole specimen. Such homogenisation scheme can describe the

deformation heterogeneity between grains but it neglects such heterogeneity inside grains (Wu et al., 2017). Mutual interactions of slip localisation processes at variable distances within the same grain or in neighbouring grains can affect grain deformation (Stinville et al., 2023). Thus, the effect of microstructural variations in heterostructured materials on the incipient plasticity and dislocation mechanisms remains largely unexplored. The explicit modelling of heterogeneous grained metals in large-scale polycrystal simulations can help accelerate microstructural design for improved strength and ductility. Of the many polycrystalline deformation modelling tools, the ones that should best meet the above challenges combine CPFEM and a full-field mechanical approach (Stinville et al., 2023). Nevertheless, recognising the significance of strengthening mechanisms and damage initiation is vital in constructing a comprehensive understanding of strengthening in metallic heterostructured materials. In a recent study, full field CPFEM has been adopted for the investigation of the low-cycle fatigue property of IN718 (Xi et al., 2024). However, this was achieved in the context of a homogeneous-grained material and thus, not in the context of heterostructured materials.

2.4.5 Homogenized finite element method

The Finite Element Method (FEM) is a numerical technique used to solve complex engineering and physical problems by dividing a large system into smaller, simpler parts called finite elements. These elements are analysed individually, and their solutions are assembled to approximate the behaviour of the entire system. FEM is widely used in structural analysis, heat transfer, fluid dynamics, and other fields to solve problems involving partial differential equations or large geometries with complex boundary conditions. It offers flexibility in modelling various shapes, materials, and load conditions. Some researchers, such as Wu et al. (X. L. Wu et al., 2014), employed this traditional FEM to investigate the stress, strain and strain gradient distribution across the thickness direction of gradient steel. The constitutive models used by these

authors for the CG and gradient layers were obtained by fitting uniaxial tensile stress-strain data on individual layers. Although the extra strengthening of the composite laminates was modelled when considering the stack of these layers, the exact underlying deformation mechanisms at play were not fully elucidated. Li and co-workers developed a dislocation density-based theoretical model and investigated the mechanical behaviour of gradient structures (Li & Soh, 2012). Experiments and FEM modelling were further employed by Li et al. to study the strength-ductility synergy of gradient structures (Li et al., 2017). Although multiple mechanisms, including geometrically necessary dislocation (GNDs) and back stress, were considered by these authors, the FEM model developed was limited to conducting 2D analyses. Zhao et al. presented a constitutive FEM model considering the deformation heterogeneities and multiple related mechanisms, such as dislocations and back stress strengthening (Zhao, Zaiser, et al., 2021). The effect of grain size, layer thickness and the NG layer volume content were thoroughly investigated and compared with experimental data. However, the failure criteria and the study of the microhardness were not included in this work. Besides, the numerical framework adopted by these authors would not be well suited if one was to follow it for simulating dynamic processes. To address the limitations of the numerical methods reported above, Li et al., (Li & Soh, 2012; Li et al., 2017) and Zhao et al., (Zhao et al., 2019; Zhao et al., 2020) developed a multiple mechanism-based framework and demonstrated its implementation within the ABAQUS/STANDARD module. However, these researchers did not consider a damage criterion. Consequently, their work is limited for the modelling of dynamic processes where ABAQUS/EXPLICIT and a damage criterion would be favourable. Although applying an homogenisation scheme is an efficient way to investigate the effects of multiple deformation mechanisms (Zhao et al., 2019; Zhao et al., 2023; Zhao, Lu, et al., 2021; Zhao et al., 2020), it does not allow for a comprehensive understanding of the spatial distribution and evolution of deformation characteristics for each grain, and consequent effects on the local

extra strength.

2.5 Summary and knowledge gaps identified

This Chapter provided a comprehensive review of the development of HSMs, with a particular focus on the numerical approaches employed to investigate their strengthening mechanisms. Specifically, it examined the current state-of-the-art in numerical methodologies when applied to HSMs, including (1) MD, (2) DDD, (3) CPFEM/FEM and (4) analytical modelling, focusing on their synergistic effects and fracture. The current attempts to integrate MSGP and JC model were also discussed. Based on the studies reviewed, several key conclusions and knowledge gaps pertinent to the objectives of this Thesis have been identified as follows:

Knowledge gap 1: There is a lack of implementation of methodology to extract an explicit and real-time estimation of the plastic strain gradient within an MSGP-modified JC computational framework. A few researchers have attempted to combine the strain gradient plasticity theory within the JC constitutive material model for the numerical simulation of plastic flow when microscale specimens are deformed under medium to high strain rate scenarios. This combined approach bears the advantage of being relatively straightforward to implement within realistic space and time scales in a continuum-based modelling framework. However, one issue within this body of literature is that, until now, the plastic strain gradient has either been considered as a constant or expressed as a function of the specific problem investigated. It is argued that this current state-of-the-art is too restrictive as it does not support the numerical prediction of small scale and high strain rates material behaviour regardless of the loading scenario. To address this gap, the research presented in Chapter 3 proposes a methodology to compute explicitly

the plastic strain gradient value in real time at every simulation iteration within a three-dimension strain gradient modified JC computational framework.

Knowledge gap 2: A constitutive model which could quantitatively investigate the sources of hardening and the internal damage evolution of HSLs and to predict the response of such laminate materials under a range of deformation scenarios, including in tension and during nanoindentation is yet to be developed. Despite recent experimental and numerical progress, the deformation mechanism of HSLs, and the corresponding evolution of dislocations and back stress, remains unclear. Besides, to realise the numerical simulation of HSLs when subjected to dynamic deformation processes, a framework coupled with damage criterion is needed. It is also argued that the further understanding of strengthening and damage mechanisms of HSLs should lead to the enhanced tailoring and design of these materials such that their promising strength-ductility synergy can be taken full advantage of. An efficient and robust physical mechanisms-based 3D numerical method coupled with failure criterion remains to be developed to address this gap. This is particularly important considering the large design space that is typical of HSLs, i.e., material employed, layer thickness and the respective grain size of the CG and NG layers. The associated modelling framework development, results and discussions are reported in Chapter 4.

Knowledge gap 3: While a non-local CPFEM model was developed for the investigation of heterostructured materials in (Zhang, Zhao, et al., 2023; Yong Zhang et al., 2024), grains were not explicitly considered in these studies. As a result, mechanisms such as shear band and grain rotation could not be captured. Despite extensive numerical work reported on the nanoscopic and macroscopic levels, the behaviour of grain-level interactions in heterostructured materials is comparatively less explored. CPFEM method typically serves as an advanced tool for investigating the impact of grain-level information on larger scales, while simultaneously capturing the spatio-

temporal dynamics of dislocation-related deformation processes. In light of this knowledge gap, a non-local full-field CPFEM model, which explicitly accounts for the interaction between dislocations and grain boundaries, is developed and reported in detail in Chapter 5.

Knowledge gap 4: The intriguing synergy effect during the deformation process of metallic HSMs is still not fully understood due to the difficulties in accurate description of the real ‘fracture’ process at the microscale. The crystal plasticity finite element method (CPFEM) is widely used to capture grain-level mechanical responses (Loukadakis & Papaefthymiou, 2024; Roters et al., 2010). CPFEM has also been used to investigate SBs in single crystal and multi-crystal pure aluminium (Luan et al., 2020), aluminium alloys (Wu et al., 2017; Wu et al., 2016) and interstitial free steel (Sedighiani et al., 2022). However, most of these studies lack the consideration of damage models to effectively predict fracture. Only a few investigations focussed on CPFEM damage modelling. These were carried out in the case of single-phase steel (Wu & Zikry, 2015) and gradient metals (L.-Y. Liu, Q.-S. Yang, X. Liu, & X.-C. Nian, 2021; Xiao et al., 2024; Zheng Zhang et al., 2024). Based on this body of literature, it can be said that there is a need to conduct numerical investigations of HSMs using CPFEM with the incorporation of fracture. Furthermore, although extensive experimental work has been carried out to investigate strengthening mechanisms in HSMs, most reports are empirical and lack in-depth and comprehensive understanding of fundamental strengthening sources, such as dislocation activities and SBs formation and evolution. Consequently, the general endeavour of designing HSMs with an optimised balance of strength and ductility remains at the stage of experimental attempts. For these reasons, the focus of Chapter 6 is on the development of a non-local CPFEM-CDM model and further demonstrated to TWIP/Maraging steel laminate specimens for the investigation of strengthening mechanisms and fracture characteristics.

Chapter 3 Development of a 3D strain gradient modified Johnson-Cook computational framework

3.1 Introduction

The research presented in this Chapter proposes a methodology to compute explicitly the plastic strain gradient value in real time at every simulation iteration within a three-dimension strain gradient modified Johnson-Cook computational framework. The theoretical background, the numerical implementation process and the FEM modelling aspects are introduced in detail. The developed framework is then used to conduct uniaxial tensile and torsion simulations of microscale copper wires with different diameters. The results of these simulations are presented and discussed. The size and strain rate effects and their respective quantitative contribution to the material hardening are also discussed in detail. The conclusions are presented in section 3.4.

3.2 Constitutive relations and FEM modelling

3.2.1 Mechanism-based SGP modified JC constitutive model

In this section, the proposed MSGP-modified JC constitutive model is introduced. The classical JC theory (Johnson & Cook, 1985) defines the flow stress as

$$\sigma_{JC} = [A + B(\bar{\epsilon}^{pl})^n] \left[1 + C \ln \left(\frac{\dot{\epsilon}^{pl}}{\dot{\epsilon}_0} \right) \right] (1 - \hat{\theta}^m) \quad (3.1)$$

where A , B , C , m , n are the traditional coefficients of the JC model, $\bar{\epsilon}^{pl}$ is the equivalent plastic strain, $\dot{\epsilon}^{pl}$ is the plastic strain rate, $\dot{\epsilon}_0$ is the reference strain rate and $\hat{\theta}$ is the temperature term. The MSGP theory is based on Taylor hardening model (Taylor, 1997) where the shear stress, τ , is related to the dislocation density as:

$$\tau = \alpha G b \sqrt{\rho} \quad (3.2)$$

G is the shear modulus, α is an empirical constant which takes value between 0.3 and 0.5, b is the magnitude of the Burgers vector and ρ is the total dislocation density. In the presence of strain gradients, ρ can be further divided into the statistically stored dislocation (SSD) density, ρ_S , and the geometrically necessary dislocation (GND) density, ρ_G , as follows:

$$\rho = \rho_S + \rho_G \quad (3.3)$$

In addition, the tensile flow stress is related to the shear flow stress by:

$$\sigma_{flow} = M\tau \quad (3.4)$$

where M is the Taylor factor. Thus, combining (2) and (4), the flow stress using Taylor's model is given as:

$$\sigma_{flow} = M\alpha G b \sqrt{\rho_S + \rho_G} \quad (3.5)$$

According to Ashby (Ashby, 1970), the GND density is calculated as:

$$\rho_G = \bar{r} \frac{\eta}{b} \quad (3.6)$$

where \bar{r} is the Nye's factor (Nye, 1953) and η is the equivalent plastic strain gradient. ρ_S can be determined by material tests where the strain gradient is negligible and thus, when only SSDs influence the material behaviour. In this case, the classical JC model is applicable, and the following expression is given:

$$M\alpha G b \sqrt{\rho_S} = \sigma_{JC} \quad (3.7)$$

which can re-formulate as:

$$\rho_S = \left(\frac{\sigma_{JC}}{M\alpha G b} \right)^2 \quad (3.8)$$

Substituting (3.7) into (3.5), the flow stress becomes:

$$\sigma_{flow} = \sigma_{JC} \sqrt{1 + \frac{\rho_g}{\rho_s}} \quad (3.9)$$

Substituting (3.6) and (3.8) into (3.9) and considering that for FCC metals, M and \bar{r} are equal to 3.06 and 1.90, respectively, the flow stress can now be expressed as (Lai et al., 2008):

$$\sigma_{flow} = \sigma_{JC} \sqrt{1 + \left(\frac{18\alpha^2 G^2 b}{\sigma_{JC}^2} \eta \right)^\mu} \quad (3.10)$$

where $\frac{18\alpha^2 G^2 b}{\sigma_{JC}^2}$ is defined as material characteristic length l . μ is introduced to represent the density of GNDs needed to accommodate the strain gradient in the deformation zone following the work of Eq. (10) describes the material constitutive model which combines the JC and the mechanism based SGP theories. As a result, the influence of the size effect, the strain rate and the processing temperature can be captured in one formulation.

3.2.2 Methodology for the explicit calculation of the plastic strain gradient

In this section, the explicit calculation of plastic strain gradient, η , is discussed. The elemental level plastic strain increment is calculated using the equivalent plastic strain at the Gaussian points rather than at the elemental nodes which means that extrapolation is necessary. Then, the incremental plastic strain gradient is calculated by differentiation of the shape functions. Following the work of (Gao et al., 1999), the strain gradient is related to the plastic strain components as follows:

$$\Delta\eta_{ijk}^p = \Delta\varepsilon_{ik,j}^p + \Delta\varepsilon_{jk,i}^p - \Delta\varepsilon_{ij,k}^p \quad (3.11)$$

The strain gradient is reformulated as:

$$\Delta\eta_{ijk}^p = \sum_{k=1}^8 N_k(\xi, \eta, \zeta) (\Delta\bar{\varepsilon}_{ij}^{pl}) \quad (3.12)$$

where $N_k(\xi, \eta, \zeta)$ is the shape function vector, the detailed introduction of which can be found in the appendix, and $\Delta\bar{\varepsilon}_{ij}^{pl}$ is the incremental equivalent plastic strain. Similar to the effective strain, which can be expressed as $\varepsilon = \sqrt{\frac{2}{3} \varepsilon_{ij} \varepsilon_{ij}}$, the effective strain gradient is:

$$\Delta\eta^p = \frac{\eta_{ijk}^p \Delta\eta_{ijk}^p}{\eta^p} \quad (3.13)$$

η_{ijk}^p can be computed in the same way as $\Delta\eta_{ijk}^p$. Under rate-proportional loading, $\Delta\eta^p$ can be calculated as (Fleck & Hutchinson, 1997):

$$\Delta\eta^p = \sqrt{\frac{1}{4} \Delta\eta_{ijk}^p \Delta\eta_{ijk}^p} \quad (3.14)$$

$\Delta\eta^p$ is further simplified as a scalar measure of spatial gradients of the accumulated equivalent plastic strain, $\bar{\varepsilon}_i^p = \partial \varepsilon^p / \partial x_i$.

$$\Delta\eta^p = \sqrt{\bar{\varepsilon}_{,i}^p \bar{\varepsilon}_{,i}^p} \quad (3.15)$$

It is important to note that the JC shear failure criterion is also included in the developed model. More specifically, the failure strain $\bar{\varepsilon}_f^{pl}$ is calculated as follows (Johnson & Cook, 1985): The JC shear failure criterion is also included in the developed model. More specifically, the failure strain $\bar{\varepsilon}_f^{pl}$ is calculated as follows (Johnson & Cook, 1985):

$$\bar{\varepsilon}_f^{pl} = (d_1 + d_2 e^{d_3 \frac{p}{q}}) (1 + d_4 \ln(\frac{\dot{\bar{\varepsilon}}^{pl}}{\dot{\varepsilon}_0})) (1 + d_5 \hat{\theta}) \quad (3.16)$$

where d_1, d_2, d_3, d_4, d_5 are parameters of JC shear failure criterion, q is the von Mises stress, p is the hydrostatic stress and $\frac{p}{q}$ is the stress triaxiality. A summation of incremental failure strain $\Delta\bar{\varepsilon}_f^{pl}$ is performed over all increments to calculate the failure criterion ω as follows:

$$\omega = \Sigma \left(\frac{\Delta\bar{\varepsilon}_f^{pl}}{\bar{\varepsilon}_f^{pl}} \right) \quad (3.17)$$

Once ω exceeds a critical threshold, i.e., a value over 1, the affected elements are deleted in the next solver step. The classical JC constitutive model was defined in the VUHARD subroutine. The equivalent plastic strain, $\bar{\epsilon}^{pl}$, von Mises stress, q , and hydrostatic stress, p , needed for the algorithm are obtained with the VGETRM utility subroutine at the end of each increment in the VUSDFLD subroutine. In this way, the strain gradient is explicitly obtained at the end of each increment. Figure 3.1 displays the flow chart of the implemented MSGP-modified JC algorithm.

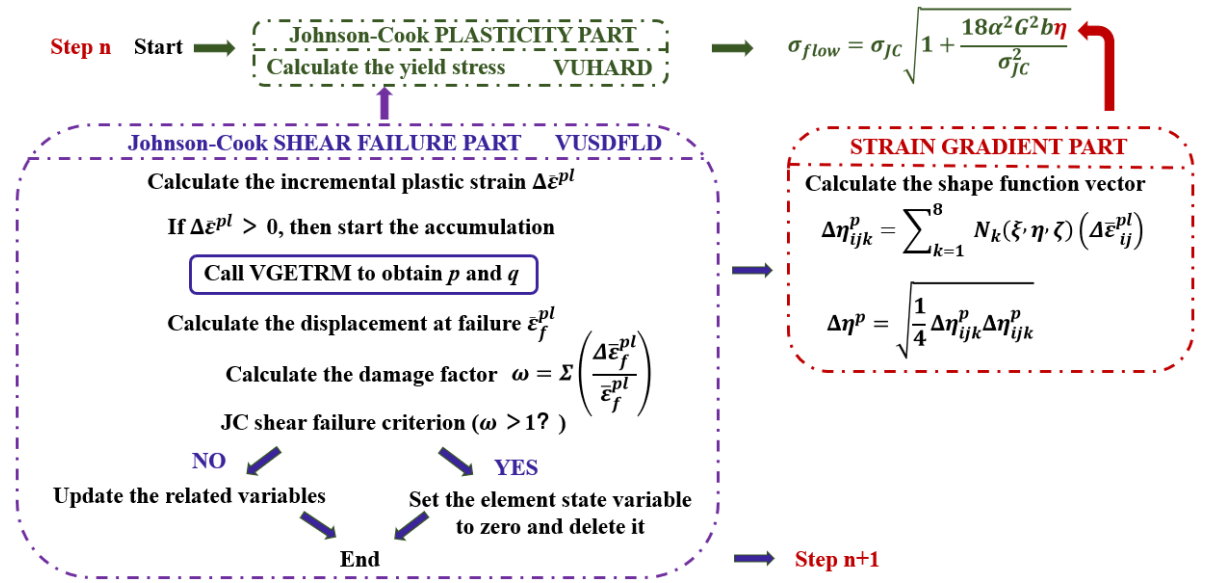


Figure 3.1: Flow chart of the MSGP-modified JC algorithm.

3.2.3 Finite element model set-up

Using the model and methodology described above, simulations were conducted to investigate the effect of strain rate and strain gradient on micro-scale copper wires with different diameters in uniaxial tension and torsion. The simulations were conducted using the ABAQUS/Explicit module using the user-defined subroutines discussed in section 3.2. In tension, all degrees of freedom (DOF) on the base part were assigned as fixed boundary condition and only the x direction of the grip part was ascribed to move (see Figure 3.2(a)). In torsion, the grip and base parts were subjected to a rotation of 1.57 (radians) in the $UR1$ direction and the remaining DOFs were constrained. Conditions of

quasi-static strain rate and middle to high strain rates of 100 s^{-1} and 1000 s^{-1} were considered to investigate the strain rate effect. The sample dimensions, loading conditions and typical mesh are displayed in Figure 3.2. The diameter values of the copper wire were selected to be $18 \text{ }\mu\text{m}$, $30 \text{ }\mu\text{m}$, $42 \text{ }\mu\text{m}$ and $105 \text{ }\mu\text{m}$ to compare the simulation results against the experimental data published in (Liu et al., 2012). The unit system and relevant material parameters used in the simulation are given in Table 1 and Table 2 respectively. The diameters of the copper wire were selected to be $18 \text{ }\mu\text{m}$, $30 \text{ }\mu\text{m}$, $42 \text{ }\mu\text{m}$ and $105 \text{ }\mu\text{m}$ to compare the simulation results against the experimental data published in (Liu et al., 2012). The unit system and relevant material parameters used in the simulation are given in Table 3.1 and Table 3.2 respectively.

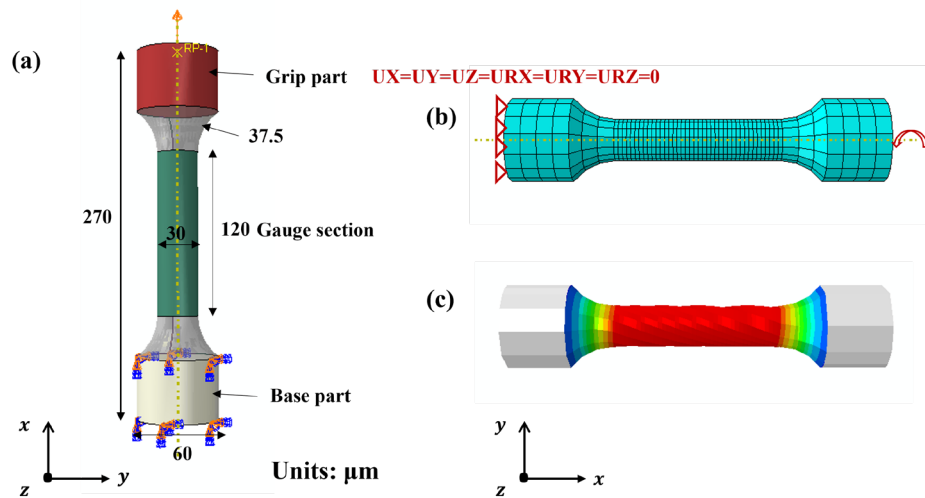


Figure 3.2: (a) Schematic illustration of one of the simulated dog-bone-shaped specimens (diameter of $30 \text{ }\mu\text{m}$ in tension), (b) FE model and meshing of the specimen in torsion, (c) typical stress distribution during torsion simulation.

Table 3.1: Adopted unit system in ABAQUS.

Dimension	Length L	Force	Stress $M \cdot L^{-1}$	Time T	Mass M	Density
Unit	μm	$M \cdot L \cdot T^{-1}$ mN	$1 \cdot T^{-1}$ GPa	s	Ton	$M \cdot L^{-3}$ 10^{21} kg/m^3

Table 3.2: Material properties used in this Chapter.

	Parameter	Value		Parameter	Value
Mechanical properties (Johnson & Cook,	E (GPa)	124	Johnson-Cook shear failure (Johnson & Cook, 1985)	d_1	0.54
	ν	0.34		d_2	4.89
	ρ (kg/m ³)	8960		d_3	-3.03
				d_4	0.014
				d_5	1.12
Johnson-Cook plasticity (Johnson & Cook,	A (GPa)	0.09	Plastic strain gradient (Joshi & Melkote, 2005)	a	0.5
	B (GPa)	0.292		G (GPa)	39
	n	0.31		b (nm)	0.256
	C	0.025		μ	0.38

3.3 Results and discussion

Based on the computational framework described in the previous section, a series of simulated results were obtained and are presented here. The simulated stress in tension was calculated as an average value of the von Mises stress of the gauge section as displayed in Figure 3.2. The simulated shear strain in torsion was calculated using $a\theta/L$, where L is the gauge length, a is the radius of the wire and θ is the torsion angle. Following the notation in (Fleck & Hutchinson, 1993; Fleck et al., 1994), the normalized torque, Q/a^3 , was plotted against the surface shear strain in torsion as shown in Figure 3.3(b) and Figure 3.4(b), where κ is the twist per unit length of the wire.

3.3.1 Size effect

Figure 3.3(a) shows the tensile stress-strain curves of copper wires with different diameters at quasi-static strain rate obtained with the simulations conducted in this work and also as reported experimentally in (Liu et al., 2012). This figure also displays the stress-strain curve simulated using the classical JC constitutive model. Only one such curve is visible in this case as the classical JC expression does not account for size effects (see Equation (3.1)). A similar approach is followed to display the results shown in Figure 3.3(b) which are

concerned with the obtained normalised torque against the surface shear strain. It can be observed from both Figure 3.3(a) and Figure 3.3(b) that when implementing the MSGP-modified JC constitutive model proposed in this research, both the simulated flow stress and the normalized torque increased with the decrease of the microscale wire diameter. This is a result which is aligned with experimental findings and with the general strain gradient plasticity theory. The maximum flow stress and normalised torque were obtained for both the simulation and experimental conditions when the considered wire diameter was the smallest, i.e., 18 μm . In tension, the simulated stress-strain curves for diameters of 30 μm , 42 μm and 105 μm , (see Figure 3.3(a)), are relatively close to each other, which agrees well with experimental findings in (Liu et al., 2012) indicating that the size effect diminishes when the sample dimension exceed approximately 105 μm . In torsion, it is only the 30 μm and 42 μm diameter wires that yielded rather similar simulated data. This is again aligned with the experimental finding reported in Figure 3.3(b) and a consequence of the fact that, within the range 18 μm to 105 μm , an increase in diameter from 30 μm to 42 μm can be considered not really significant. The reason for the observed size effect for both simulation and experimental data is explained by the increase in the strain gradient inherent in small and localised zones which leads to the generation of extra geometrical necessary dislocations (GNDs) (Nye, 1953) and causes additional hardening (Fleck & Hutchinson, 1993). In practice, the dislocation starvation at smaller size would also contribute to this size effect. However, this phenomenon is not accounted for in the proposed model. The observed size effect in torsion, as displayed in Figure 3.3(b), is more pronounced than that in tension, as also reported in (Fleck et al., 1994; Liu et al., 2012). This explains why the simulation results obtained for the 105 μm wire diameter in torsion is quite distinct from those of the 30 μm to 42 μm wires, whereas such difference is not so pronounced with the tensile simulations. Generally, this 'smaller but stronger' size effect is also aligned with widely reported experimental findings on micro-scale copper wires, such as

those in (Chang et al., 2022; Hou et al., 2022; Kiener et al., 2008).

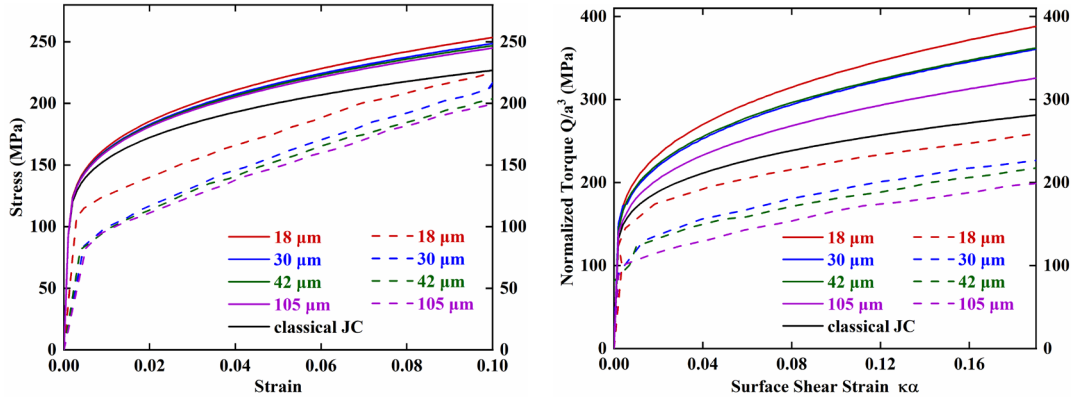


Figure 3.3: (a) Stress-strain curves under quasi static strain rate for copper wires in tension with diameters of 18 μm , 30 μm 42 μm and 105 μm , (b) Plots of normalized torque-twist curves for copper wires with diameters of 18 μm , 30 μm 42 μm and 105 μm . The simulated results are plotted with solid lines and experimental data are plotted with dashed lines.

It should also be said that the presented numerical results in tension and torsion are in good agreement with the experimental results from (Liu et al., 2012) in terms of trends and order of magnitude. However, there is some discrepancy with respect to actual values achieved with the developed model. This might be because the material parameters used in the simulation conducted in this research may not truly reflect the experimental conditions for comparison purpose. More specifically, Liu and co-workers stated that: ‘all wires were annealed at 410 °C for 2.4h’ (Liu et al., 2012). Thus, it is reasonable to expect that the annealing treatment in (Liu et al., 2012) led to a larger grain size and smaller dislocation density (El-Deiry & Vinci, 2001). In turn, this would lead to a reduced experimental flow stress and normalised torque values. This is corroborated with the fact that other mechanical properties have also been reported to decrease following annealing when compared to the as-received material such as the scratching hardness of microscale copper (Kareer et al., 2016a, 2016b) and the uniaxial tensile and compression properties of steel and high-entropy alloy (Chen et al., 2019; Ren et al., 2022). The material properties

implemented in the presented work were those from bulk standard copper (Johnson & Cook, 1985). If reliable and comprehensive material data for annealed copper can be obtained, it is expected that the simulation and experimental results will align more closely.

3.3.2 Strain rate effect

Tension and torsion simulations were also conducted at strain rates of 100 s^{-1} and 1000 s^{-1} to investigate whether the model was capable of predicting the size effect at higher strain rates and importantly, to understand from a theoretical viewpoint whether flow stress is dominated by size effect or strain rate in such scenarios. Figure 3.4(a) and (b) display the simulated curves under the strain rates of 100 s^{-1} and 1000 s^{-1} in tension and torsion, respectively. From Figure 3.4(a), it is observed that the elastic part of all curves in tension are superimposed. This indicates that the elastic deformation is rate independent. In the plastic deformation region, it can be seen from Figure 3.4(a) and Figure 3.4(b) that, using the classical JC constitutive model in tension and torsion, the copper wires were hardened under higher strain rates. This is expected as Equation (3.1), which reports the classical JC flow stress expression, incorporates the effect of strain rate. The results reported in these figures also show that the size effect is observed in both tension and torsion, similarly to that existing under quasi-static strain rate. This indicates that the size effect is present under all strain rates studied in this work. This simulated combined influence of the strain rate and size effects agrees well with the experimental findings reported in for micro-tensile tests conducted on Ni-based materials. In particular, these authors found that both size and strain rate effects occurred on the microscale and that the yield stress and strain rate sensitivity scaled well to bulk macroscale properties. This also correlates with MD simulation data reported in (Liang & Zhou, 2004) where the size and strain rate effects were shown to co-exist and lead to the co-hardening of copper material at small scales.

From the simulation results presented in Figure 3.4, it can be said that the size effect is still more pronounced in torsion than that in tension at higher strain rates. It can also be observed that the simulated copper wires exhibited a peculiar torsion simulation response at the higher strain rate of 1000 s^{-1} where the normalised torque is seen to fluctuate around the initial yield point. These fluctuations are associated with the initiation of severe plastic deformation caused by high strain rate. Similar pronounced fluctuations were also observed in (Liang & Zhou, 2004) for the high strain rate MD simulation of nano copper wires in tension.

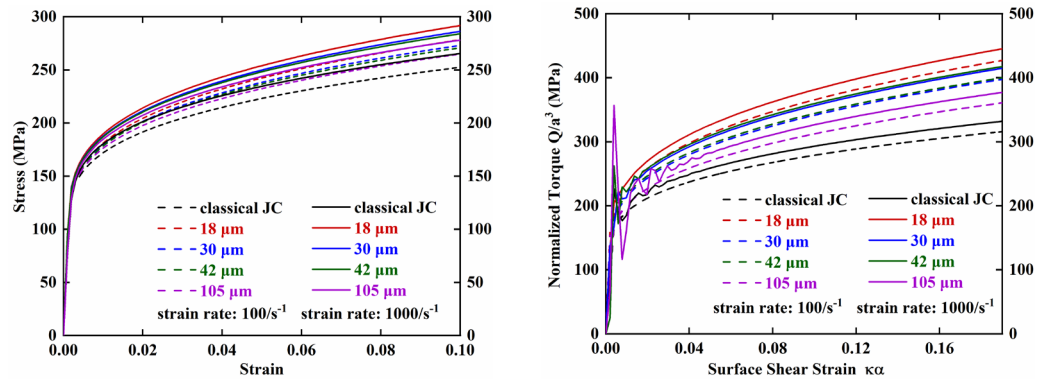


Figure 3.4: (a) Stress-strain curves for copper wires in tension with diameters of $18 \mu\text{m}$, $30 \mu\text{m}$, $42 \mu\text{m}$ and $105 \mu\text{m}$ under the strain rate of 100 s^{-1} (dashed lines) and 1000 s^{-1} (solid lines), (b) Plots of normalized torque-twist curves for copper wires with diameters of $18 \mu\text{m}$, $30 \mu\text{m}$, $42 \mu\text{m}$ and $105 \mu\text{m}$ under the strain rate of 100 s^{-1} (dashed lines) and 1000 s^{-1} (solid lines).

The incremental yield stress could also be readily obtained using the self-compiled classical JC subroutines and MSGP-modified JC subroutines by outputting state variables. The final yield stress in tension at the strain of 0.1 and torsion at the surface shear strain of 0.19 are displayed in Figure 3.5 for all strain rates. The readers should note that the discrepancies in Figure 3.5 are not errors but rather predictions under different strain rates and conditions (with and without the size effect under tension and torsion). The final yield stress using the classical JC approach in both tension and torsion remains identical

under the same strain rate while it increases with a larger strain rate indicating that the strain rate effect exists on the microscale. The enhanced yield stress might be caused by the dynamic wave effect or phonon drag (Liang & Zhou, 2004). When using the MSGP-modified JC constitutive model developed in this work, the final yield stress increases with a reduction in the wire diameter under all strain rates. It is shown that size effect for the final yield stress exists under all simulated strain rates. More interestingly, the size effect for the final yield stress in torsion is more significant than that in tension as shown in Figure 3.5. This was also reported experimentally in (Fleck et al., 1994; Liu et al., 2012). The enhanced yield stress might be caused by the dynamic wave effect or phonon drag (Liang & Zhou, 2004). When using the MSGP-modified JC constitutive model developed in this work, the final yield stress increases with a reduction in the wire diameter under all strain rates. It is shown that size effect for the final yield stress exists under all simulated strain rates. More interestingly, the size effect for the final yield stress in torsion is more significant in tension as shown in Figure 3.5 which was also reported experimentally in (Fleck et al., 1994; Liu et al., 2012). The reason behind this difference in the magnitude of the size effect between tension and torsion is due to the fact that, in uniaxial tension, hardening is mainly due to the SSDs, which can be relatively moderate for a given wire diameter (Fleck et al., 1994). In torsion however, and for the same wire diameter, the strain gradient $d\gamma/da=\kappa$ and the severe non-homogeneity of deformation introduce an increased amount of GNDs. For a given surface shear strain, a thinner wire, i.e., a smaller a , introduces a larger strain gradient and a greater density of GNDs. As a result, a more prominent hardening in thinner wires would thus be observed. The more pronounced equivalent plastic strain/shear strain in torsion is attributed to this size effect. Although the size effect for the final yield stress is obvious, one should notice that, compared to the classical JC model, the initial yield stress remains constant using the MSGP-modified JC approach proposed here. This is due to the fact that the MSGP-modified JC theory is based on dislocations that only exist

during plastic deformation (Fleck et al., 1994; Liu et al., 2012).

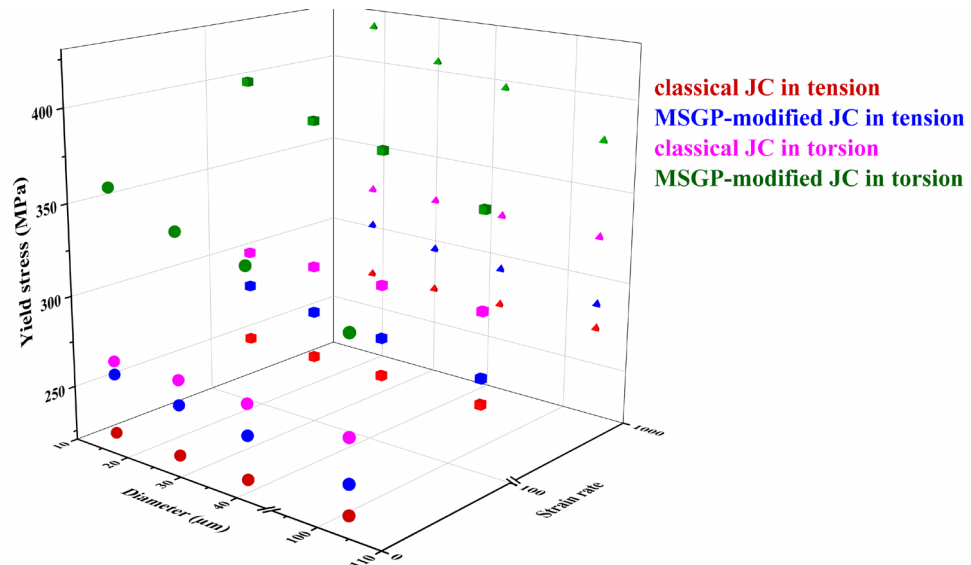


Figure 3.5: Simulated predictions of final yield stress data (for a strain of 0.1 in tension and a surface shear strain of 0.19 in torsion) for copper wires with diameters of 18 μm, 30 μm, 42 μm and 105 μm under quasi-static strain rate (dot marker), and strain rate values of 100 s⁻¹ (cube markers) and 1000 s⁻¹ (tetrahedron markers).

To experimentally investigate the mechanical behaviour at the microscale for the strain rates mentioned, specialized techniques are required. While Hopkinson bar experiments are widely used for high strain rate testing at the macroscale, adapting these methods to the microscale presents several challenges. These include the difficulty of fabricating microscale specimens with consistent geometry, ensuring accurate alignment and loading, and capturing reliable data due to the small scale and potential material heterogeneity. Alternative approaches, such as micro-tensile testing combined with high-speed imaging or laser-based methods, could be explored to achieve precise strain rate control and measurement at the microscale. These techniques, while promising, also require careful consideration of their limitations, such as the influence of boundary conditions and the resolution of strain measurement

systems.

3.3.3 Respective contribution of the size effect and the strain rate effect

The respective contribution of different hardening factors to the enhanced flow stress was also quantitatively investigated and the outcome of such a comparison is plotted in Figure 3.6. As discussed earlier, obvious size and strain rate effects can be observed, and both are more pronounced in torsion than in tension. It is interesting to notice from this figure that for a given diameter, the contribution from the size effect in both tension and torsion remains nearly constant under different strain rates. In contrast, and as one would expect, the contribution from the strain rate becomes more important with the increased strain rate. Figure 3.6 also shows that, under the varying strain rate range studied here (i.e., for 100 s^{-1} and 1000 s^{-1}), which can be considered to be high, the strain rate increase is the dominant contribution to the hardening of the material in tension. This relative contribution is further enhanced with the increase of the wire diameter. This is because, for a given strain rate value, the contribution of this effect remains constant with varying wire diameters while the contribution of the size effect reduces when the wire diameter becomes larger. Under high strain rate torsion deformation, while the size effect remains the dominant factor for all wire diameter and strain rate values considered, a trend can be observed that this relative contribution of the size effect decreases with the increase of wire diameter. Experimentally obtained data in (Xu et al., 2018) for microscale Ni wires in tension showed that the flow stress increased by 15 MPa to 35 MPa when the strain rate was multiplied by a factor of 100. Interestingly, when analysing our simulation results, we observed an increase in flow stress by a similar order of magnitude. In particular, the simulated flow stress of microscale copper wires, which is also a face-centred cubic (FCC) metal, was raised by around 13 MPa in tension when the strain rate was 1000 s^{-1} instead of

100 s⁻¹.

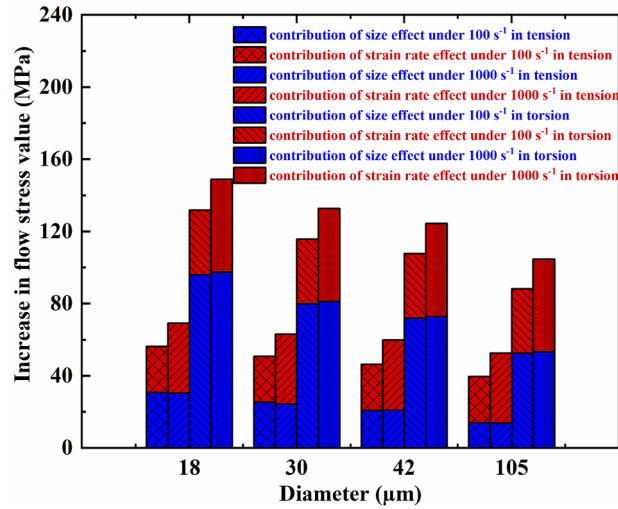


Figure 3.6: Relative contributions of size and strain rate effects to the increase in the flow stress value for different copper wire diameters. The plotted increase in flow stress was obtained by comparing the simulated data against a baseline simulation scenario defined as that using the classical JC method under quasi-static strain rate.

3.4 Conclusion

The research in Chapter 3 proposed and implemented a computational framework that combines 1) the classical Johnson-Cook theory that includes damage criterion with 2) the mechanism-based strain gradient plasticity theory to derive a constitutive material model that could be applied for the numerical simulation of high strain rate deformation scenarios on the microscale. These plastic flow conditions can, for example, be representative of micro-manufacturing processes such as micro forming and micro mechanical machining. The distinguishing characteristic of this work, in comparison with previous attempts at combining the Johnson-Cook and the strain gradient plasticity theories, is that the plastic strain gradient value is extracted explicitly at every simulation time-step. Based on this novel 3D MSGP-modified JC framework, tensile and torsion simulations were also conducted on microscale

copper wires for a range of wire diameters and strain rates. The outcome of these simulations was shown to compare well against experimental data found in the literature. Based on this model, it was also possible to quantify the respective contribution of strain rate and strain gradient effect on the hardening of small-scale copper wire specimens. While the JC model provides a robust framework for simulating material behaviour under high strain rates and temperatures, it is important to acknowledge its limitations. The empirical nature of this model means it relies heavily on experimental data for calibration, which may restrict its generalisability to materials or conditions outside the tested range. Additionally, the JC model does not account for certain microstructural effects or anisotropic behaviour, which could influence accuracy in more complex scenarios. These limitations highlight the need for further refinement or complementary approaches in future work.

Chapter 4 Development of a multiple mechanism based constitutive model coupled with damage criterion for investigating the deformation of HSLs

4.1 Introduction

The study of this Chapter is organised as follows: the constitutive model for the NG and CG layers as well as the IAZ, the JC failure criterion and the numerical implementation process are introduced in section 4.2. In section 4.3, indentation and tensile simulations on homogenous grained copper are carried out first to validate the correctness and robustness of the developed numerical framework. The quantitative investigation of strengthening of Interstitial-Free (IF) steel was investigated as well. Then, the effect of the layer thickness and the NG volume content on the mechanical response of HSLs are investigated. Calculations that rely on the ROM method and the model prediction method proposed by Zhao and co-workers (Zhao, Zaiser, et al., 2021) are also conducted and compared against those published in the literature to further validate the accuracy of the numerical work reported here. Finally, the distinguishing characteristic of this research, i.e., the developed integrated FEM model, which combines the multiple physical mechanisms based constitutive model coupled with the JC damage criterion, is implemented to study the synergistic effect and mutual constraints of the NG and CG layers in the laminates as well as the damage evolution during the deformation process. Conclusions and issues needing further investigation are then presented in section 4.4.

4.2 Numerical framework and FEM model

4.2.1 Multiple mechanisms based constitutive model

Considering the significant dislocation activity experimentally observed in the deformation process of laminates and the relative ease of numerically implementing the conventional mechanism-based strain gradient (CMSG) theory, the deformation response and strengthening mechanism of HSLs were investigated based on the CMSG (Huang et al., 2004) and dislocation pile-up (Hirth et al., 1983) theories in this research. The flow stress is related not only to the statistically stored dislocations (SSDs) but also to the geometrically necessary dislocations (GNDs) from the sample level, the grain level and the back stress. This direct introduction of dislocations into the constitutive model does not require the need to consider higher order stresses and boundary conditions and thus can be implemented within the VUHARD/VUSDFLD subroutines, which are mathematically easier than the UEL/VUEL and VUMAT/UMAT subroutines (Lele & Anand, 2008; Lele & Anand, 2009). A multiscale schematic of the developed model is shown in Figure 4.1 and the associated constitutive equations are presented in the following sub-sections.

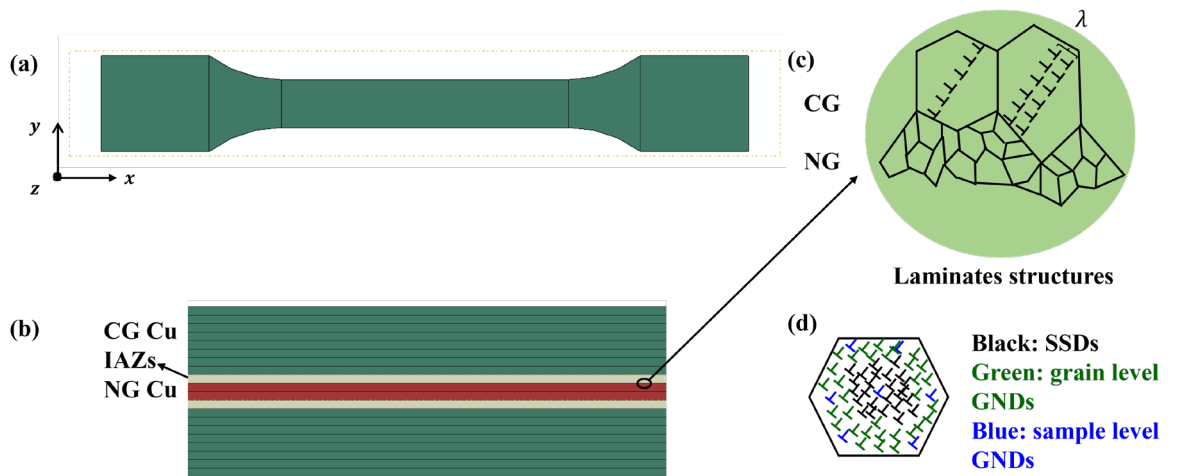


Figure 4.1: (a) Schematic diagram of the modelled tensile dog-bone specimen; (b) layers of the integrated FEM model with a NG volume content of 10 %; (c) schematic of piled-up GNDs near the boundaries of NG and CG layer; (d)

schematic of the various dislocations considered in the presented work.

4.2.2 Constitutive model for homogenous layers

The Taylor hardening law was adopted in the presented work to relate the flow stress with the dislocation density. The dislocation density can be further decomposed into the SSD density, ρ_{SSDs} , and the GND density, ρ_{GNDs} . The flow stress σ_f is defined as:

$$\sigma_f = \sigma_0 + M\alpha Gb\sqrt{\rho_{SSDs} + \rho_{GNDs}} + \sigma^b \quad (4.1)$$

where σ_0 is the lattice friction stress, M is the Taylor factor, α is a material constant, G is the shear modulus, b is the magnitude of the Burgers vector and σ^b is the back stress. Considering the significant amount of back stress observed experimentally and following the work of (Hirth et al., 1983; Zhao et al., 2020; Zhao, Zaiser, et al., 2021), the back stress σ^b is defined as:

$$\sigma^b = \frac{Mgb}{\pi(1-\nu)d}N \quad (4.2)$$

where d is the grain size, ν is the Poisson's ratio, N is the dislocation number within a pile-up. The rate of change of N is defined following the work of (Sinclair et al., 2006).

$$\dot{N} = N_\Delta \left(\frac{2}{3} \dot{\epsilon}^p - \frac{N}{N^*} \dot{p} \right) \quad (4.3)$$

Considering the negligible effect of the plastic strain components $\dot{\epsilon}^p$ and to ease the implementation process, equation (3) is simplified as:

$$\dot{N} = N_\Delta \dot{p} \left(\frac{2}{3} - \frac{N}{N^*} \right) \quad (4.4)$$

where N_Δ is the initial evolution rate of N , N^* is the saturated pile-up dislocation number and \dot{p} is the equivalent plastic strain rate. N^* and N_Δ are defined with equation (4.5) and (4.6) respectively (Zhao, Zaiser, et al., 2021):

$$N^* = \frac{\pi(1-\nu)k_{HP}}{Mgb} d^{\frac{1}{2}} \quad (4.5)$$

$$N_{\Delta} = \frac{4M\lambda}{3b} \quad (4.6)$$

where k_{HP} is the Hall-Petch constant, λ is the distance between slip lines as shown in Figure 4.1(c).

During the deformation process, apart from the back stress, the dislocation hardening is also caused by the interactions between dislocations as shown in Figure 4.1(d). This dislocation hardening behaviour is included in the presented work as stated in equation (4.1). The density of piled-up GNDs is defined on both the sample level and the grain level as:

$$\rho_{\text{GNDs}} = \rho_{\text{GNDs}}^{\text{sam}} + \rho_{\text{GNDs}}^{\text{gra}} \quad (4.7)$$

where $\rho_{\text{GNDs}}^{\text{sam}}$, $\rho_{\text{GNDs}}^{\text{gra}}$ are the sample level and the grain level GNDs density, respectively. The grain level GNDs density is defined as (Zhao, Zaiser, et al., 2021):

$$\rho_{\text{GNDs}}^{\text{gra}} = \frac{d}{\lambda} \frac{N}{d^2} \quad (4.8)$$

where $\frac{d}{\lambda}$ is the number of pile-ups in a grain.

Apart from the GNDs for the grain level, the non-uniform strain gradient is also generated via dislocation pile-up (Ma et al., 2016) which would lead to the size effect. The layer thickness studied in the experiments can be as thin as 3.7 μm (C. X. Huang et al., 2018) and the smallest nanoscale grain size is 100 nm. Therefore, the effect of GNDs on the sample level, although expected to be not that significant in tensile loading scenarios, is also included in this work and defined following the work in (Ashby, 1970; Nye, 1953).

$$\rho_{\text{GNDs}}^{\text{sam}} = \bar{r} \frac{\eta^p}{b} \quad (4.9)$$

where \bar{r} is Nye's factor (Nye, 1953) and η^p is the strain gradient which can be

calculated using $\Delta\eta^p = \sqrt{\frac{1}{4}\Delta\eta_{ijk}^p\Delta\eta_{ijk}^p}$ (Fleck & Hutchinson, 1997).

GNDs play a critical role in accommodating strain gradients in crystalline materials. The separation of GNDs into grain-level and sample-level contributions is essential for understanding deformation mechanisms at

different length scales. Grain-level GNDs arise from local lattice rotations within individual grains, often due to intragranular deformation mechanisms such as dislocation pile-ups at grain boundaries. In contrast, sample-level GNDs reflect macroscopic strain gradients across the polycrystalline structure, ensuring compatibility between grains during deformation.

This distinction is particularly relevant for modelling and predicting material behaviour under mechanical loading. For instance, grain-level GNDs provide insight into localized deformation phenomena, such as strain hardening and grain boundary strengthening, while sample-level GNDs help characterize the overall strain distribution and mechanical response of the material. By separating these contributions, a more accurate description of the material's deformation behaviour can be achieved, which is crucial for designing materials with tailored mechanical properties.

Experimentally, the split of GNDs into grain and sample contributions can be achieved using high-resolution techniques such as electron backscatter diffraction (EBSD). EBSD allows for the measurement of local misorientations within grains, which can be used to calculate GND densities. By applying dislocation density tensor analysis, it is possible to differentiate between intra-grain (grain-level) and inter-grain (sample-level) contributions to the total GND density. Complementary techniques, such as transmission electron microscopy (TEM) or X-ray diffraction (XRD), can further validate these measurements and provide additional insights into dislocation structures.

A modified Kocks-Mecking-Estrin (KME) model (Estrin, 1998; Kocks, 1976; Mecking & Kocks, 1981) proposed by Li et al. (Li & Soh, 2012) is adopted in this work to describe the evolution of SSDs for both the CG and NG phases.

$$\frac{\partial \rho_{\text{SSDs}}}{\partial \varepsilon^p} = M \left[\frac{k_{mfp}^g}{bd} + \frac{k_{mfp}^{dis}}{b} \sqrt{\rho_{\text{SSDs}} + \rho_{\text{GNDs}}} - k_{\text{ann}} \left(\frac{\dot{\varepsilon}^p}{\dot{\varepsilon}_{\text{ref}}} \right)^{-\frac{1}{n_0}} \rho_{\text{SSDs}} - \left(\frac{d_{\text{ref}}}{d} \right)^2 \rho_{\text{SSDs}} \right] \quad (4.10)$$

where k_{mfp}^g and k_{mfp}^{dis} are geometric factor and proportional factor that control the dislocation activities at the grain boundaries and the dislocation reactions on the dislocation mean free path (MFP), $\dot{\varepsilon}_{\text{ref}}$ is the reference strain rate and d_{ref} is

the reference grain size, k_{ann} is the dislocation annihilation factor and $k_{\text{ann}} \left(\frac{\dot{\epsilon}^p}{\dot{\epsilon}_{\text{ref}}} \right)^{-\frac{1}{n_0}} \rho_{\text{SSDs}}$ represents the dislocation annihilation, which quantifies the rate-dependent reduction in dislocation density due to dynamic recovery processes. $\dot{\epsilon}^{\text{ref}}$ is typically chosen based on experimental conditions or standard testing protocols. n_0 is determined by fitting experimental data from strain rate tests, such as stress-strain curves at different strain rates. $\dot{\epsilon}^p$ is obtained directly from experimental measurements or simulations.

4.2.3 Constitutive model for interface affected zones (IAZs)

In this work, the thickness values considered for the CG layer were 4.8 μm and 4 μm , while it was 100 nm for the NG layers to ensure that the simulations aligned with the experiments reported in (C. X. Huang et al., 2018; Ma et al., 2015) for comparison purpose. This significant difference in grain size leads to a mechanical incompatibility between interfaces during plastic deformation and further results in high GND density, strain gradient (Zhao et al., 2022) and back stress (Wu & Zhu, 2017). The dislocation ledge source theory (Murr, 2016) states that NG-CG interfaces could act as sources of dislocations. Experiments show that there exists a ‘one grain width zone’ (about 5 μm to 6 μm) in the CG layer near the NG-CG interface where the GND density is higher than in other parts of that layer (J. Li et al., 2019; Liang et al., 2019; Ma et al., 2016). This zone is called the IAZ. The dislocation pile-up behaviour in the IAZs is different from that in the homogenous layers due to the significant difference in layer properties as reported above. Following the work of Zhao et al. (Zhao, Zaiser, et al., 2021), the dislocation number within a pile-up for an IAZ is defined as:

$$N_{\text{IAZ}}^* = \frac{\pi(1-\nu) \left(k_{\text{HP}} d_{\text{NG}}^{-\frac{1}{2}} + \Delta\sigma_0 \right)}{Mgb} d_{\text{CG}} \quad (4.11)$$

where d_{NG} is the size of a nano grain and d_{CG} is the size of a coarse grain, $\Delta\sigma_0$ is

the difference of lattice friction stress between the NG and the CG layers. Comparing equation (11) with equation (5), a larger dislocation pile-up is produced in the IAZ region which would further lead to a larger back stress.

4.2.4 Johnson Cook failure criterion

Quantitatively, experimental reports also indicate that the uniform deformation of a NG layer in the laminates is at least ten times higher than that of its a stand-alone counterpart (Ma et al., 2015; Wu et al., 2020). Based on this, in the classical ROM approach or the modified ROM method proposed in Zhao et al. (Zhao, Zaiser, et al., 2021), the engineering stress of the NG layer in the laminates is assumed to be constant after necking. Although a reasonable correlation between experimental and predicted results was observed when adopting this assumption in the case of HSLs displaying a relatively large layer thickness, the prediction accuracy of this approach reduces as the layer thickness decreases. While it can indeed be said that the NG layer in the laminate is much stronger than when it is considered standalone, it is questionable to assume that its engineering stress remains constant after necking when developing a numerical model of HSLs. For this reason, not only it is important to take into account of multiple physical mechanisms when developing a constitutive model of HSLs, it is also essential to include a failure criterion when developing an integrated FEM model of HSLs. The JC failure criterion (Johnson & Cook, 1985), which was initially proposed for macroscopic metal failure, has proven to be robust and efficient for simulating metal deformation processes on the microscale (Guo et al., 2014; Guo et al., 2016; Lai et al., 2008; Z. Wang et al., 2019). This is due to its comprehensive inclusion of the effect of strain, strain rate and temperature. Thus, given the limitations of the current numerical methods reported above for modelling HSLs, it is proposed that the JC failure criterion is also considered when numerically simulating the indentation and uniaxial tensile responses of HSL materials.

As stated by Zhao et al. (Zhao, Zaiser, et al., 2021), a reasonable damage and failure model should be developed to investigate the synergistic behaviour of the NG and CG layers in HSLs. Herein, the JC dynamic failure model, which is proved to be robust in microscale processes affected by large deformations (Lai et al., 2008; Z. Wang et al., 2019), was adopted as the failure criterion. The JC failure model comprehensively includes the effect of strain hardening, strain rate and temperature. More specifically, the JC failure model is based on the calculation of the equivalent plastic strain, which is expressed as also shown in equation (3.16).

A summation of incremental failure strain $\Delta\bar{\epsilon}_f^{pl}$ is performed over all increments to calculate the failure criterion ω (Johnson & Cook, 1985). Failure is considered to be reached when the JC failure criterion, ω , increases to a value equal to "1". The damage parameters used in this work were those defined for copper (Johnson & Cook, 1985).

4.2.5 Implementation and finite element modelling

The constitutive model and JC failure criterion introduced in the previous section were implemented via user-defined subroutine VUHARD/VUSDFLD and thus can be used with ABAQUS/EXPLICIT. The implementation flow chart is displayed as shown in Figure 4.2. The microhardness of homogenous grained layers, i.e., the NG and CG layers were also investigated numerically using a Berkovich pyramid indenter following the work reported in (C. X. Huang et al., 2018). The imperfection of the tip, i.e., the tip bluntness as well as the friction between the indenter and the specimen, were also taken into account based on the work of (Antunes et al., 2007; Antunes et al., 2006; Sakharova et al., 2009). The indentation speed was set to 10 $\mu\text{m} / \text{s}$ and the indentation depth was 10 μm . The schematic diagram of the FEM model for indentation is shown in Figure 4.3. The dimension of the dog-bone shaped specimen for the uniaxial tensile simulations on homogenous copper and for

the subsequent integrated FEM modelling was set following the reports in (C. X. Huang et al., 2018) and (Ma et al., 2015), respectively. The gauge section consisted of three zones, i.e., the NG layer, the CG layer and the IAZ zone as shown in Figure 4.1(a) and 1(b). The specimen was discretised using C3D8 elements, and the gauge section was refined to ensure mesh independence on the simulated results. The strain rate was set to 5×10^{-4} (C. X. Huang et al., 2018) and the material properties in the constitutive model parameters were sourced from published data as listed in Table 1. The stress (in the S11 and S22 directions), strain and all the state variables discussed in this work were calculated using the average value of the gauge section. A Python script was compiled to extract the variables and plot the results for comparison with experimental data.

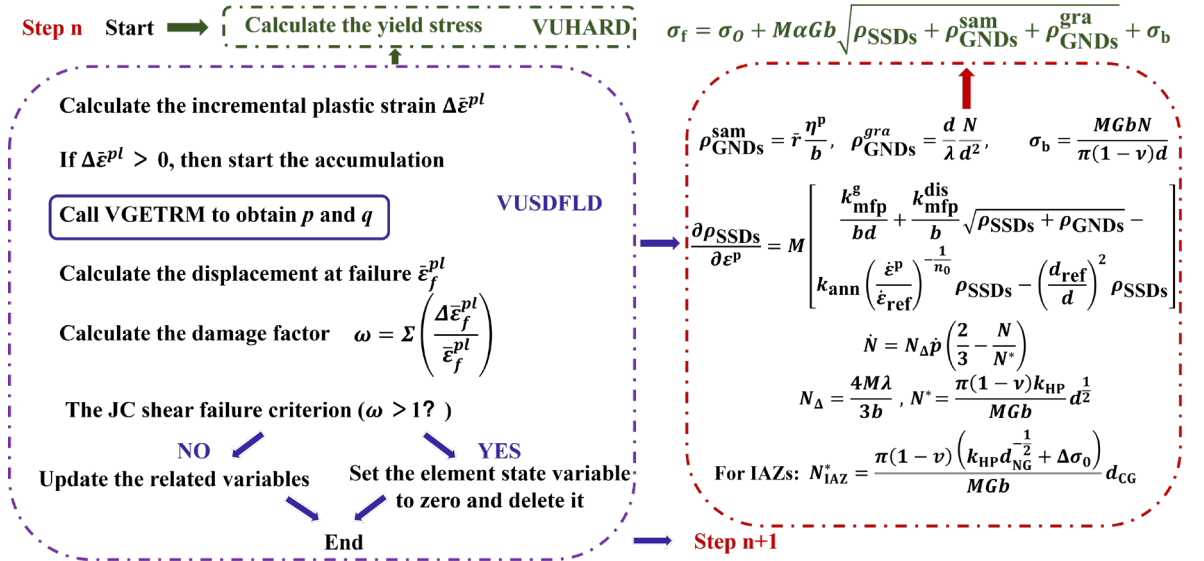


Figure 4.2: Flow chart of the developed 3D multiple physical mechanisms algorithm.

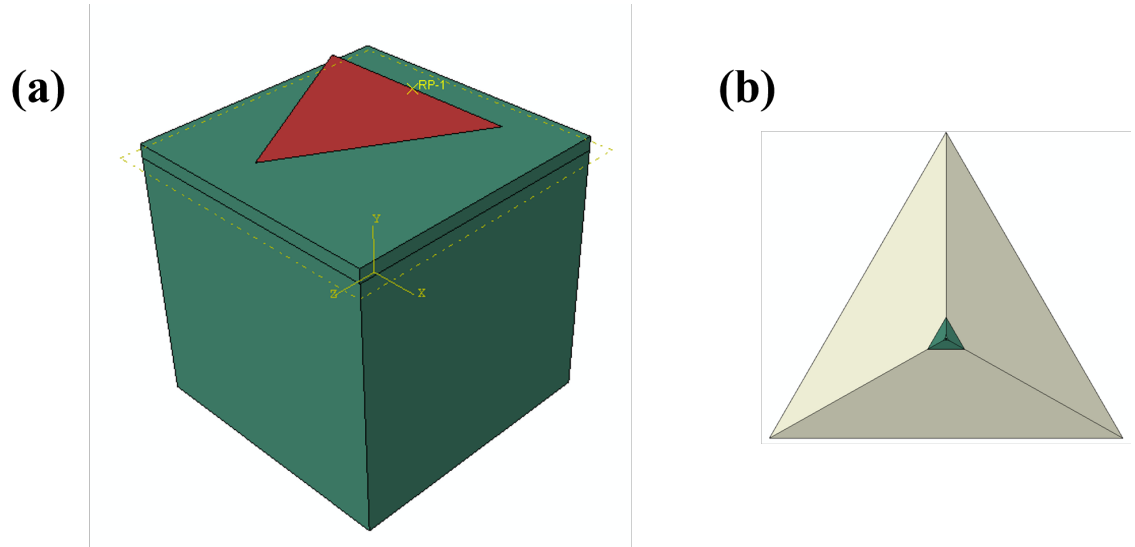


Figure 4.3: (a) FEM model of indentation; (b) detailed Berkovich indenter with consideration of tip bluntness

Table 4.1: Material properties

Parameter	Symbol	Value
Young's modulus (GPa)	E	200
Shear modulus (GPa) (Li & Soh, 2012)	G	42.1
Poisson's ratio (Li & Soh, 2012)	ν	0.36
Magnitude of the burgers vector (nm)	b	0.256
Lattice friction stress (MPa) (Olfe & Neuhäuser, 1988)	σ_0	0 (coarse-grained copper) 31.8 (nano-grained copper)
Hall-Petch constant (MPa $\cdot \mu\text{m}^{1/2}$) (Li & Soh, 2012)	k_{HP}	110
Geometric factor (Zhao, Zaiser, et al., 2021)	k_{mfp}^g	0.2
Proportionality factor (Zhao, Zaiser, et al., 2021)	$k_{\text{mfp}}^{\text{dis}}$	0.02
Dynamic recovery constant (Zhao, Zaiser, et al., 2021)	k_{ann}^0	2.1
Dynamic recovery exponent (Li & Soh, 2012)	n_0	21.25
References strain rate (s ⁻¹) (Li & Soh, 2012)	$\dot{\epsilon}_{\text{ref}}$	1
Reference grain size (μm) (Zhao, Zaiser, et al., 2021)	d_{ref}	1.5
Distance between slip lines (nm) (Zhao, Zaiser, et al., 2021)	λ	260
Initial dislocation density (m ⁻²) (Zhao, Zaiser, et al., 2021)	ρ_0	10^{13}
Johnson Cook damage parameters (Johnson & Cook, 1985)	d_1	0.54
	d_2	4.89

	d_3	-3.03
	d_4	0.014
	d_5	1.12

4.3 Results and discussion

4.3.1 Microhardness simulation on standalone homogeneous grained layers

In addition to uniaxial tensile experiments mentioned above, nano/micro indentation is also an important material characterisation method where only a small-scale sample is needed rather than a large-scale specimen (Koumoulos et al., 2015; Zha et al., 2019). Nano/micro indentation testing can thus be an appropriate alternative to large scale experiments especially when these can be difficult and complex to conduct or when material cost is an issue (Karimzadeh & Ayatollahi, 2012; Karimzadeh et al., 2019). Characterizing the hardness of HSLs is important as it is also a key material parameter. However, only a few experimental research reports have focussed on this material property for HSLs and none from a numerical modelling viewpoint. Huang et al. investigated the nanoindentation hardness of a copper-based HSL using a Berkovich indenter (C. X. Huang et al., 2018), while Ma et al. (Ma et al., 2016; Ma et al., 2015) and Wang et al. (Y. Wang et al., 2018) used a Vickers indenter to study the nanoindentation hardness of copper/bronze HSLs. Overall, these experiments revealed that the microstructure and composition difference across the interface between layers can result in a significant variation in hardness.

Microhardness simulations of homogenous grained layer with grain size of 4.8 μm and 100 nm were conducted using the developed framework. The simulated load-displacement curves are shown in Figure 4.4(a). It is obvious that the reaction force of the NG copper is significantly higher than that of the CG layer, as expected. The significant jumps observed in the force-displacement graphs during nanoscale indentation of copper are likely attributed to dislocation nucleation and propagation events. At the nanoscale, deformation

is dominated by discrete dislocation activities, which can cause sudden strain bursts, leading to abrupt changes in the force-displacement response. These phenomena are consistent with the stochastic nature of plastic deformation in crystalline materials at small length scales, as supported by prior studies in nano-mechanics.

The numerical micro indentation hardness H_i was calculated as $H_i = \frac{F_N}{A_p}$, where F_N is the normal reaction force and A_p is the projected area. The calculated results are shown in Figure 4.4(b) together with the experimentally obtained hardness values from (C. X. Huang et al., 2018). The numerical results correlate well with the experimental data as the simulated micro indentation hardness for the CG and the NG layer were 0.79 GPa and 2.43 GPa, respectively. The observation of the experimental data in this figure highlights the abrupt change in hardness between the different layers showing a prominent difference in material properties. The good correlation between the numerical and experimental results shows that the developed framework may not only be used in tensile simulations, but also in dynamic indentation process where relatively large compression and damage of material are involved.

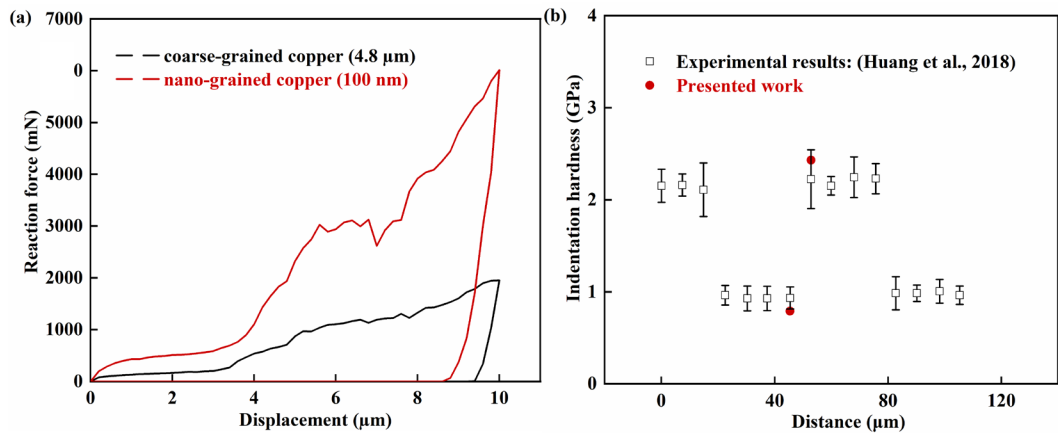


Figure 4.4: (a) Simulated reaction force-displacement curves during indentation and (b) comparison between numerical and experimental microhardness values for homogenous-grained CG and NG copper.

4.3.2 Uniaxial tensile responses of standalone

homogenous NG and CG copper layers

To further test the suitability of the developed numerical framework, uniaxial tensile simulations on homogenous grained copper were also carried out. The simulated stress-strain curves for copper with grain sizes of 4.8 μm , 4 μm and 100 nm are displayed in Figure 4.5(a). The experimental results reported in (C. X. Huang et al., 2018) and (Ma et al., 2015) are also plotted for comparison. It is observed from this figure that the simulated results agree well with the experimental data. One should notice that the IAZ data provided in this figure are merely for demonstration purpose as such a zone can only exist due to the interaction between the NG and CG layers. However, the IAZ results obtained in this simulation can still be compared against those reported in the simulation from (Zhao, Zaiser, et al., 2021) and thus are also included in the plot of Figure 4.5(a). It can be seen that the displayed stress-strain curves exhibit a strong grain size dependent behaviour. The NG copper shows no strain hardening and fails immediately after yield, i.e., around 530 MPa. This simulated behaviour agrees well with the experimental findings of (Champion et al., 2003; Dasharath & Mula, 2016; Y. F. Wang, M. S. Wang, et al., 2019; Zhao et al., 2006) for nanograined copper and also with those of (Liang et al., 2017) who investigated nano grained Ni. In contrast, and as expected, the stress in the CG layer keeps increasing with the applied strain post yield and although the value of stress is significantly lower than that in NG layer, a better ductility is observed.

The back stress was also output as a state variable and compared with the experimental values measured by the unloading-reloading experiments of (C. X. Huang et al., 2018). In particular, the evolution of back stress of homogenous copper layers with different grain size is displayed in Figure 4.5(b) to quantitatively explain the significant contribution of back stress to the mechanical response. The back stress strengthening, in other words the contribution of the back stress, is significantly higher than that of the effective stress caused by pure dislocation density strengthening (see equation 4.1). The back stress is mainly caused by the GNDs generated within each layer and piled-up near the

interfaces, i.e., IAZs. From Figure 4.5(b), it is observed that the back stress in the NG and CG layers saturates rapidly after initial yielding. In contrast, the back stress value of the IAZ keeps on increasing due to the continuous increase in piled-up dislocations. The simulated data suggest that the stress and back stress level of the IAZs can be as high as that in the NG layer when the strain is around 8 %. This indicates that the IAZs are crucial in the hardening behaviour of HSLs. It can also be seen from this figure that the back stress in the NG layer saturates around 347 MPa, which is in close alignment with the experimental results presented in (Y. Wang et al., 2018) and with the numerical results found in (Zhao, Zaiser, et al., 2021).

In the current formulation, back stress evolves during loading and unloading (or reverse loading) due to its dependence on the plastic strain history. During loading, back stress increases as dislocations accumulate and rearrange, creating internal stresses that oppose further deformation. Upon unloading or reverse loading, back stress partially relaxes as dislocations recover or reorganize, but a residual back stress may remain due to the irreversibility of plastic deformation. This behaviour reflects the kinematic hardening characteristics of the material, where back stress contributes to the Bauschinger effect and influences the material's response under cyclic loading conditions.

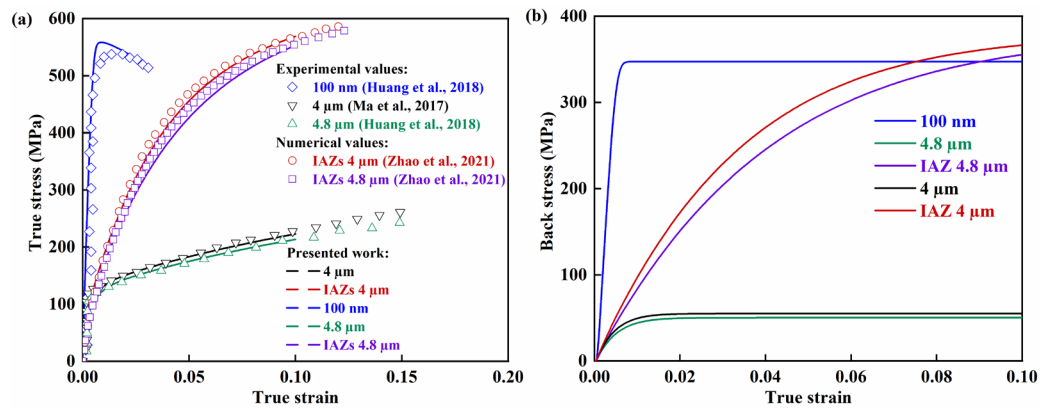


Figure 4.5: Simulated and experimental (a) true stress-true strain curves (b) back stress-true strain for homogenous-grained copper with grain sizes of 100 nm, 4 μm and 4.8 μm and for the IAZ.

The deformation at 10 % tensile strain for these three homogeneous standalone specimens taking into account of the JC damage factor are displayed in Figure 4.6. The necking is only observed in NG layer which indicates an early failure as was highlighted above with the data plotted in Figure 4.5(a). The corresponding JC damage accumulation factor at 10 % tensile strain in the NG layer, in the 4 μm CG layer and the 4.8 μm CG layer was found to be 0.06, 0.0064 and 0.0063, respectively. This shows quantitatively that the damage factor in the NG layer is one order of magnitude larger than that in the CG layers for this given percentage of tensile strain. These different damage conditions are the result of the smaller grain size in the NG layer which leads to this layer not being able to sustain dislocation accumulation. However, when such a layer is not standalone, i.e., when it is within a laminate structure, experimental results reported in the literature suggests that such stress concentration is reduced through the motion of dislocations in the CG layer near the interface i.e., the IAZ. Such dislocation-induced back stress and dislocation hardening explains why the stress in the IAZ keeps increasing with the strain as shown in Figure 4.5(b).

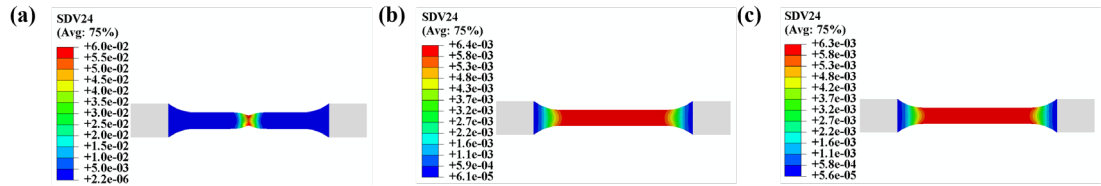


Figure 4.6: Specimen deformation and corresponding JC damage accumulation factor (i.e., SDV 24) at 10% tensile strain for homogenous copper layers with grain size of (a) 100 nm (b) 4 μm and (c) 4.8 μm using.

4.3.3 Quantitative analysis of uniaxial tensile responses of standalone IF

The developed model was adopted to investigate the effect of grain size on the tensile properties of homogenous grained Interstitial-Free (IF) steel. The dimension of the simulated dog-bone shaped specimen was adopted from Fang

et al. (Fang et al., 2011) for comparison purpose. The specimen was discretized into 1728 C3D8 elements, and the gauge section was refined to ensure mesh independence for the simulated results. The strain rate was set to 5×10^{-4} (X. Wu et al., 2014; Zhao et al., 2020) and the material properties used can be found in (Zhao et al., 2020). The stress (S11 direction), strain and all the state variables discussed in the next section were calculated by the average value of the gauge section. A Python script was compiled to extract the variables and plot the results for comparison with experimental values.

Uniaxial tensile stress-strain curves obtained from the simulation of the IF steel specimen with different grain size are displayed in Figure 4.7(a). The experimental results from Li et al. (Li et al., 2017) and Yang et al. (Yang et al., 2016) are also plotted for comparison. It is observed that the simulated stress-strain curves vary greatly in the range of grain size considered, i.e., 0.096 μm to 35 μm . In addition, it can also be said that the simulated results correlate well with the experimental data in terms of both initial yielding and subsequent strain hardening.

Experimental results from (Li et al., 2017) show that the strength of nano grained IF steel can be around 800 MPa but with limited ductility and almost no work-hardening before failure (Meyers et al., 2006). A similar trend can be observed in Figure 4.7(a). It is shown that when the grain size is 0.096 μm and 0.65 μm , the stress-strain curve tends to be flat right after yielding, which indicates that the strain hardening saturates immediately post-yield. As mentioned earlier, this is because dislocations rarely accumulate in the grain but are absorbed since smaller grains have less space for dislocation accumulation and slip. More interestingly, the premature necking phenomenon of the NG specimen is also captured as shown in Figure 4.7(a). The strong but brittle nature of NG material (Fang et al., 2011) which is a result of strain localization is predicted using the proposed constitutive model.

Figure 4.7(b) also shows that the back stress is grain-size dependent. The back stress saturates right after the initial yielding when the grain size is on the

nanoscale while it increases with strain when the grain size reaches the micro scale. This trend agrees well with the experimental results obtained on copper in (Mahato et al., 2016; H. Wang et al., 2018) where the back stress of CG copper was reported to increase with strain until 20% but saturated at a strain of 1% for the NG copper. It is also observed from Figure 4.7(b) that the simulated back stress increases with the reduction in grain size. This inverse dependence correlates well with the experimental findings and other numerical findings as well (S. Lu et al., 2019).

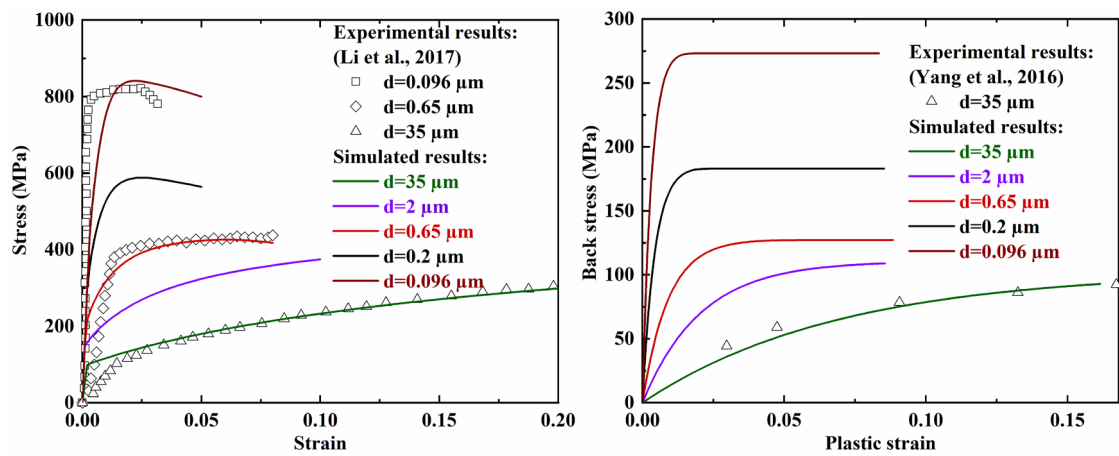


Figure 4.7: The predicted curves of (a) stress-strain and (b) back stress-plastic strain for homogeneously grained IF-steel with the grain size varies from 0.096 μm -35 μm .

Next, the respective contribution of GBs, SSDs, GNDs from both sample level and grain level and related back stress were output as state variables using the developed subroutine. In this way, the source of hardening and the respective influence from these different factors could be further investigated. The evolution of the contribution of different factors for the grain size 35 μm and 0.096 μm are displayed in Figure 4.8(a) and Figure 4.8(b) respectively. The final contribution of different factors to the final flow stress are displayed in Figure 4.9.

It is found that the flow stress is mainly dominated by the GBs strengthening, according to the H-P effect, and the back stress for both CG and NG IF steel.

However, the contribution of the SSDs for the CG IF steel is also important while negligible for the NG counterpart. This is because, the larger grain size allows more pile up accumulation within the grain thus leading to higher SSDs. The GNDs at the grain level tend to pile up in front of GBs and generate back stress on the grain level. A smaller grain size would lead to a larger density of GBs thus more piled-up GNDs on the grain level which explains the higher contribution of GND grain when the grain size is the smallest, i.e., 0.096 μm . The GNDs from the sample size rarely contributes to the flow stress. This is in accordance with the strain gradient plasticity (SGP) theory (Fleck & Hutchinson, 1997) in consideration of the millimetre (mm) scale of the specimen. Besides, Figure 4.8(b) displays that the back stress and GNDs form the grain level of the specimen with 0.096 μm grain size saturate right after yielding. This is because smaller grains do not have enough space for dislocation accumulation and slip.

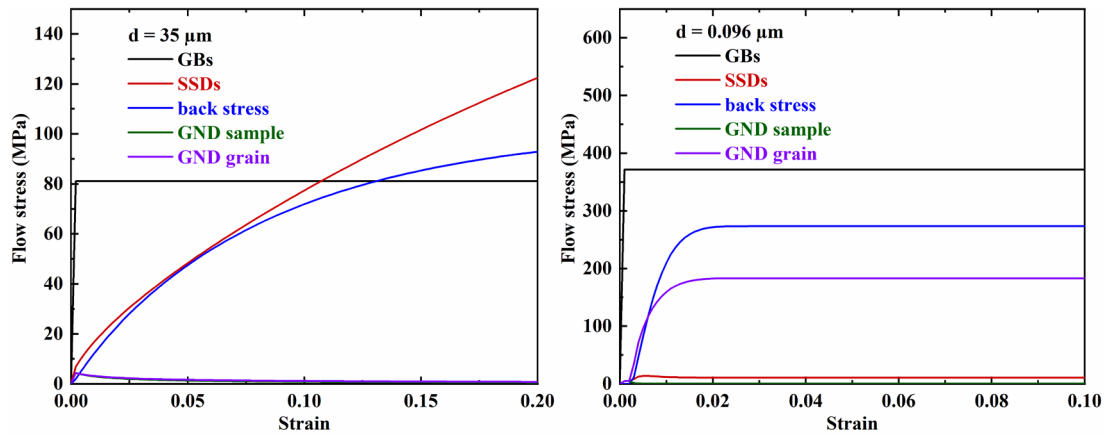


Figure 4.8: The evolution of contribution from different factors to the flow stress of homogenous IF-steel with different grain sizes, (a) $d=35 \mu\text{m}$, (b) $d=0.096 \mu\text{m}$.

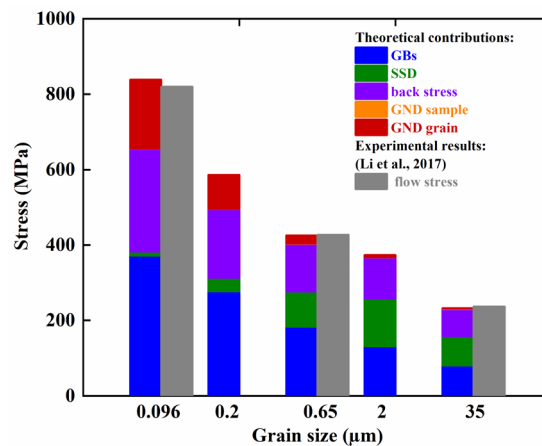


Figure 4.9: The contributions of different factors to the flow stress of homogenous IF-steel with different grain sizes.

4.3.4 Uniaxial tensile response of HSLs

The closeness of results between the experimental and numerical data obtained with the developed framework for standalone layers as reported in sections 4.3.1 to 4.3.3 provides some confidence that the numerical framework could be subsequently applied to further investigate the uniaxial tensile properties of HSLs with different layer thicknesses and NG layer volume content.

As mentioned in section 4.1, the rule of mixture (ROM) has been widely used to calculate the mechanical response of laminate structures made of different volume contents. When implementing the ROM (Zhao et al., 2022) for laminated composites, the yield stress, strain hardening, and uniform elongation are calculated as follows:

$$\sigma_{ys} = \sum V_i \sigma'_{i,ys} \quad (4.14)$$

$$\frac{d\sigma}{d\varepsilon} = \sum V_i \frac{d\sigma_i}{d\varepsilon} \quad (4.15)$$

$$\varepsilon_{UE} = \frac{\sum V_i \sigma_{i,UE} \varepsilon_{i,UE}}{\sum V_i \sigma_{i,UE}} \quad (4.16)$$

where V_i is the volume fraction of component i , $\sigma'_{i,ys}$ is the flow stress of component i alone at 0.2 % plastic strain of the composite sample, σ_i is the true stress of component i , σ and ε are the stress and strain of the composite sample and $\sigma_{i,UE}$, $\varepsilon_{i,UE}$ are true stress and true strain of the sample at necking point. As acknowledged earlier from published literature, the yield stress of HSLs using the ROM method correlates well with experimental values when the volume content of the IAZs is relatively low although the predicted strain hardening rate and uniform elongation are still smaller than the experimentally observed values (Ma et al., 2015; Zhao et al., 2022).

Because IAZs are not taken into account with the ROM method, Zhao et al. (Zhao, Zaiser, et al., 2021) proposed a modified ROM approach as shown in

equation (18) for calculating material properties of HSLs samples by volume average over the three regions, i.e. the NG layer, CG layer and the IAZs.

$$\sigma_{\text{laminite}} = \frac{\sigma_{\text{CG}}V_{\text{CG}} + \sigma_{\text{IAZ}}V_{\text{IAZ}} + \sigma_{\text{NG}}V_{\text{NG}}}{V_{\text{total}}} \quad (4.17)$$

where σ_{laminite} is the stress of the laminate and V_{total} is the total volume of the integrated sample, σ_{CG} , σ_{IAZ} and σ_{NS} are stresses for the three regions and V_{CG} , V_{IAZ} and V_{NG} are the volumes for these respective regions. Good correlation between theoretical modelling and experimental results were obtained by these authors. Therefore, in the following sub-section, the ROM approach and the modified ROM method from Zhao and co-workers (Zhao, Zaiser, et al., 2021) are implemented and analysed further.

- **Effect of layer thickness**

It has been widely verified experimentally that the strength-ductility balance of HSLs outperforms their homogeneous grained counterparts and that the layer thickness can be optimised to achieve superior properties (Fan et al., 2016; C. X. Huang et al., 2018). Herein, the effect of layer thickness on the tensile response of HSLs composed of copper layers with different thicknesses is investigated. The experimental data reported in (C. X. Huang et al., 2018) and the stress-strain curves simulated with the developed framework for copper-based HSLs with thickness values of 3.7 μm , 7.5 μm , 15 μm , 30 μm , 62 μm and 125 μm are displayed in Figure 4.10(a).

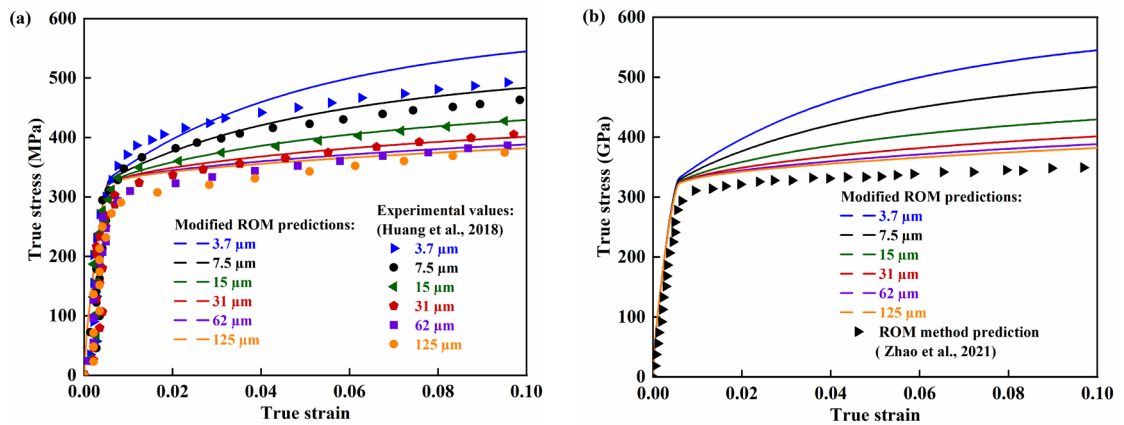


Figure 4.10: Plots of simulated stress-strain curves using modified ROM method for copper-based HSL composites with different layer thicknesses

against (a) experimental results from (C. X. Huang et al., 2018) and (b) ROM predictions from (Zhao, Zaiser, et al., 2021).

From this figure, an obvious layer thickness dependent behaviour is observed. More specifically, a smaller layer thickness leads to a higher stress. This outcome is expected as a smaller layer thickness leads to a higher IAZs density. In the case of the 3.7 μm layer thickness, the IAZs may also overlap. However, this high stress comes at the expense of a reduction in ductility since the effectiveness of back stress hardening is limited. Experiments reported in the literature also show that, during plastic deformation, emitted dislocations at the IAZs span on the order of several micrometres, which is consistent with the fact that the width of an IAZ is also the characteristic length in the strain gradient plasticity theory. Smaller interface spacing means a higher IAZs density which further leads to a higher density of GNDs. The stress concentration is further transmitted from the IAZs to inner parts of CG layer by dislocation activities. When the layer thickness is relatively small, i.e., 3.7 μm , this transmission is hindered by overlapping IAZs. Consecutively, the smaller the layer thickness, the more limited the ductility. The content of IAZs increase from 3.3 % to 100 % when the layer thickness decreases from 125 μm to 3.7 μm . X-ray tomography and digital image correlation data obtained in (Fan et al., 2017) reveal that the interface between layers in the laminate can act as local stress/strain transformer and delay crack initiation and propagation. It can be seen from Figure 4.10(a) that a lower IAZs content, namely when the layer thickness is larger than 15 μm , is associated with a better alignment of experimental and numerical results. On the other hand, when the IAZs content is relatively high, i.e., for layer thicknesses of 3.7 μm and 7.5 μm , obvious deviations can be observed which indicates that appropriate modelling of the IAZs and the interfaces are crucial in the tensile response of laminates.

The simulated results are also plotted and compared with results obtained using the ROM method as shown in Figure 4.10(b). As stated earlier, the IAZs

are not considered in the ROM method and the volume content the NG and CG layers remain constant, i.e., 50 % for each layer regardless of the changing thickness. This inevitably leads to overlapping predictions using this method as seen in this figure. Besides, this figure illustrates that the ROM-based predictions are smaller than the experimental data. Again, this indicates the crucial role of IAZs in strengthening the laminates.

Considering the significant role that back stress plays in hardening gradient and laminate structures (Wu & Zhu, 2017; Yang et al., 2016), the back stress for laminates fabricated with different layer thickness is also analysed in the presented work. In Figure 4.11(a), the simulated back stress is plotted and compared with experimental data from (C. X. Huang et al., 2018). It can be seen that the evolution of the back stress for laminates with the considered layer thicknesses of 7.5 μm and 31 μm agree well with the experiments and that a smaller layer thickness leads to a higher back stress. This is due to the fact that the back stress is mainly caused by GNDs generation and pile-ups near the interfaces. A larger amount of GNDs is expected with larger interface densities i.e., with smaller layer thickness. It can also be observed from Figure 4.11(a) that the back stress increases drastically until 1% true strain and tends to saturate afterwards. This indicates that the back stress hardening is most effective in the early stage of deformation which also correlates well with experimental findings (C. X. Huang et al., 2018). The calculated effective stress $\alpha Gb\sqrt{\rho}$ (Gao et al., 1999) is also plotted and compared with experimental findings from (C. X. Huang et al., 2018) as shown in Figure 4.11(b). It can be seen that the back stress is significantly higher than the effective stress which is also aligned with experimental findings reported in (Ren et al., 2022). The simulated trends are in good agreement with the experimental data, although discrepancies with exact values are noticed, especially for the effective stress, which might stem from the texture changing during the manufacturing process.

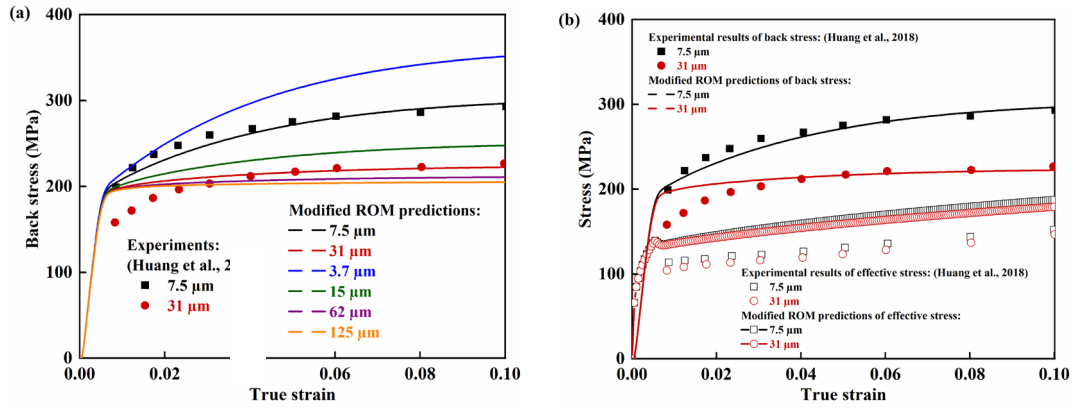


Figure 4.11: Evolution of (a) back stress and (b) effective stress for the simulated copper-based HSLs with different layer thickness and comparison with experimental findings from (C. X. Huang et al., 2018).

- **Effect of NG volume content**

The developed model was further applied to study the uniaxial tensile properties of copper-based HSLs with different NG volume content and the simulated results compared against the experimental investigation presented in (Ma et al., 2015). The modelling details follow the experimental set up described in (Ma et al., 2015) for post mortem comparisons; specifically, the volume content of the NG layer is set to 0.1, 0.22 and 0.47 while the thickness of the specimen was 600 μm.

Figure 4.12 shows the comparisons of the stress-strain curves with different NG volume contents between the theoretical predictions obtained in this work by implementing 1) the modified ROM method, 2) the classical ROM predictions (Zhao, Zaiser, et al., 2021) and 3) the experimental results (Ma et al., 2015). The predicted results using the modified ROM method are slightly larger than those from the classical ROM predictions in all cases. This is because the effect of IAZs is not included in the ROM method. Generally, the simulated stress-strain curves for all considered NG volume contents agree well with the experimental results (Ma et al., 2015) and the ROM predictions (Zhao, Zaiser, et al., 2021). The reason why the ROM method is also well-aligned with the experimental results here is likely due to the fact that the IAZs take up only 1.9 %, 2.1 % and 3.1 % of

the CG layer, for the respective volume contents investigated, and thus, can be considered to have a negligible effect on the overall properties.

The model predictions match the experimental data well in the initial stages of deformation (elastic regions). However, as the strain increases, the predicted stress-strain curves tend to deviate slightly from the experimental results. This suggests that the model captures the initial deformation behaviour but may not fully account for the complex deformation mechanisms that dominate at higher strains. The constitutive model is based on dislocation density evolution and back stress mechanisms, which are effective in describing the initial deformation. However, at higher strains, other factors such as dynamic recovery, grain rotation, and damage mechanisms (e.g., void formation or microcracking) may become significant. These factors are not explicitly included in the current model, leading to discrepancies at larger strains. While the current model provides a good approximation of the mechanical behaviour of hetero-structured laminates, the discrepancies observed in Figure 4.12 indicate that further refinements, including more mechanism and realistic consideration of interfaces, are needed to fully capture the complex deformation mechanisms at higher strains. Acknowledging these limitations including is crucial for guiding future improvements to the model and ensuring its applicability to a wider range of loading conditions and material systems.

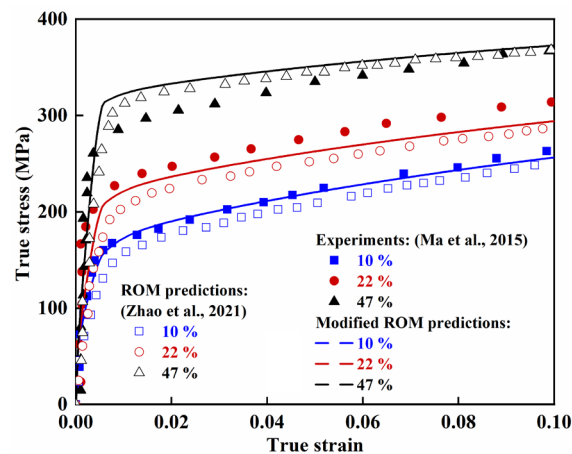


Figure 4.12: Comparison of the results obtained between the modified ROM method predictions, ROM results from (Zhao, Zaiser, et al., 2021) and

experimental results from (Ma et al., 2015) for laminates with different volume content of NG layer.

- *Outcomes from the integrated FEM model developed in this research*

The previous two sections investigated the effectiveness of the classical ROM approach and the modified ROM method from Zhao and co-workers (Zhao, Zaiser, et al., 2021) to quantitatively predict the effect of the layer thickness and the NG volume content on the tensile response of copper-based HSLs. However, experimental data (Ma et al., 2015) show that the synergetic effect of the NG and CG layers would produce a more significant strengthening than that inferred by the weight-based mathematical formulae that characterise both methods. Besides, the CG and NG layers experience different damage characteristics when considered as standalone entities compared to when they compose a HSL stack. To shed further light on the constraints and the synergy of the NG and CG layers, an integrated finite element method (FEM) model is developed to study the mechanical response of the ‘sandwich structure’ of HSL materials rather than studying the separate standalone layers.

One should notice that for homogenous grained copper, a Taylor constant M of 3.06 is adopted for the CG, the NG and the IAZ material. However, the laminates are manufactured by HPT, rolling and annealing which would result in a different grain size for final specimens, especially for the NG layers (C. X. Huang et al., 2018; Zhao, Zaiser, et al., 2021). In consideration of this, a Taylor constant of 2.45 is adopted for the NG layer in the laminates following the study presented in (Starink & Wang, 2003) while the rest of the material properties remain unchanged. The model consists of three regions, namely the CG, the NG and the IAZs, as previously illustrated in Figure 4.1(b). These regions were geometrically modelled to adhere to the experimental conditions of (C. X. Huang et al., 2018; Ma et al., 2015) and were meshed suitably. The predicted stress-strain curves using the integrated FEM model of copper-based HSLs with different layer thicknesses and NG volume contents are plotted in Figure 4,13.

This figure also includes experimental data from (C. X. Huang et al., 2018; Ma et al., 2015) for comparison purpose. The simulated stress-strain curves with different layer thicknesses correlate relatively well with experimental values. Similar to what was found earlier when implementing the modified ROM method from Zhao and co-workers (Zhao, Zaiser, et al., 2021), the larger the layer thickness, the better the approximation. This indicates again the crucial role of interfaces and the IAZ. For the laminates with different NG volume contents, i.e., Figure 4.13(b), the simulated stress-strain curves also agree relatively well with experimental data for all considered scenarios. As discussed earlier, the IAZs content considered for all simulations in this figure is lower than that for the simulations Figure 4.13(a) where the layer thickness is small and thus, a better correlation can be achieved. This figure also indicates that the mutual constraints between the NG and CG layer are negligible in the scenarios modelled in Figure 4.13(b) because the results displayed are close to the results in Figure 4.12.

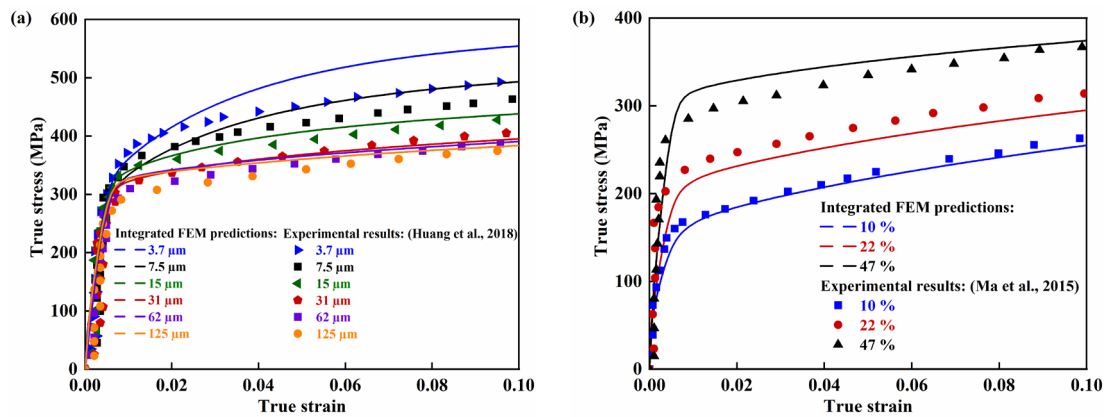


Figure 4.13: (a) Plots of simulated stress-strain curves for copper-based HSLs using the integrated FE model with (a) different layer thicknesses against experimental results from (C. X. Huang et al., 2018) and (b) different NG volume contents against experimental results from (Ma et al., 2015) .

To investigate the mutual interactions between the NG and the CG layers, the lateral stress distribution, of the laminates with 10%, 22% and 47% NG volume content at the true strain of 0.5 % is shown in Figure 4.14 together with the

numerical results from Zhao et al., (Zhao, Zaiser, et al., 2021) for comparison. Experimental observations at this stage report that the CG layer has yielded while the deformation in the NG layer is still pre-yield, i.e., elastic (Wu & Zhu, 2017). The selected simulation path in the presented work corresponds to the middle section of the specimen along the thickness direction as shown in the inset of Figure 4.14(b). The presented results agree well with the numerical findings of (Zhao, Zaiser, et al., 2021) where 5 different paths on the cross section were selected. The lateral stress is negative in the NG region while positive in the CG region. This reveals the severe ‘shrinkage’ of the NG layer along the lateral direction and the multiaxial loading in the HSL structure. This incompatibility between the NG and the CG layers during deformation was also reported in the experiments conducted in (C. X. Huang et al., 2018). The lateral stress distribution in the CG layer was found to be around 5 MPa which is close to the results reported in (X. L. Wu et al., 2014; Zhao et al., 2020), while the lateral stress distribution in the NG layer can be relatively high, such as -25 MPa. It can also be observed from Figure 4.14(b) that the smaller the NG volume content, the larger the difference in lateral stress between the CG and NG layers. This indicates that a smaller NG volume content would lead to a larger incompatibility between both layers. This bi-axial stress state can activate more slip systems and contributes to extra strengthening beyond the predictions made using the ROM method (X. Wu et al., 2014).

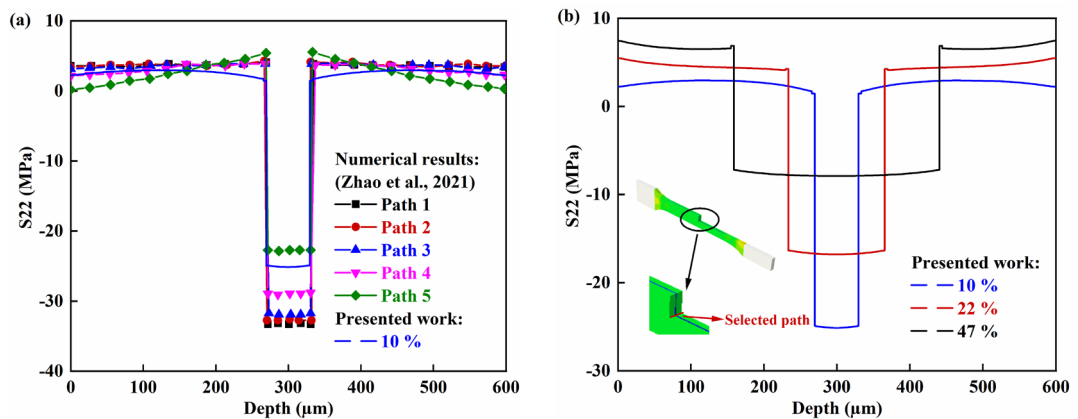


Figure 4.14: (a) Comparisons of simulated lateral stress distribution of 10 % NG volume content of a copper-based HSL at the true strain of 0.5 % with numerical

results presented in (Zhao, Zaiser, et al., 2021); (b) lateral stress distribution of simulated copper-based HSLs with different NG volume contents at the true strain of 0.5 %.

In the integrated FEM model developed here, the NG layer in the HSL displays no necking in the first 10 % true strain (see Figure 4.15(b)) while the stand-alone NG layer started necking at 0.4% true strain (see earlier Figure 4.5(a)). A similar phenomenon was observed in the experiments conducted in (Ma et al., 2015) where the NG layer in the laminates started necking at the strain of 12% while their stand-alone NG layer counterparts yielded at an early strain of 0.7 %. The maximum JC damage accumulation factor in the NG layer of the copper based HSL composite was simulated to be around 0.0065 for all layer thicknesses considered at a strain of 10%, as shown in Figure 4.15(a). This is significantly smaller than that in standalone NG layer, which was found to be 0.06 (c.f. Figure 4.6(a)) for the same value of strain. This is explained by the fact that early necking of the NG layer in HSL structures is suppressed by the CG layers through the formation of two IAZs on both sides (Wu & Zhu, 2017). The early tensile failure exhibited in a standalone NG specimen is thus avoided. The damage accumulation factor in the NG layer for different thicknesses is also displayed with Figure 4.15(a). It can be seen that the smaller the layer thickness, then the smaller the damage factor. This indicates that the NG layer is protected by the neighbouring layers since the smaller layer thickness means a larger interface/IAZs density. The damage factor in the NG layer for copper-based HSLs with different volume content is given with Figure 4.15(b). As reported above, the damage factor in this situation is about one magnitude smaller than that for a standalone NG layer, which indicates that the neighbouring IAZs and CG layer alleviates the stress concentration. However, with the increase in the volume content of the NG layer, the stress concentration cannot ultimately be lessened. This leads to a larger damage factor and thus, an earlier failure as observed in experiments conducted in (Ma et al., 2015).

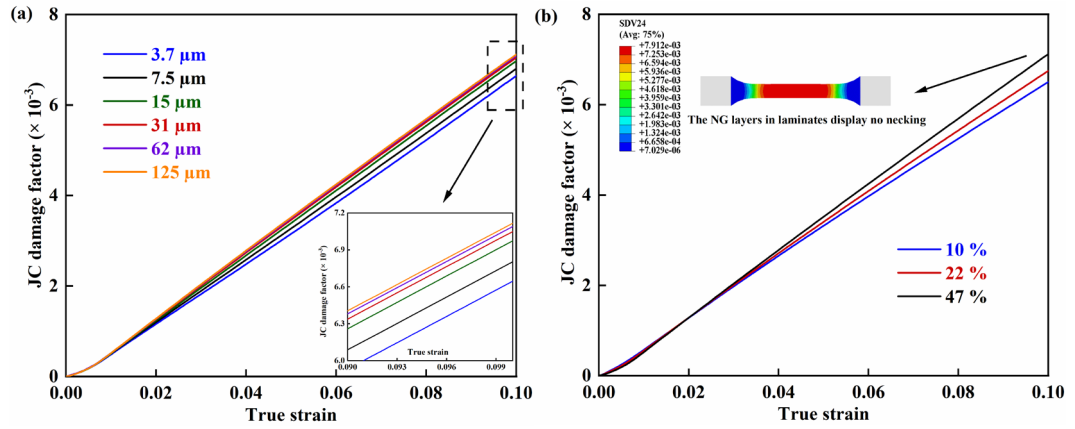


Figure 4.15: (a) The simulated JC damage accumulation factor of the NG layer in HSLs with layers of different thicknesses, (b) The simulated JC damage accumulation factor of the NG layer in HSLs with 10 %, 22 % and 47 % NG volume content using the integrated FE model developed in this research.

The numerical results presented in this work using the modified ROM method from Zhao and co-workers (Zhao, Zaiser, et al., 2021) and the developed integrated FEM model, including the output stress-strain curves, microhardness, back stress and JC damage factors correlate well with the corresponding experimental observations. However, the simulated stress-strain curves in Figure 4.10(a) and 4.13(a) for the copper-based HSL with different layer thicknesses still somewhat show some degree of discrepancy with experimental values. A first possible reason behind this outcome may be due to the uncertainty around the thickness of IAZs as various values are reported in the literature, i.e. 5 μm to 6 μm in (C. X. Huang et al., 2018) and the size of one coarse grain in (Zhao, Zaiser, et al., 2021). A second possible source of error may be linked to the uncertainty in the value of the Poisson's ratio of the CG layer in the integrated HSL structure simulations. More specifically, findings from (X. Wu et al., 2014) suggest that the Poisson's ratio of this layer changed from 0.36 to 0.5 to accommodate the mechanical incompatibility between layers. As a result, the uniaxial tensile loading turns into a bi-axial one and more slip systems are activated which contribute to the extra strengthening (X. L. Wu et al., 2014). The interaction between the NG and CG layers is found to make a

significant contribution to back stress (Y. Wang et al., 2018) and this synergetic hardening behaviour needs to be further investigated. In addition, the cohesive interfaces between different layers were not included but modelled as a whole part in this research which will ineluctably lead to deviations of the laminate properties.

While this work focusses on the heterogenous deformation-induced hardening, the hardening of such structures (Wu et al., 2020) might also stem from various sources such as the additive effect of individual layer by forest hardening as in gradient structures, compressive residual stress induced strain hardening, and partly recovered forest dislocation hardening due to the change of stress state in the NG layer. The change in grain size in different layers during the deformation process and due to the manufacturing process as well as nanotwin boundary-mediated strain hardening might contribute to the deviations as well. For example, grain coarsening in the NG layer of gradient copper was observed in (Chen et al., 2017) and ‘strain softening’ was induced as a result, and consequently, an enhanced strength-ductility synergy was achieved. In future studies, the evolution of grain size should be modelled as a function of temperature and stress-strain rate to achieve more accurate predictions. In addition to this, damage initiation and fracture are a complicated process especially in such ‘sandwich’ structures where necking-delayed ductile mode to necking-inhibited brittle mode transition (Liang et al., 2017), interface delamination and slip bands activities (Zhao et al., 2022) are involved. The inclusion of cohesive interfaces with reasonable progressive failure criterion has the potential to lead to further advances when investigating this problem.

4.4 Conclusions

In the presented work, a multiple physical mechanism based constitutive model coupled with the JC damage criterion was developed to simulate the deformation of HSLs and particularly, to investigate and quantify the internal damage evolution in such structures. The evolution of GNDs, SSDs and

resulting back stress were taken into account using dislocation pile up theory. The simulated microhardness, stress-strain curves and back stress evolution agreed well with published experimental results. The important conclusions that can be drawn from this work are as follows:

(1) The developed HSL simulation model is considered to outperform the traditional ROM and the modified ROM methods due to its ability to investigate the interactive constraints between the CG and NG layers and to quantify the damage conditions throughout the deformation process.

(2) Given the ability of the developed model to evaluate the damage accumulation factor in the NG layer, simulation outcomes were obtained which aligned with the following known experimental observations: 1) the smaller the layer thickness, then the smaller the internal damage and 2) the internal damage increases with the increase in volume content of the NG layer.

(3) For a set simulated strain of 10%, it was found that the damage accumulation factor in the NG layer was 10 times lower than that in a stand-alone NG layer not sandwiched between two CG layers. This confirms that good protection of the NG layers is provided by the CG layers during deformation in HSLs.

(4) Deviations from experimental data were observed when predicting the stress-strain curves of HSLs with smaller layer thickness values using both the developed model and the modified ROM method, as displayed in Figure 4.7 and Figure 4.10. The observed discrepancies may result from the complex interactions of multiple mechanisms as well as the lack of consideration for grain-level deformation and orientation effects. It is anticipated that the inclusion of interfaces and a reasonable traction-separation progressive failure law in the proposed FEM model should have the potential to address this issue. It is anticipated that the developed framework could be easily adopted to simulate other metallic heterogeneous materials especially in the context of dynamic manufacturing processes, such as forming. Thus, the proposed framework should support the application of metallic laminates, and potentially gradient metallic structures too, by supporting the optimal design

of such materials.

Chapter 5 A full-field non-local crystal plasticity investigation of bi-layered HEA

5.1 Introduction

In this Chapter, the study from Fu and co-workers (Fu, Huang, et al., 2022), who fabricated bi-layered high entropy alloy (HEA) specimens utilising laser shock peening, was adopted as the benchmark against which the results of the developed model could be compared. Initially, uniaxial tensile simulations on homogenous grained HEAs with grain sizes ranging from 5 μm to 100 μm were conducted to validate the model. Subsequently, the proposed framework was applied to simulate the uniaxial tensile behaviour of a heterostructured HEA and the obtained results compared to the experimental data given in (Fu, Huang, et al., 2022). By comparing simulation results with experimental findings, the deformation characteristics and strengthening mechanism of heterostructured materials could be comprehensively discussed.

5.2 Numerical framework and FEM model

In this section, the development and implementation of a non-local CPFEM framework are presented. The framework incorporates essential components, including the slip model, the hardening model, and the calculation of GNDs, which contribute to the resultant back stress. Additionally, the implementation details of the model are discussed, providing a foundation for its application in simulating material behaviour at the microscale.

5.2.1 CPFEM constitutive model

- **Slip model**

The shear strain rate $\dot{\gamma}^a$ generated by the dislocation motion of slip system a is expressed as (Ashby, 1970):

$$\dot{\gamma}^a = \dot{\gamma}_0 \left(\frac{|\tau^a|}{\tau_c^a} \right)^n \text{sgn}(\tau^a) \quad (5.1)$$

where $\dot{\gamma}_0$ is the reference shear rate, n is the power law exponent, τ^a is the shear stress acting on the slip system and τ_c^a is the critical resolved shear stress (CRSS) which describes resistance to gliding dislocations. The CRSS can be further formulated as (McCabe et al., 2010):

$$\tau_c^a = (\tau_c^a)^0 + \tau_{for}^a + \tau_{sub}^a \quad (5.2)$$

where $(\tau_c^a)^0$ is the initial CRSS, τ_{for}^a is the forest dislocation interaction stress and τ_{sub}^a is the dislocation substructure interaction stress.

- **Hardening model**

It was pointed out in (Wulfinghoff & Böhlke, 2015) that meaningful boundary conditions for the dislocation evolution equations are required if they are to be applied to problems with more complex interfaces or open boundaries. Considering difference in properties between finer and coarser grain regions, the Kocks-Mecking-Estrin (KME) dislocation density model was adopted to account for dislocations generation and annihilation. Thus, the evolution of forest density for slip system a , $\Delta\rho_{for}^a$, is as follows (Mecking & Kocks, 1981):

$$\Delta\rho_{for}^a = \left(k_1 \sqrt{\rho_{for}^a} - k_2(\dot{\epsilon}, T) \rho_{for}^a \right) |\dot{\gamma}^a| \Delta t \quad (5.3)$$

where k_1 is the hardening constant, Δt is the step time increment and k_2 is the annihilation constant. $k_1 \sqrt{\rho_{for}^a}$ represents the rate of dislocation storage by statistical trapping of gliding dislocations by forest obstacles. $k_2(\dot{\epsilon}, T) \rho_{for}^a$ accounts for dynamic recovery by thermally activated mechanisms such as dislocation cross-slip and climb, which can be obtained through (McCabe et al., 2010):

$$k_2 = k_1 \frac{\zeta b^a}{g^a} \left(1 - \frac{K_B T}{D^a (b^a)^3} \ln \frac{\dot{\epsilon}}{\dot{\epsilon}_0} \right) \quad (5.4)$$

where g^a is the effective activation enthalpy, D^a is the drag stress, $\dot{\epsilon}_0$ reference slip rate. The hardening caused by forest dislocations τ_{for}^a can be expressed as:

$$\tau_{for}^a = \zeta G^a b^a \sqrt{\rho_{for}^a} \quad (5.5)$$

where ζ is the dislocation interaction parameter, G^a is the shear modulus and b^a is the magnitude of the Burgers vector. Dynamic recovery is often associated with thermal activation of dislocation cross-slip and climb, and the formation of dislocation substructures is concomitant with these recovery processes. The term substructure dislocation is used to describe dislocations that are statistically stored within the substructure due to deformation and contribute to the total dislocation density. Substructure dislocations primarily arise from local plastic deformation processes and are essential for capturing the hardening behaviour. As a consequence, the rate of substructure dislocation $\Delta\rho_{sub}$ development was coupled to the rate of recovery of all active dislocations through (McCabe et al., 2010):

$$\Delta\rho_{sub} = q \sum_a f^a \sqrt{\rho_{sub}} k_2 \rho_{for}^a |\dot{\gamma}^a| \Delta t \quad (5.6)$$

where q is the rate coefficient, f^a is the fraction of recovery rate that leads to substructure formation. Dislocation dynamics simulations show that the contribution to hardening by dislocations stored within substructures, such as cell walls, can be written with the following extended Taylor law (McCabe et al., 2010):

$$\tau_{sub} = k_{sub} G^a b^a \sqrt{\rho_{sub}} \ln \left(\frac{1}{b^a \sqrt{\rho_{sub}}} \right) \quad (5.7)$$

where k_{sub} is an empirical parameter.

5.2.2 GND calculation

The GND density is calculated from Nye's dislocation density tensor Λ (Nye, 1953), which can be expressed based on the curl of plastic deformation gradient

\mathbf{F}^P (Arsenlis & Parks, 1999; Das et al., 2018; Demir et al., 2024b):

$$\Lambda = (\nabla \times \mathbf{F}^P)^T \quad (5.8)$$

Thus, the GND density ρ_{GND} can be obtained as:

$$\rho_{GND} = [\mathbf{A}]^T ([\mathbf{A}][\mathbf{A}]^T)^{-1} \{\Lambda\} \quad (5.9)$$

where $[\mathbf{A}]$ is the linear operator matrix calculated based on slip line direction \mathbf{t} , slip plane normal \mathbf{n} and Burgers vector \mathbf{b} . $\{\Lambda\}$ is the vector form of the Nye's dislocation density tensor Λ . The GND density is calculated using singular value decomposition, followed by inversion to determine the dislocation densities. The solution is constrained to the active slip systems (Demir et al., 2024a), which are identified based on the total slip magnitude of each slip system.

Via incorporating the effect of GNDs, the forest dislocation density ρ_{for}^a in equation (5.3) can be further modified by the projection of GNDs:

$$\rho_{for}^a = \Delta\rho_{for}^a + \sum_b |\mathbf{n}^a \cdot \mathbf{t}_e^b| |\rho_{GND,e}^b| + |\mathbf{n}^a \cdot \mathbf{s}_s^b| |\rho_{GND,s}^b| \quad (5.10)$$

where \mathbf{t}^b is the dislocation line direction, \mathbf{n}^a is the slip plane normal, \mathbf{s}^b is the slip direction. The calculation of hardening caused by forest dislocation τ_{for}^a in equation (5.5) and substructure dislocations $\Delta\rho_{sub}$ in equation (5.6) are updated accordingly. ρ_{tot}^a can be obtained as:

$$\Delta\rho_{sub} = q \sum_a f^a \sqrt{\rho_{sub}} k_2 \rho_{for}^a |\dot{\gamma}^a| \Delta t \quad (5.11)$$

A more detailed introduction regarding the fundamental aspects of the developed numerical framework including the definition of grain rotation can be found in (Beausir et al., 2007; Demir et al., 2024a).

5.2.3 Back stress model

Physically, the back stress results from the spatially heterogeneous distribution of GNDs (Zhang, Zhao, et al., 2023; Yin Zhang et al., 2024). High energy X-ray diffraction microscopy techniques proved that even at lower length-scale, the GND back stress model is in close agreement with the thermodynamic origin

of back stress in a pure continuum mechanics framework of crystal plasticity constitutive relations (Bandyopadhyay et al., 2021). Besides, it involves only one unknown parameter and enables one to initialise back stress at each point within a microstructure in the crystal plasticity analysis (Bandyopadhyay et al., 2021). This is favourable considering the significant amount of initial dislocations induced by laser shock peening in the experimental work from Fu et al. (Fu, Huang, et al., 2022), which is considered here for evaluating the outcomes of the model. In the context of this work, where the focus is on developing a full-field non-local crystal plasticity finite element model to investigate cooperative strengthening mechanisms in metallic heterostructured materials, it is of interest to probe the effect of GND-induced kinematic hardening on the strain hardening behaviour. Thus, following the work in (Kapoor et al., 2018), the back stress σ^b caused by GND density on slip system ρ_{GND}^a was calculated as:

$$\sigma^b = KG^a b^a \sqrt{\rho_{GND}^a} \quad (5.12)$$

where, K is a scaling constant. the shear modulus G^a used for each slip system is the macroscopic shear modulus of the material, which is assumed to be the same for all slip systems. It is noted that the back stress in Eq. (12) is formulated based on the magnitude of stress and does not explicitly consider its sign. This approach aligns with the assumption that the kinematic hardening evolution is driven by the absolute value of plastic deformation rather than the direction of the stress tensor components. This simplification is consistent with similar models in the literature work (Kapoor et al., 2018).

Equation (5.1) was further modified as:

$$\dot{\gamma}^a = \dot{\gamma}_0 \left(\frac{|\tau^a - \sigma^b|}{\tau_c^a} \right)^n \text{sgn}(\tau^a - \sigma^b) \quad (5.13)$$

Thus, this model connects the mathematical description of kinematic hardening, in the context of crystal plasticity, to the underlying mechanisms at the microscopic level.

5.2.4 Damage model

Stress mismatch between two regions results in high triaxiality (Liu et al., 2017; Yu et al., 2018), which is a key damage characteristic (Tvergaard et al., 1990). Thus, a reasonable damage model should be developed to investigate damage nucleation in heterostructured materials. Herein, the JC dynamic failure model, proven to be robust for microscale processes affected by large deformations (Lai et al., 2008; Z. Wang et al., 2019), especially within a CPFEM framework (Boubaker et al., 2021), was adopted as the damage criterion. The JC failure model comprehensively includes the effect of strain hardening, strain rate and temperature. More specifically, the JC failure model is based on the calculation of the equivalent plastic strain, which is expressed as introduced earlier in equation (3.16). A summation of incremental failure strain $\Delta \bar{\epsilon}_f^{pl}$ was carried out over all increments for assessing the failure criterion, ω (Johnson & Cook, 1985), as shown in equation (3.17).

5.2.5 Model implementation

The developed non-local CPFEM model was implemented into a user-defined material subroutine (UMAT) (Dunne et al., 2007; Hardie et al., 2023; Liang & Dunne, 2009). The tensile simulations were performed with the commercial FEM software ABAQUS. Table 1 shows the material properties adopted in this work. As mentioned earlier, the experimental data used in this research to validate the developed model were those reported by Fu and co-workers (Fu, Huang, et al., 2022), who investigated the heterostructured CrFeCoNiMn_{0.75}Cu_{0.25} high entropy alloy. The studied HEA has face centred cubic (FCC) crystal structure, and the dominant slip system is 111 110. The readers should note that in crystalline materials, deformation typically occurs through the activation of multiple slip families rather than just one. The use of a single slip system simplifies the physical reality of plastic deformation, as it ignores the complex interactions between multiple slip families that are often

observed in real materials. As material properties for this specific alloy are not all available from the literature, care was taken to select values relevant for this HEA.

Table 5.1: Material properties.

Parameter	Symbol	Value
Elastic moduli (Fang et al., 2019)	C_{11}	264.6 GPa
	C_{12}	184.8 GPa
	C_{44}	112.9 GPa
Magnitude of the Burgers vector (Gao et al., 2020)	b	0.252 nm
Power law exponent	n	10
Initial CRSS	τ_c^0	101.5 MPa
Reference slip rate	$\dot{\gamma}_0$	0.001
Hardening constant	k_1	1
Dislocation interaction parameter	ζ	0.9
Effective activation enthalpy (Gao et al., 2020)	g^a	3×10^{-4}
Drag stress (Gao et al., 2020)	D^a	500 MPa
Reference slip rate	$\dot{\epsilon}_0$	1×10^7
Rate coefficient (McCabe et al., 2010)	q	4
Fraction of recovery rate	f^a	20
Empirical parameter	k_{sub}	0.086
References strain rate (s^{-1})	$\dot{\epsilon}_{ref}$	1
Initial GND	ρ_0	10^{13}
Scaling constant of back stress (Kapoor et al., 2018)	K	0.4
Johnson Cook damage parameters (Johnson & Cook, 1985)	d_1	0.54
	d_2	4.89
	d_3	-3.03
	d_4	0.014
	d_5	1.12

5.3 Uniaxial tensile response of homogeneous HEA specimens

Before investigating the deformation behaviour of the bi-layered HEA specimen considered in this work, the tensile response of each separate homogeneous polycrystalline regions was simulated first. In this section, simulations were carried out to validate the ability of the developed model to capture the GND-induced effect and corresponding mechanisms. In particular, five homogeneous-grained models with grain size ranging from 5 μm to 100 μm were considered.

5.3.1 CPFEM modelling

A 2D model was employed to ease the computational burden. In particular, representative volume elements (RVEs) consisting of 32 randomly oriented grains as displayed in Figure 5.1(a), were employed for the homogeneous-grained material simulations. The initial flow stress of FCC polycrystals depends both on the grain size and the initial dislocation density (Zhang, Zhao, et al., 2023) and samples with the same grain size and dislocation density distribution, but randomly generated grain orientation, exhibit varied mechanical properties. In order to avoid the influence of the initial dislocation density, it was set to 0.1/ μm^2 in all cases studied in this section. In addition, the grain orientation was kept constant between the different samples simulated here. The polycrystalline models with varying grain size were generated using the open-source software Neper (Quey et al., 2011). They displayed the same grain morphology and were discretized using CPS4 elements. In other words, the parameters used for the validation work reported in this section, including grain orientations and initial dislocation density, were all identical apart from the grain size. In this way, the effect of the grain size could be isolated and effectively studied between the five homogeneous-grained models considered. An initial mesh sensitivity study showed that the mesh resolution adopted was sufficiently high for the modelled homogeneous

polycrystals, as shown in the Appendix. To simulate uniaxial tensile deformation, displacement constraints of $U_x = 0$ and $U_y = 0$ were applied on the lower and left surfaces, respectively as displayed in Figure 5.1(a). Furthermore, for ease of data post-processing, a coupling constraint was applied to all the nodes on the top surface and the reference point to ensure that their displacements and reaction forces along the y-axis were the same. The tensile displacement was applied at the reference point at a constant strain rate of $7.14 \times 10^{-4} \text{ s}^{-1}$, aligned the experimental loading condition reported in (Fu, Huang, et al., 2022) by Fu and co-workers. The material parameters adopted for this constitutive model were summarised earlier in Table 5.1.

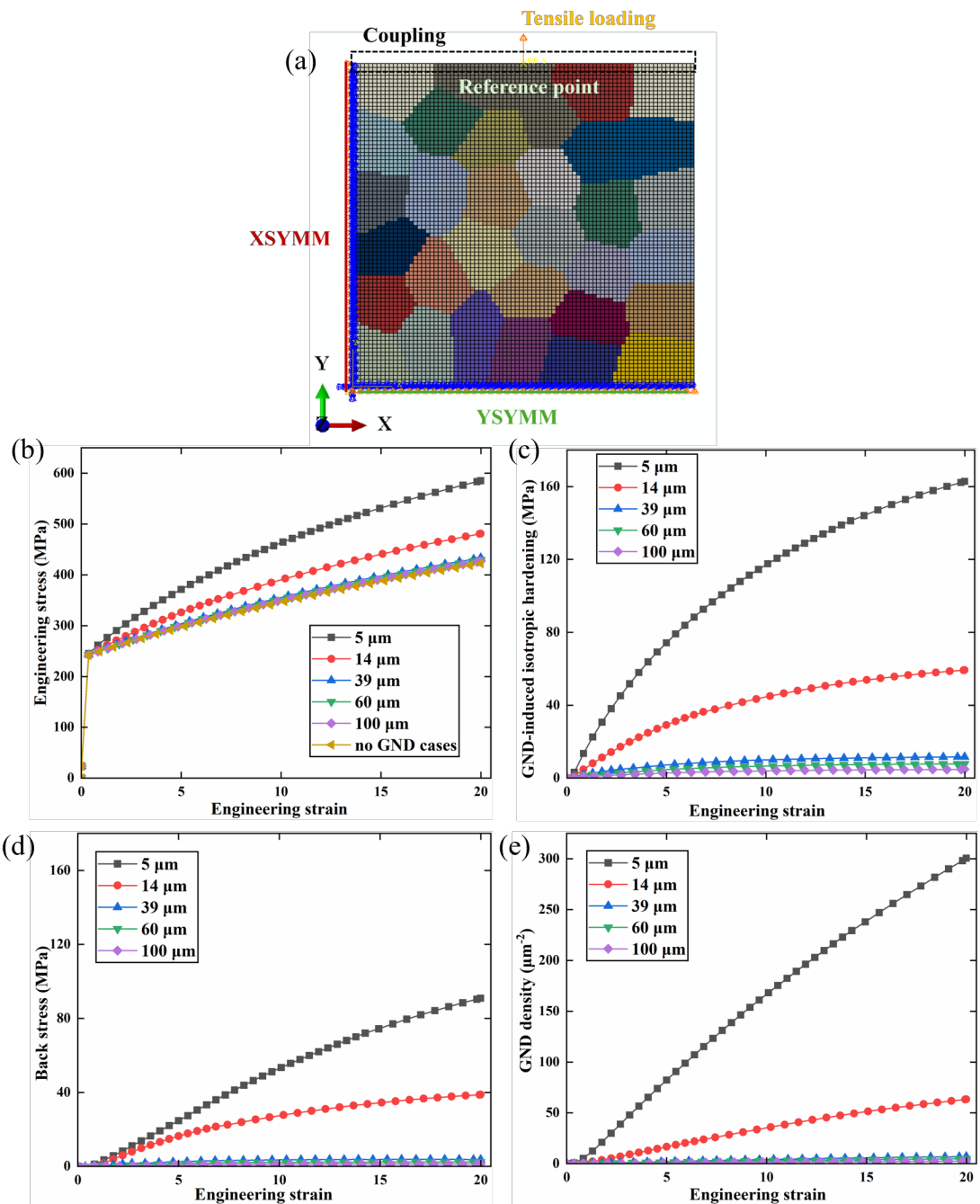


Figure 5.1: (a) RVE containing 32 randomly orientated grains generated using the Voronoi algorithm and boundary conditions adopted during the finite element simulations. Simulated (b) stress-strain curves and (c) GND densities for homogeneous polycrystals with grain sizes ranging from 5 μm to 100 μm . Results without GND hardening are also shown in (b). Contribution of (d) back stress hardening and (e) GND-induced isotropic hardening to the flow stress for homogeneous specimens with grain sizes in the range of 5 μm to 100 μm .

5.3.2 Validation of the constitutive model and parameter calibration

Figure 5.1(b) and (c) show the simulation results for the five homogeneous polycrystalline specimens with grains sizes ranging from 5 μm to 100 μm . Engineering stress-strain curves were computed from the force-displacement data obtained with the simulations. As shown in Figure 5.1(b), all samples exhibit increasing flow stress with increasing strain, indicating strain hardening. It can also be observed that the flow stress increases gradually with the decrease of the grain size. Thus, it can be said that the developed model can predict the grain size effect without introducing any grain size-dependent parameters in its set-up. When the grain size increases above 39 μm , the simulated stress-strain curves display minor variation, indicating that the grain size effect becomes rather weak. This is corroborated with the data given in Figure 5.1(c) as the GND density tends to stabilise and be minimal at this grain size and higher. The stress-strain curves simulated without considering GND hardening were also obtained for all five specimens. However, these curves overlapped since the grain orientation was identical for all five cases simulated. For this reason, only one curve labelled “no GND cases” is displayed in Figure 5.1(b) for comparison. From Figure 5.1(b), it is also noted that the grain size does not contribute to the elastic limit, but only significantly affects the flow stress during the plastic deformation stage. Besides, while all simulated specimens show strain hardening, the strain hardening rate increases as the grain size decreases. This coincides with experimental results obtained from FCC metals (Fang et al., 2011) and the simulation data reported in (Haouala et al., 2020; Zhang, Zhao, et al., 2023). The above results indicate that the developed model can be utilised to study grain size-dependent problems such as those for heterostructured materials.

5.3.3 Grain size effect

The back stress was calculated based on the simulated GND density following equation (5.12). To study their respective individual influence on the strain hardening behaviour, the GND-induced kinematic hardening i.e., the back stress, and the GND-induced isotropic hardening were separately assessed. Figures 5.1(d) and 1(e) show the contribution of the back stress and of the GND-induced isotropic hardening on the flow stress, respectively. Figure 5.1(d) indicates that the back stress emerges at the onset of plastic deformation. This agrees with the experimental findings from (Cheng et al., 2018) and the numerical findings reported in (Zhang, Zhao, et al., 2023) for gradient copper. The back stress keeps increasing during the whole deformation stage. This should result from the fact that physically, back stress is due to the spatially heterogeneous distribution of GNDs. In the initial deformation stage, back stress is linked to the piling up of GNDs at grain boundaries (GBs). During subsequent deformation, dislocation structures, such as cells and walls, also lead to heterogeneous distribution of dislocations, which further enhances back stress. As seen in Fig. 1(d), in the simulated specimens with larger grain sizes, back stress hardly contributes to the flow stress, while it becomes more and more pronounced with decreasing grain size. This conclusion agrees with experimental results where metals with smaller grain sizes showed a stronger Bauschinger effect (Zhang, Zhao, et al., 2023).

From Figure 5.1(e), it can be seen that the GND-induced isotropic hardening increases with the strain. This agrees with the experimental results from (S. Zhang et al., 2020) and the numerical predictions of (Li & Soh, 2012; Zhang, Zhao, et al., 2023). It is also observed that GND-induced isotropic hardening is higher than the GND-induced kinematic hardening under the same applied strain for all grain sizes considered. Having said that, the plots shown in Figure 5.1(d) and (e) suggest that when the grain size is larger than 39 μm , both GND-related effects can be neglected. Overall, based on these results, it can be inferred that the smaller the grain size, the stronger the GND-induced isotropic hardening and back stress. Besides, both GND-induced isotropic hardening and

back stress emerge in a significant manner in the initial deformation stage for smaller grain size specimens and increase gradually afterwards.

To further understand the effect of GNDs on the deformation behaviour of the simulated polycrystals, Figure 5.2(a) exhibits the evolution of the GND density across the modelled specimen, as well as the von Mises stress and ε_y for polycrystals with grain size of 5 μm , 14 μm and 100 μm . The GND density depicted here was calculated as:

$$\rho_{GND} = \sum_{\alpha=1}^{12} (|\rho_e^\alpha| + |\rho_s^\alpha|) \quad (5.16)$$

The above is a summation of absolute value of 12 edge dislocations, $\rho_{\Delta e}^\alpha$, and 6 screw dislocations, $\rho_{\Delta s}^\alpha$, on 12 slip systems. The reader should note that the model developed here is currently limited to uniaxial tensile loading as unloading or reverse loading could cause the change in dislocations. Future work should incorporate signed dislocations to extend the applicability of the model to more complex loading conditions.

From Figure 5.2(a), it is observed that the smaller the grain size, the more distributed the GND density is (Wulfinghoff & Böhlke, 2015). Moreover, the GNDs tend to accumulate near the GBs and especially at the triple junctions (Doan et al., 2023). With the increase of grain size, the dislocation density decreases, and the magnitude of the difference in density between the GB regions and the grain interiors become smaller and smaller, indicating that the deformation in specimens with larger grain sizes is more homogeneous as evidenced by the von Mises stress distribution shown in Figure 5.2(b). The strain along the tensile direction is displayed in Figure 5.2(c). The deformation becomes more inhomogeneous with the appearance of dense SBs when the grain size decrease to 5 μm . The experimental strain distribution along the tensile loading direction on copper with a grain size of 4.8 μm obtained in (C. X. Huang et al., 2018) is also displayed in Figure 5.2(d) for comparison. A good alignment is observed between the simulated results obtained here and those

of (C. X. Huang et al., 2018) due to the grain size and FCC crystalline structure similarities.

In summary, based on the results presented in this section for homogeneous-grained specimens, it can be said that that the simulations are reasonably consistent with experimentally observed mechanical responses reported in the literature. Thus, the developed framework was further employed to investigate micromechanical mechanisms for heterostructured materials as these can be challenging to study experimentally. In next section, the local stress and strain distributions as well as the overall mechanical response are investigated in the case of the HEA heterostructured material from (Fu, Huang, et al., 2022).

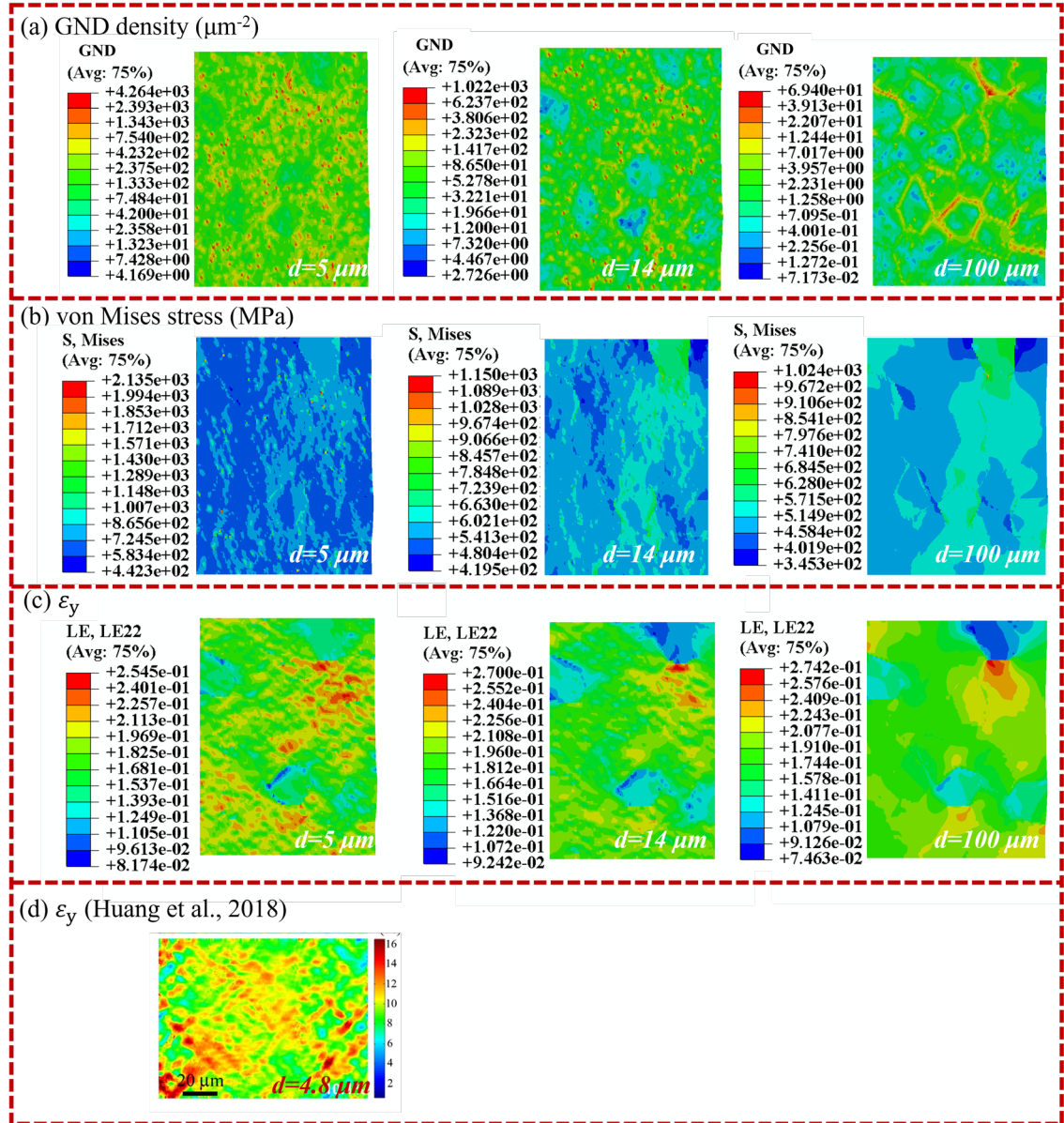


Figure 5.2: (a) Distribution of (a) the total GND density, (b) von Mises stress and (c) ε_y in the homogeneous grained HEA with grain size of 5 μm , 14 μm and 100 μm at a strain of 20%, (d) example of experimental ε_y distribution on copper with a grain size of 4.8 μm obtained in (C. X. Huang et al., 2018) using Digital Image Correlation. ε_y represents the strain components in the loading direction. These figures highlight a marked increase in GND density, von Mises stress and ε_y with a reduction in grain size.

5.4 Uniaxial tensile response of a bi-layered HEA specimen

After the successful validation of the developed framework, in this section, the tensile deformation of a bi-layered HEA is simulated to investigate its strengthening mechanisms during deformation. Firstly, grain sizes of 14 μm , 39 μm and 60 μm were adopted to adhere to the grain size after LSP, recrystallization annealing (RA) and casting treatment, respectively, based on the work of Fu et al. (Fu, Huang, et al., 2022). Then, the strengthening mechanisms including SB formation and GND hardening of bi-layered HEA were investigated via the developed model.

5.4.1 Finite element model

The geometric model was divided into two regions, namely 1 and 2, as shown in Figure 5.3(a), with each one characterised by a specific grain size according to the experimental data from Fu et al. (Fu, Huang, et al., 2022). In particular, region 1 had a grain size of 14 μm , while it was 46 μm for region 2. The interface between both regions was assumed to be perfectly bonded. Plane strain element was adopted which could accurately capture the mechanical behaviour of the material while reducing computational cost. Following the LSP operations conducted in (Fu, Huang, et al., 2022) by Fu and co-workers, the thickness of the surface and core layers was 300 μm and 700 μm , respectively. Accordingly, the thickness of the two regions in the model were set as 90 μm and 210 μm to keep the same ratio while reducing the computational burden. The overall size of the model was 300 μm along the x-axis and 600 μm along the y-axis. Uniaxial tension was applied in the y-direction at a strain rate of $7.14 \times 10^{-4}/\text{s}$ on the reference point shown in Figure 5.3(a). This reference point was also coupled with the top surface. The bottom surface was fixed on all degrees of freedom. Three paths of interest were selected as shown in Figure 5.3(a) for plotting and investigating a number of state variables. As displayed in this figure, "Path A"

traverses both regions in the middle of the specimen along its thickness. “Path B” corresponds to the interface between the two regions and “path C” cuts across the middle of region 1 in the direction of the y-axis, i.e. the loading direction.

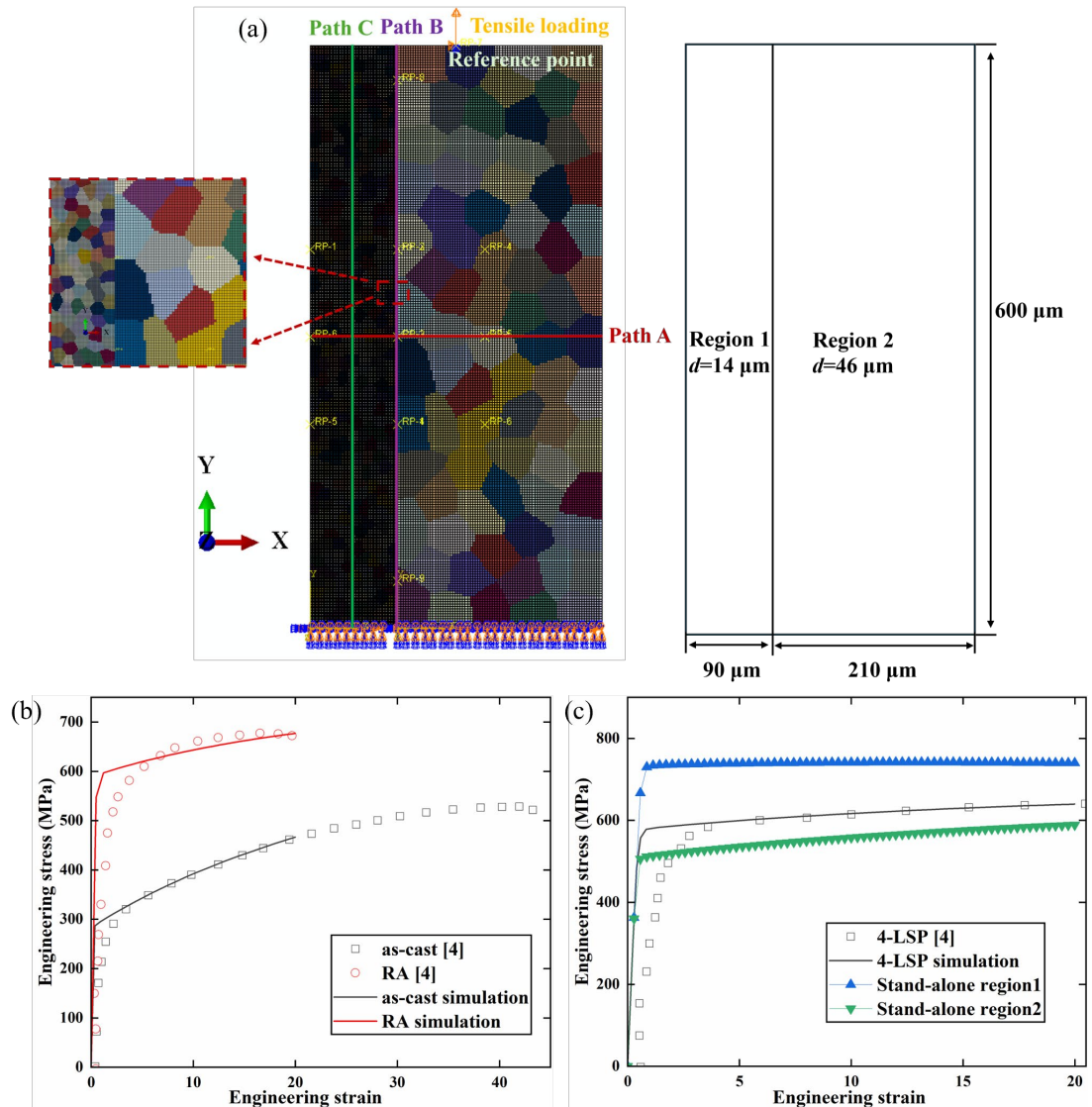


Figure 5.3: (a) Finite element model of the bi-layered specimen with different grain size, d , between both regions and adopted boundary conditions. Comparison of simulated and experimental engineering stress-strain curves for (b) as-cast and RA homogeneous HEA specimens; (c) bi-layered and stand-alone HEA regions 1 and 2. 4-LSP indicates four repetitions of the laser shock peening operation.

5.4.2 Uniaxial tensile response

- **Stress-strain curves**

Figure 5.3(b) and (c) display the simulated stress-strain curves associated with different states of the HEA sample processed by Fu et al. (Fu, Huang, et al., 2022). More specifically, Figure 5.3(b) displays results for cases where the specimen had a homogeneous grain size distribution, i.e. not in a bi-layered state. This corresponds to “as-cast” and the “recrystallization annealed” (RA) scenarios for which the grain size was 60 μm and 39 μm , respectively. The experimental tensile data obtained in (Fu, Huang, et al., 2022) for these two cases are also displayed in Figure 5.3(b) for comparison. Different from the previous section, where the dislocation density was intentionally set to 0.1/ μm^2 for all five models to isolate the effect of the grain size, the dislocation density in the as-cast and the RA model were set to 15/ μm^2 and 600/ μm^2 based on the report of (Fu, Huang, et al., 2022), while the remaining parameters remained unchanged. Overall, the simulation results displayed in Figure 5.3(b) align with experimental data reasonably well for both cases. Slight deviations between the experimental and simulation results are observed mainly during the initial yielding stage. Thus, the reliability of the developed model is judged to be acceptable based on this comparison. In Figure 5.3(c), the simulated and experimental engineering stress-strain characteristics of the bi-layered HEA are also compared. In this case, the experimental data considered from (Fu, Huang, et al., 2022) are those following LSP. The simulated results for the stand-alone region 1 and for the standalone region 2 are also plotted for comparison. It can be seen from this figure that the simulated model with the finer grain size displays a higher flow stress and a flatter hardening curve, indicating limited strain hardening ability.

It should be noted that the values of the grain size considered here are fairly large, i.e. 14 μm and 46 μm for region 1 and 2, respectively. As reported in (Zhou, Li, et al., 2024) and (Zhang et al., 2021), a larger mechanical heterogeneity

is beneficial for optimising the strength-ductility synergy. For this reason, it is expected that both GND-induced isotropic hardening and back stress hardening should have more significant effects on the strain hardening for samples combining nano-scale grains in the surface layer and micro-scale grain in their core (Zhang, Zhao, et al., 2023).

- **Shear bands formation**

In contrast with the homogenisation scheme used in (X. Lu et al., 2019; Zhang, Zhao, et al., 2023) for the CPFEM simulation of gradient structures, one of the advantages of the full-field model developed here is that it enables the investigation of deformation morphology at grain level. This means that the distribution and evolution of local strain bands, also known as SBs (Wang, Huang, Li, Guo, et al., 2020; Y. F. Wang, C. X. Huang, et al., 2019) can be simulated. Figure 5.4(a) and (b) show the local strain, ε_x , along the thickness and ε_y , in the tensile direction, respectively. It can be observed from these two figures that dense SBs are distributed over the sample during tensile deformation, and especially in region 1. These SBs tend to be orientated at about 50° with respect to the tensile axis (see Figure 5.4(b)), which agrees with in-situ DIC analyses in (Fu et al., 2023; M. Huang et al., 2018; Y. F. Wang, C. X. Huang, et al., 2019; Yuan et al., 2019). Such dispersed SBs undertake large strain but none of them carries excessively high strain concentration, thus resulting in locally inhomogeneous, but globally uniform, strain distribution (Fu et al., 2023). It is also observed from Figure 5.4 that the SBs density decreases significantly in region 2. This implies that the low strain hardening capability of the harder layer, i.e., region 1, provides favourable conditions for the formation of SBs, as also evidenced in (Fu et al., 2023).

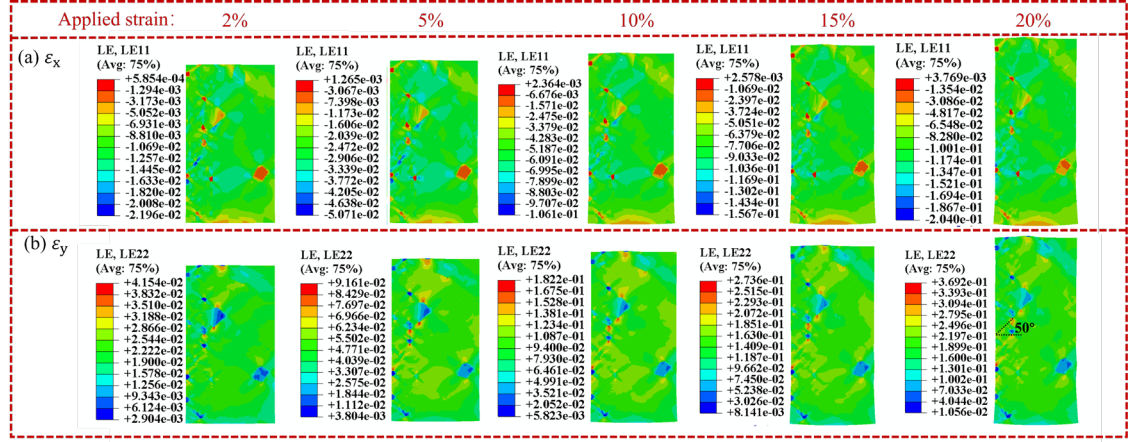


Figure 5.4: Distributions of (a) ε_x and (b) ε_y in the simulated bi-layered HEA at strains of 2%, 5%, 10%, 15% and 20%.

To further quantify the evolution of SBs under different tensile strains, the size and distribution of SBs along “Path A” and “Path C” (defined earlier with Figure 5.3(a)) were statistically analysed as shown in Figures. 5. The larger peaks observed in these figures correspond to the location of SBs. From Figures. 5(a) and 5(c), which respectively display values for ε_x and ε_y along “Path C” (i.e., within region 1 and aligned with the tensile direction), it is seen that local strain intensities i.e., whether within SBs and in the surrounding matrix, increase with the applied strain. With further increase in applied strain, as displayed in Figure. 5(c) and Figure 5.9(d), the increased amplitude in strain variation indicates that dense SB clusters are introduced by the extension and interaction of incipient SBs, which prevent the premature failure of heterostructured HEAs. While the width of SBs in the heterostructured HEA generally remains constant, their intensity increases linearly with the applied tensile strain as confirmed in Figure 5.5(d). This result also aligns with the experimental finding from Fu and co-workers (Fu, Huang, et al., 2022).

Figures. 5.5(b) and 5.5(d) show the distribution of SBs along “Path A”, which crosses both regions through the middle of the specimen. During initial loading i.e., for a strain of 2%, the values for ε_x and ε_y in region 2 remain relatively constant along this path, while these fluctuate in region 1. This indicates that SB

nucleation originates in region 1, with the smaller grain size, and then propagate along the shear direction (see Figure 5.5(d)). With increasing applied tensile strain, SBs also form in region 2 but with a lower density and magnitude. The local strain along both directions in region 1 is more heterogeneous than that in region 2 during loading, indicating a higher density of SBs. Subsequently, such strain gradient leads to differing plastic deformation behaviour between region 1 and region 2 during tensile loading. Based on Figures 5.5 (b) and 5.5(d), it is noted that, while the respective magnitudes of ϵ_x and ϵ_y across both regions are generally comparable regardless of the applied strain, it is interesting to see that these strain values in region 2 tend to increase more steadily and smoothly. This suggests that the plastic deformation capacity in this softer region is higher than that in the harder region 1, which contains the smaller grains. In other words, plastic deformation is mainly driven by the core region 2. This result is aligned with the experimental findings of Fu and co-workers in (Fu, Huang, et al., 2022) and with the stress-strain results shown earlier with Figure 5.3(c), where the modelled bi-layered HEA displayed a work hardening behaviour closer to that of the stand-alone region 2.

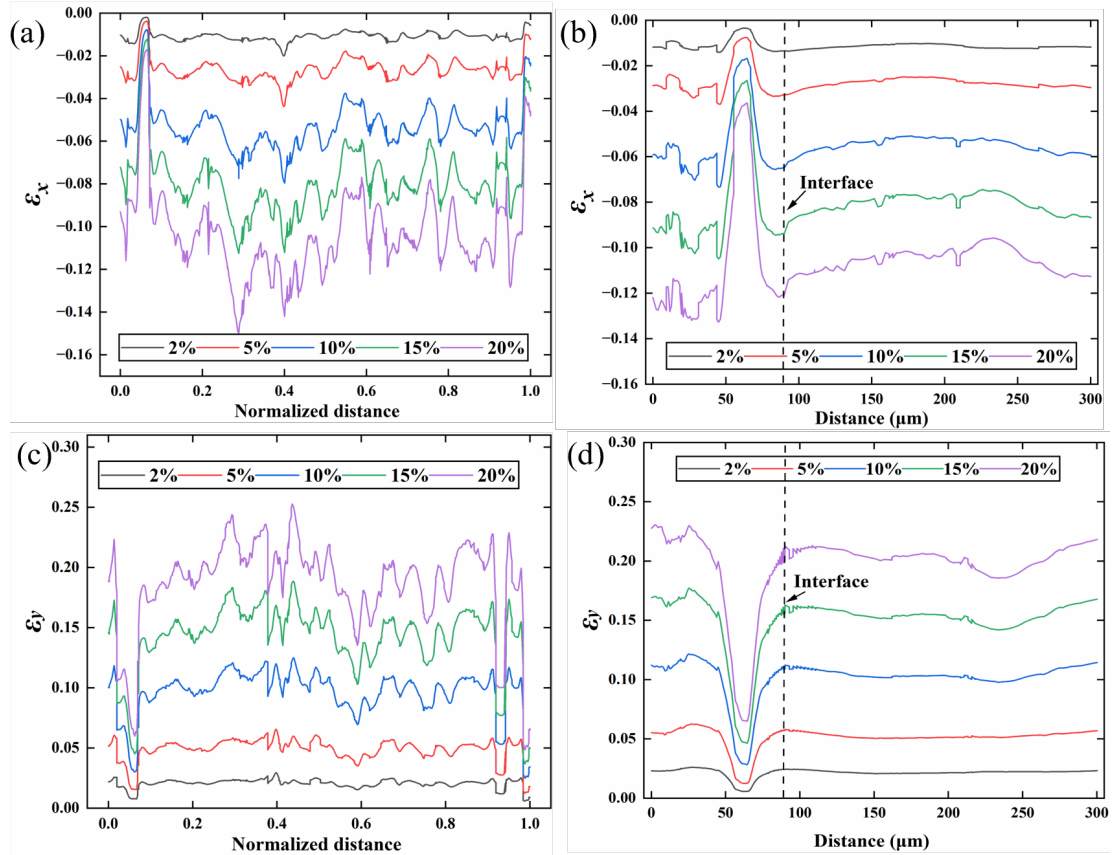


Figure 5.5: Distributions of local strain ϵ_x (thickness direction) on (a) “Path C” i.e., within region 1 along the tensile direction, and (b) “Path A” i.e., along the thickness of the specimen across both regions, for the simulated bi-layered HEA at different tensile strains. Distributions of local strain ϵ_y (loading direction) on (c) “Path C” i.e., within region 1 along the tensile direction, and (d) “Path A” i.e., along the thickness of the specimen across both regions, for the simulated bi-layered HEA at different tensile strains.

- **GND hardening**

In this section, the distributions of several pre-set internal state variables, namely GND density, von Mises stress and back stress, are analysed to understand grain-scale and sample-scale deformation features of the modelled bi-layered HEA. For heterostructured materials, in addition to GNDs pile-up near the grain boundaries, i.e., grain-scale GNDs, non-uniform deformation can arise due to the strain partitioning between the coarse-grained and the fine-

grained layers resulting in the formation of sample-level GNDs (Jamalian & Field, 2020; Li et al., 2017). Figure 5.6(a) provides the simulated GND density at a strain of 20% along “Path A”. The inset included in the figure also shows the distribution of GNDs over the entire bi-layered specimen at this strain rate. It is observed from this simulated data that the GND density is higher in region 1 and that dislocations accumulate preferentially at the grain boundaries. These findings also coincide with the experimental observation reported in (Hasan et al., 2019) where GND density decreased from small grains to large grains in a CoCrFeNiMn gradient grained HEA. The higher dislocations density observed here in region 1 increases significantly with the applied strain during plastic deformation as shown in Figure 5.6(c), which agrees with the experimental findings of (Fu, Huang, et al., 2022). From a qualitative viewpoint, Figure 5.6(c) also suggests that a very small amount of GNDs formed at the interface between both regions. To gain further insights into the formation of such sample-level GNDs, Figure 5.6(b) shows the simulated GND density at a strain of 20% at the interface between regions 1 and 2 i.e., along “Path B”. For comparison, the figure also includes the simulated GND density on the equivalent location on region 1 but when considered as a stand-alone region i.e., along its right edge when viewed from the top. Although slightly larger fluctuations of the GND density are observed in the bi-layered HEA compared to the stand-alone sample, it could be said that overall, the magnitude of GNDs at the interface for the bi-layered specimen is similar to that of the stand-alone model of region 1. This means that the formation of sample-level GNDs is not obvious for the bi-layered specimen modelled here. This is likely due to the fact that the difference in mechanical properties between both regions considered in this work is not significant as the difference in grain size between both is relatively small, i.e. a factor of 3.

Overall, the results given in Figures 5.6(a-c) demonstrate that, for the pair of grain size values considered in the modelled bi-layered HEA i.e., 14 μm and 46 μm , there is no obvious concentrations of GNDs at the interface between

regions 1 and 2. This observation is aligned with the results shown earlier with Figures 5.5(b) and 5.5(d), which plotted the simulated strain at the interface. For the specific bi-layered HEA material modelled here, numerous grain-scale GNDs accumulate around GBs, especially in region 1, to accommodate the strain gradient between adjacent grains. Given that only a small amount of sample-level GNDs accumulate along the interface, it can be said that HDI strengthening originates largely from the accumulation of grain-scale GNDs in the case modelled here, rather than from sample-scale GNDs. This aligns with the experimental findings in (Zhou, Wang, et al., 2024) where the authors found that a only a small number of sample-scale GNDs accumulated around the interface between the coarse- and fine-grained regions of copper-brass laminates. Instead, the authors found that a large number of grain-scale GNDs accumulated around GBs to accommodate the strain gradient resulting from the heterogeneous deformation between neighbouring grains. The average grain size of the specimens considered by these authors in (Zhou, Wang, et al., 2024) was $\sim 5.8 \mu\text{m}$ for the copper layers and $\sim 1.1 \mu\text{m}$ for the brass layers. Thus, both grain sizes were on the microscale and there was a factor ~ 6 between them, which is somewhat comparable with the configuration of the specimen modelled here. It should be noted however, that the copper-brass laminates fabricated in (Zhou, Wang, et al., 2024) exhibited a $\sim 7 \mu\text{m}$ gradient interface between the coarse- and fine-grained regions. This interface was composed of a gradient distribution of Zn and Cu elements. Such gradient interface, referred to as a “gradient transition layer” in (Zhou, Wang, et al., 2024) is not considered here. Indeed the interface between the HEA layers was modelled as a sharp transition in this work based on the experimental report in Fu et al. (Fu, Huang, et al., 2022).

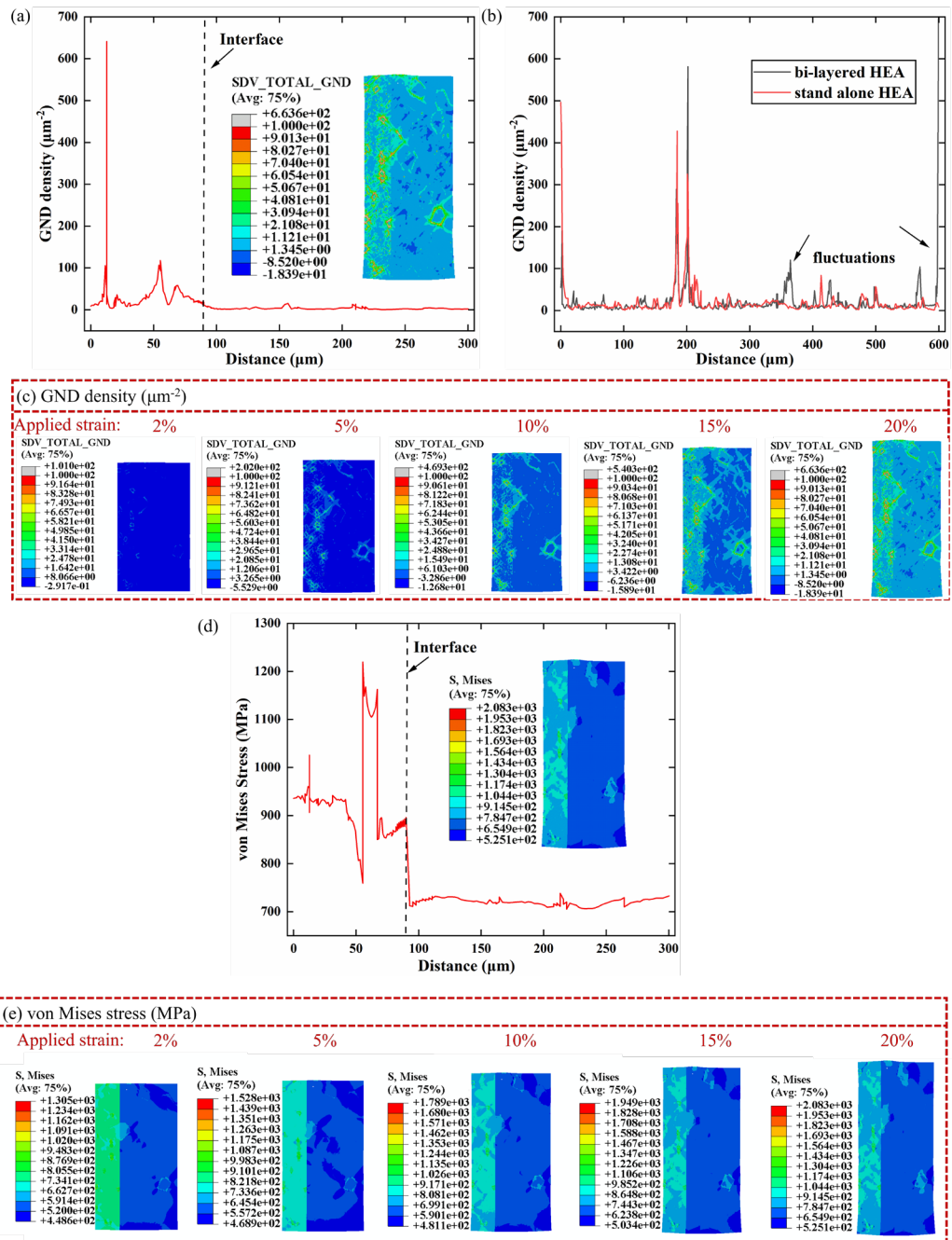


Figure 5.6: GND density in the modelled bi-layered HEA at a strain of 20% along (a) “Path A”, and (b) “Path B”. (c) Distributions of GNDs at strains of 2%, 5%, 10%, 15% and 20%. Simulated (d) von Mises stress along “Path A” for a strain of 20% and (e) distributions of von Mises stress at strains of 2%, 5%, 10%, 15% and 20% for the entire bi-layered HEA modelled.

Figure 5.6(d), which presents the distribution of the von Mises stress along

“Path A” at a strain of 20%, shows that the von Mises stress in region 1 is the highest. That is to say, region 1 carries more stress and region 2 experiences more plastic deformation. This agrees with the FEM simulations presented by Wang and co-workers in the case of polycrystalline metals with gradient grain sizes (Y. Wang et al., 2017). Furthermore, the stress along region 2 appears more homogeneous than that in region 1, where GNDs play a significant hardening role and no significant difference in stress values is noted between the grain interiors and the GBs in region 2.

Figure 5.7 shows the distribution of back stress on the 12 slip systems at a strain of 20%. Similar to the simulation data reported above for the von Mises stress and the GND density, qualitatively it is observed that the back stress increases with decreasing grain size. This is aligned with the stress-strain curves shown in Figure 5.3(c) and with experimental measurements reported by (Gao et al., 2022; Mahato et al., 2016), as well as with numerical predictions from (Zhang, Zhao, et al., 2023). This result also indicates that back stress originating from the smaller grains should be a non-negligible factor when considering back stress hardening in heterostructured materials.

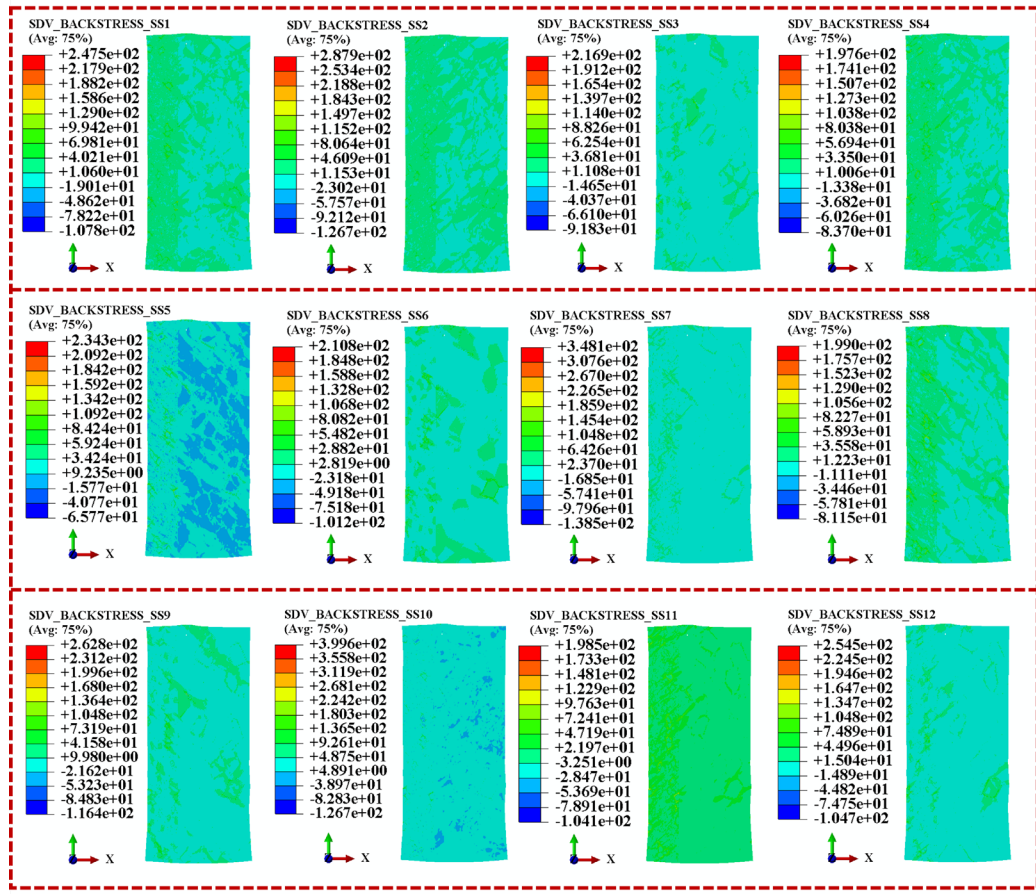


Figure 5.7: Simulated distributions of back stress on the 12 slip systems in the modelled bi-layered HEA at a strain of 20%.

- **Damage initiation**

As presented earlier, the JC damage initiation criterion was also incorporated into the CPFEM framework. From Figure 5.8(a), which presents the simulated damage criterion values for the whole bi-layered HEA specimen for an applied strain of 20%, it can be seen that region 1 is relatively more prone to damage. This was reported at triple junctions formed by grains in (Charpagne et al., 2021; Zhang et al., 2010). SBs tend to form in alloys with fine grains due to their work hardening capability, and eventually become crack initiation sites due to stress concentration (Marano et al., 2019; K. Wang et al., 2022). Moreover, adjacent SBs can eventually connect with each other with the increase of tensile strain, as seen in Figure 5.8(c) when the strain eventually reaches 20%.

It was reported that SBs are likely to transmit into neighbouring grains with low GB misorientations (Ahmadikia et al., 2021). MD simulations on a smaller grain size HEA also revealed that the rotation of grains can be triggered by grain boundary sliding and grain boundary migration as dominant mechanisms (Doan et al., 2023). High intra- and inter-granular crystal rotation are plasticity mechanisms common to samples, which exhibit high mechanical performance (Griesbach et al., 2024). Thus, the effect of grain orientation and rotation on the formation and propagation of SBs were also investigated in this work. In particular, the evolution of a typical SB spanning across 5 grains is analysed. This group of 5 grains is displayed in Figure 5.8(b) including the respective Euler angles. Specifically, grains ID 85, 290, 36 and 209 exhibit similar orientations while the grain ID 158 has higher misorientation angles.

Figures 5.8(c) and 5.8(d) present the SB and the JC damage factor evolution within this 5-grain region for strain values ranging from 0.2% until 20%. As seen in Figure 5.8(c), the SB initiates at a triple junction for grains with significant different orientations. With the increase in strain, the SB then propagates within grains that share similar crystal orientations, i.e. grains ID 85, 290, 36 and 209. This simulation result agrees with experimental studies reported in (Güler et al., 2018) where microcracks occurred in both GBs and intra-grains under tensile conditions for a FCC metal with a homogenous composition of micro- and nano-scale grains. From Figure 5.8 (d), it can be seen that there is a good alignment between the values of the JC damage criterion and the SB evolution. This suggests that the JC damage criterion could be employed as a suitable indicator to locate potential crack nucleation sites. For an applied strain of 20%, Figures 5.8 (e-g) shows that an appreciable amount of grain rotation took place for those grains traversed by the SB, in alignment with the experimental findings in (K. Wang et al., 2022). In contrast, grain rotation is less severe for the grain ID 158, which had a higher initial misorientation compared to the other four grains. This observation is also in line with the experimental findings of (Ahmadikia et al., 2021) where the authors reported that the orientation of

neighbouring grains affected the development of slip bands and their potential transmission. This is because the constraints placed on grains can be altered both by the grain size and the orientation-compatibility with neighbouring grains. Electron diffraction and imaging of the deformation sub-structures near SB interfaces reported in (Dève et al., 1988) also showed that an important part of the localization mechanism is non-uniform lattice re-orientations that cause a “geometrical softening” of the lattice. Thus, both the grain orientation distribution and the gradient distribution are deemed to be important structural features influencing the mechanical response (Griesbach et al., 2024). Moreover, the accumulated slip in this 5-grain region is also displayed in Figure 5.8(h) for an applied strain of 20%. It is evident that the accumulated slip in the grain traversed by the SB is higher than that in the grain not affected by the SB.

Grain reorientation plays a critical role in determining the anisotropic mechanical properties of materials, especially under high strains. As grains rotate and align along preferential directions, the material’s texture evolves, influencing its strength, ductility, and failure mechanisms. Incorporating grain reorientation into the analysis would allow for a more comprehensive understanding of how crystallographic texture development impacts strain localization, hardening behaviour, and damage accumulation. Such an approach would provide valuable insights into the microstructural evolution and its correlation with macroscopic mechanical response, particularly under extreme loading conditions.

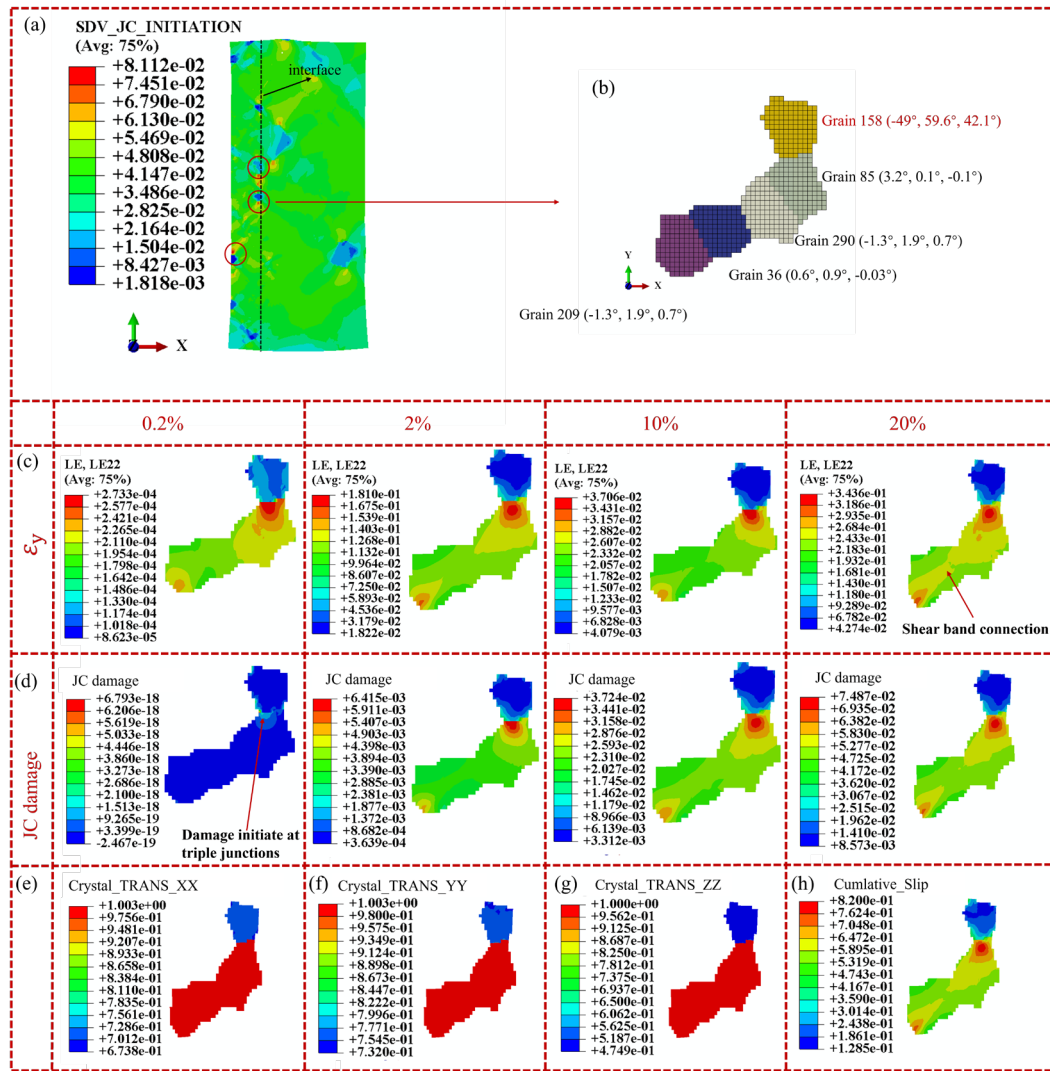


Figure 5.8: (a) Distribution of JC damage factor values for an applied strain of 20%; (b) a locally enlarged region composed of 5 grains with one of them displaying strong misalignment relative to the other four; evolution of (c) SBs and (d) damage within this region for strain values between 0.2 % and 20%; (e, f, g) crystal orientation within this region along the x, y and z direction, respectively, for an applied strain of 20%, and (h) accumulated slip, again for 20% strain.

5.5 Conclusions

This Chapter presented a novel non-local crystal plasticity model, which explicitly includes GNDs, back stress hardening and damage criterion.

Importantly, the model does not employ a homogenisation scheme, which means that it can be employed to investigate dislocation-mediated plasticity at grain-level for heterostructured materials. The model was implemented for a bi-layered HEA and its outcomes were validated against experimental data available from the literature. The model was able to confirm that the heterostructured HEA elicited heterogeneous deformation and consequent HDI strengthening during tension. Comparatively, low strain and high stress were observed in the region with smaller grains, while the coarser-grained region experienced lower stresses but more extensive plastic deformation. The more specific finding associated with this work are as follows:

1. The novel CPFEM framework developed here was able to reproduce and confirm a number of known experimental findings, namely that **a)** SBs and damage propagate among grains sharing similar orientation and **b)** significant rotation and slip take place in grains subjected to severe damage. Based on this, it is suggested that the properties of heterostructured materials could be further enhanced not only by controlling the grain size and dislocation density gradients, but also by controlling the initial grouping of grains and their respective orientations as well. Explicit modelling of orientation information of polycrystalline grains should be considered in future research. Indeed, a systematic study on the effect of grain orientation should pave the way towards a quantitative understanding of heterogeneous microstructures on the mechanical behaviour of a broader class of heterostructured materials.
2. Besides, for the bi-layered HEA modelled here, GNDs accumulated at grain boundaries, rather than at the hetero-interface. The absence of a significant jump in GND density across the interface is attributed to the relatively small difference in deformation between the fine-grained and coarse-grained regions. The deformation gradient is not substantial enough to cause a sharp discontinuity in GND density at the interface. Future work should investigate whether a threshold exists with respect to the size ratio between fine and coarse

grain regions for which GNDs accumulation at interfaces becomes more prominent than grain-scale GNDs.

3. It is suggested that the JC damage criterion could also be employed to characterise SBs evolution, which in turn could lead to the identification of potential crack nucleation sites.

It is worth noting that while this study focussed on a single phase bi-layered heterostructured HEA, the CPFEM framework developed here could also be applied to FCC/BCC alloys with different phases. It is also worth mentioning that the presented simulations were based on a 2D model with a focus on dislocation activities, and that this offers a computationally efficient approach compared to 3D cases with multiple mechanisms. Strong interfacial bonding is essential to prevent delamination, achieved through clean surfaces and techniques like diffusion bonding. Coarse-grained regions should use ductile materials, while fine-grained regions should employ high-strength alloys. These guidelines, supported by simulations, ensure optimal fabrication outcomes for achieving balanced mechanical properties.

Chapter 6 Numerical study on the strengthening and fracture characteristics of heterogeneous-structured TWIP/Maraging steel laminates using a non-local crystal plasticity and continuum damage mechanic model

6.1 Introduction

This Chapter investigated the strengthening mechanisms and fracture modes in HSLs through a full-field non-local CPFEM framework and incorporated progressive continuum damage mechanics (CDM) model for the crack initiation and propagation. The constitutive model was validated in homogenous TWIP steel and Maraging steel respectively before applied to the TWIP/Maraging steel laminates. It was observed that the non-local CPFEM-CDM model based on maximum slip accurately captured the typical brittle and ductile damage of stand-alone Maraging steel and TWIP steel. It was further found that the hard Maraging layer reside in the HSLs exhibited a fracture process of void nucleation, coalescence and propagation, displayed a brittle to ductile fracture transition which was in stark contrast to stand-alone Maraging layer where a typical brittle fracture was observed. These findings were in good agreement with recent experimental observations in terms of stress-strain responses, SBs evolution and fracture mode. The enhanced ductility of HSLs originated from the heterogeneous deformation-induced (HDI) stable SBs evolution during

tension. These findings may provide a potential strategy for the design and development of HSLs with excellent strength-ductility balance.

6.2 Constitutive relations and modelling framework

This section introduces a novel non-local CPFEM-CDM model, which integrates the effects of slip and dislocations on deformation behaviour using CPFEM, while CDM is also incorporated in the framework to consider fracture.

6.2.1 Overview

As mentioned earlier, the proposed framework was implemented in the context of studying the deformation and fracture characteristics of TWIP/Maraging steel laminates. Such type of HSL materials presents unique mechanisms and greatly depends on the mesoscale heterogeneous deformation (Yu et al., 2024). To accurately simulate the strengthening mechanisms and fracture of both steel phases, the developed non-local CPFEM-CDM model considered the inhomogeneous dual-phase microstructure, as well as the deformation behaviour and fracture mechanism of both constituent phases. Figure 6.1 details the proposed modelling framework. The numerical model was established based on actual grain morphologies obtained with scanning electron microscopy and EBSD by Yu et al. (Yu et al., 2018). To develop a realistic microstructure-based numerical framework for the investigation of fracture in HSLs, it is critical to accurately describe the deformation and damage behaviour of each constituent phase. Thus, the model was used initially to describe the elastic-plastic deformation behaviour and fracture of TWIP and Maraging steels separately. This enabled the calibration of the model parameters using the experimental stress-strain response and fracture characteristics of the individual homogeneous grained specimens from (Yu et al., 2018). The framework could subsequently be employed to simulate the deformation of TWIP/Maraging steel laminates. As a result, insights into the response of such HSL material subjected to tensile loading, including the intra-grain and inter-grain scale deformation, strengthening mechanisms and fracture characteristics,

could be gained. The detailed development and validation of the numerical framework are described next in sections 6.2 to 6.4.

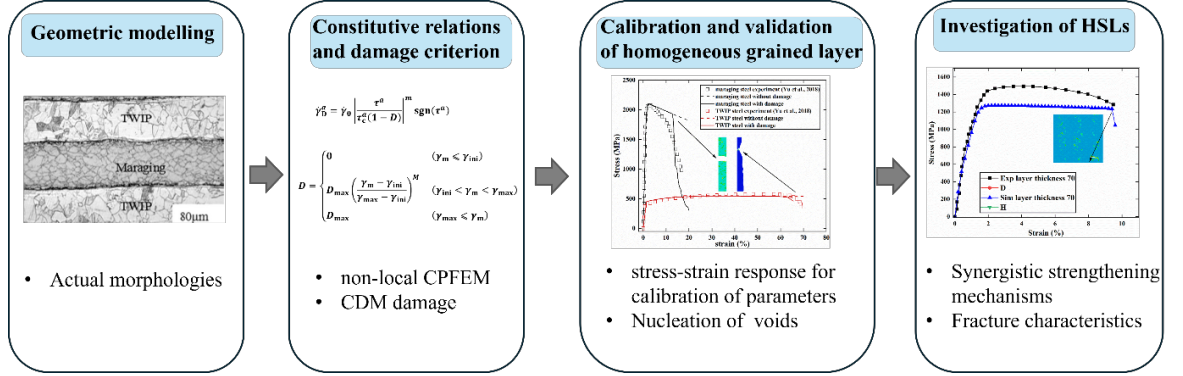


Figure 6.1: Overall framework of the developed non-local CPFEM-CDM model for the investigation of the fracture characteristics in TWIP/Maraging steel laminates.

6.2.2 CPFEM-CDM modelling of steel phases

- CPFEM slip law**

The shear strain rate $\dot{\gamma}^a$ generated by the dislocation motion of slip system a is expressed as (Ashby, 1970):

$$\dot{\gamma}^a = \dot{\gamma}_0 \left(\frac{|\tau^a|}{\tau_c^a} \right)^n \text{sgn}(\tau^a) \quad (6.1)$$

where $\dot{\gamma}_0$ is the reference shear rate, n is the power law exponent, τ^a is the shear stress acting on the slip system and τ_c^a is the critical resolved shear stress (CRSS), which describes the resistance to gliding dislocations. The CRSS can be further formulated as (McCabe et al., 2010):

$$\tau_c^a = (\tau_c^a)^0 + \Delta\tau_c^a + \tau_{for}^a \quad (6.2)$$

where $(\tau_c^a)^0$ is the initial CRSS and τ_{for}^a is the forest dislocation interaction stress.

- CPFEM hardening law**

The slip system hardening has the following evolution:

$$\Delta\tau_c^a = \sum_b \mathbf{H}_b^a \quad (6.3)$$

where b is the total number of slip systems and \mathbf{H}_b^a is the slip hardening moduli.

For latent hardening:

$$\mathbf{H}_b^a = q\Delta h^b (a \neq b) \quad (6.4)$$

where q is the latent hardening exponent. The self-hardening moduli Δh^b , which represents the hardening on a single slip system, evolves according to a power law formulation (Peirce et al., 1982):

$$\Delta h^b = h_0 \left(1 - \frac{\tau_c^b}{s_s}\right)^m |\dot{\gamma}^b| \Delta t \quad (6.5)$$

where h_0 is the hardening rate, s_s is the saturation slip strength and m is the hardening exponent.

- **GND calculation**

The GND density is calculated from Nye's dislocation density tensor Λ . The detailed calculation process of GND density and forest dislocation could be found in equation (5.8-5.10). The hardening caused by forest dislocations, τ_{for}^a , can be expressed as:

$$\tau_{for}^a = \zeta G^a b^a \sqrt{\rho_{for}^a} \quad (6.6)$$

where ζ is the dislocation interaction parameter, G^a is the shear modulus and b^a is the magnitude of the Burgers vector.

- **CDM fracture modelling**

Crack growth behaviour has seldom been studied in heterostructured materials (X. Li et al., 2019). At the same time, the microscale physical description of plastic strain is considered to be a suitable approach to explain the macroscopic mechanical response of materials (Jia et al., 2012). For example, the maximum shear strain damage model employed in a continuum damage framework was reported by Kim and Yoon to outperform stress-based counterparts in capturing the necking behaviour of aluminium alloy (Kim & Yoon, 2015). Besides, a more recent study reported that the maximum shear strain based criterion accurately captured the fatigue damage evolution in polycrystalline Al alloy (Zhongwen Zhang et al., 2024). Thus, to describe the sudden drop of load carrying capacity and the fracture of TWIP/Maraging steel laminates, a CDM

model based on maximum shear strain was adopted in the presented work. This model defines the damage as initiated and accumulated when maximum shear strain is greater than a given critical value. This model is expressed as follows:

$$D = \begin{cases} 0 & (\gamma_m \leq \gamma_{ini}) \\ D_{max} \left(\frac{\gamma_m - \gamma_{ini}}{\gamma_{max} - \gamma_{ini}} \right)^M & (\gamma_{ini} < \gamma_m < \gamma_{max}) \\ D_{max} & (\gamma_{max} \leq \gamma_m) \end{cases} \quad (6.7)$$

where γ_m is the maximum shear strain, i.e., the maximum shear strain among all slip systems, D is the damage factor and D_{max} is its maximum value. γ_{ini} is the maximum shear strain over which damage initiates and γ_{max} is the maximum shear strain at which the damage value reaches the maximum value D_{max} . When the maximum shear strain γ_m exceeds γ_{ini} , the damage begins to evolve in the slip system. When γ_m exceeds γ_{max} , the damage stops evolving and maintains its maximum value. The exponent M , known as the damage curve shape coefficient is set to 3.0 to improve convergence (Kim & Yoon, 2015). The damage parameters for both steel phases were determined based on the stress-strain relation and fracture characteristics obtained from tensile tests. The damage value was calculated for each integration point and applied to slip system-wise by solving the nonlinear equation (6.11). In this way, damage could be accumulated in an explicit manner in the CPFEM framework. To consider this progressive decrease of load carrying capacity in the developed model as damage accumulates, the resolved shear stress, i.e., τ_c^a in equation (6.1) was downscaled with the calculated damage as:

$$\dot{\gamma}_D^a = \dot{\gamma}_0 \left| \frac{|\tau^a|}{\tau_c^a(1-D)} \right|^n \text{sgn}(\tau^a) \quad (6.8)$$

It should be noted that the assessment of γ_{ini} can be approached by considering the weakest slip system and its orientation relative to the loading direction, as these factors critically influence the initial shear strain. A detailed crystallographic analysis should be performed to identify the slip systems with the lowest CRSS and their alignment

with the applied stress. This approach ensures a more accurate evaluation of γ_{ini} and its dependence on crystallographic orientation.

However, due to current experimental limitations, we have not yet been able to conduct the necessary investigations to validate this approach. Future work should prioritize experimental studies to directly measure γ_{ini} under controlled loading conditions, particularly focusing on materials with varying slip system strengths and orientations. Such experiments would provide critical insights into the role of crystallographic anisotropy and further refine the theoretical framework.

6.2.3 Model implementation for uniaxial tensile tests on TWIP/Maraging steel laminates

The numerical implementation of the proposed modelling framework was realised on the software platform ABAQUS/Standard via user-defined subroutines (UMAT) (Dunne et al., 2007; Hardie et al., 2023; Liang & Dunne, 2009). The deletion of an element was determined by assessing whether its damage variable, i.e. D in equation (6.11), had reached the corresponding critical value. To reveal the strengthening mechanisms and fracture characteristics of the modelled TWIP/Maraging steel laminates, detailed finite element simulations were conducted. More specifically, the finite element model employed in this work contained 6 layers, with each layer having a thickness of 70 μm and assigned either as TWIP or Maraging steel to form a complete HSL specimen as illustrated in Figure 6.2. The average grain size was set to 20 μm for the TWIP layer and 10 μm for the Maraging layer based on the experimental findings reported by Yu and coworkers (Yu et al., 2018; Yu et al., 2019; Yu et al., 2024). The microstructure information was generated with the open-source software Neper. A custom MATLAB script was compiled to convert the voxel files generated with Neper into input files required for the commercial software ABAQUS to conduct the CPFEM simulations. It was reported by Zhang et al. that a resolution of 32 elements for each grain should be sufficiently high for the simulation of polycrystals (Zhang, Zhao, et al., 2023).

For crystal plasticity damage models featuring grain size about 200 μm , 100 μm , and 50 μm in the x , y , and z directions, respectively, an element size of 50 μm was selected by (Kim & Yoon, 2015). The mesh convergence study shown in Appendix A demonstrates that a mesh resolution of around 200 elements for each grain was adequate for the TWIP/Maraging steel laminate studied here. A strain-controlled load at a rate of $1 \times 10^{-3} \text{ s}^{-1}$ was applied on the top side along the y -axis direction. The detailed boundary conditions are shown in Figure 6.2.

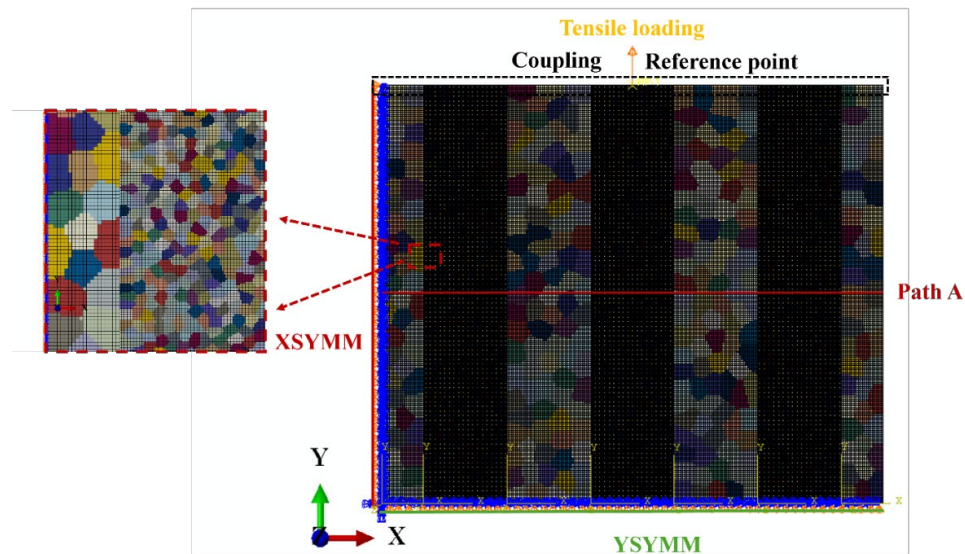


Figure 6.2: Finite element model of the TWIP/Maraging steel laminate and adopted boundary conditions.

6.2.4 Determination of model parameters and validation with standalone steel specimens

Two categories of parameters are required in the developed modelling framework, namely 1) constitutive model i.e., CPFEM, parameters, and 2) CDM parameters. The CPFEM parameters for both TWIP and Maraging layers were determined based on literature data (Hosford, 1993; Woo et al., 2012). These are listed in Table 6.1. However, the CDM parameters required calibration by matching the simulated stress-strain responses and fracture characteristics of individual homogenous TWIP and Maraging steel models to experimental data from (Yu et al., 2018). Following this calibration exercise, the CDM parameters

could be obtained, as listed in Table 6.2.

Table 6.1: Parameters of the CPFEM model for TWIP and Maraging steel

Parameter	Notation	Value for TWIP	Value for Maraging	Parameter	Notation	Value for TWIP	Value for Maraging
Elastic properties	C11	169 GPa	231.4 GPa	Hardening rate	h_0	220 MPa	950 MPa
	C12	82 GPa	134.7 GPa	Saturation slip strength	s_s	550 MPa	1000 MPa
	C44	96 GPa	116.4 GPa	Hardening exponent	m	1	4
Power law exponent	n	20	10	Latent hardening exponent	q	1	1
Reference slip rate	$\dot{\gamma}_0$	10^{-3} s^{-1}	10^{-3} s^{-1}	Geometric factor	ζ	0.25	0.25
Initial CRSS	$(\tau_c^a)^0$	220 MPa	1100 MPa	Burgers vector	b^a	0.256 nm	0.248 nm

Table 6.2: Parameters of the CDM model for TWIP and Maraging steel.

Damage parameter	Notation	Value for TWIP	Value for Maraging
Shear strain when damage initiates	γ_{ini}	0.57	0.05
Shear strain when the damage reaches the maximum value	γ_{max}	0.62	0.09
Maximum damage factor	D_{max}	0.8	0.2
Damage exponent	M	3	1

Using the calibrated CDM parameters, Figure 6.3 shows the simulated stress-strain curves and deformation characteristic of individual homogenous grained TWIP and Maraging steel specimens against corresponding experimental data

from (Yu et al., 2018). These simulated results for individual layers are presented and discussed first to assess the suitability of the developed non-local CPFEM-CDM model prior to using it to study the strain hardening and fracture behaviour of TWIP/Maraging steel HSL. Although the outcome reported here for individual layers employ the calibrated CDM parameters, it is still of value to observe whether the model can output expected deformation behaviour for each steel material when considered as a standalone specimen. In this context, Figure 6.3, which also includes simulated specimen geometries post-fracture, shows that the model was able to output both the brittle fracture of Maraging steel and the ductile damage of TWIP steel based on the adopted fracture criterion of maximum shear strain. In particular, the simulations captured the expected three stages of deformation, namely 1) initial elastic deformation followed by 2) yielding and eventually the transition from yielding to 3) damage-induced softening. A comparison was also made when employing the CPFEM framework but without considering CDM as also reported in Figure 6.3. In this case, it is interesting to note that the sudden drop of load carrying capacity for both materials with increased plastic strain could not be predicted appropriately.

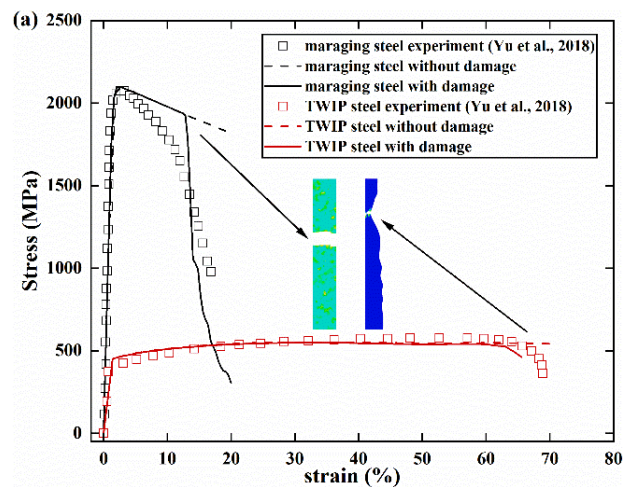


Figure 6.3: Comparison of the obtained numerical stress-strain responses against corresponding experimental data from (Yu et al., 2024) for individual homogeneous grained TWIP and Maraging steels.

Figure 6.4 provides additional data for the simulated standalone specimens, particularly with respect to their deformed geometry and experienced von Mises stress as a function of the strain until fracture. For the softer TWIP steel specimen, significant plastic deformation i.e., multiple necking, could be simulated before fracture as seen in Figure 6.4(a). This phenomenon correlates well with the experimental findings in (Yu et al., 2024). As should be expected, the simulated TWIP steel displayed good ductility and underwent significant necking before the point of failure, which occurred at a large strain of 65.7%. In contrast, typical brittle fracture was observed in the simulated deformation of Maraging steel as reported with Figure 6.4(b). In this case, little to no plastic deformation was observed before fracture, which occurred at a much lower strain of 11.4%. Based on the data plotted earlier in Figure 6.3, it was determined that yield took place at a strain of 11.2% for the Maraging steel. Thus, catastrophic fracture occurred rapidly for this simulated specimen i.e., only with 0.2% additional strain post-yield. Its fractured surface was also correctly simulated to be perpendicular to the applied stress direction. Overall, the data shown in Figure 6.4 can also be used to note that stress concentration is simulated to occur at multiple locations near GBs for both standalone steel models. This is caused by orientation mismatch between neighbouring grains.

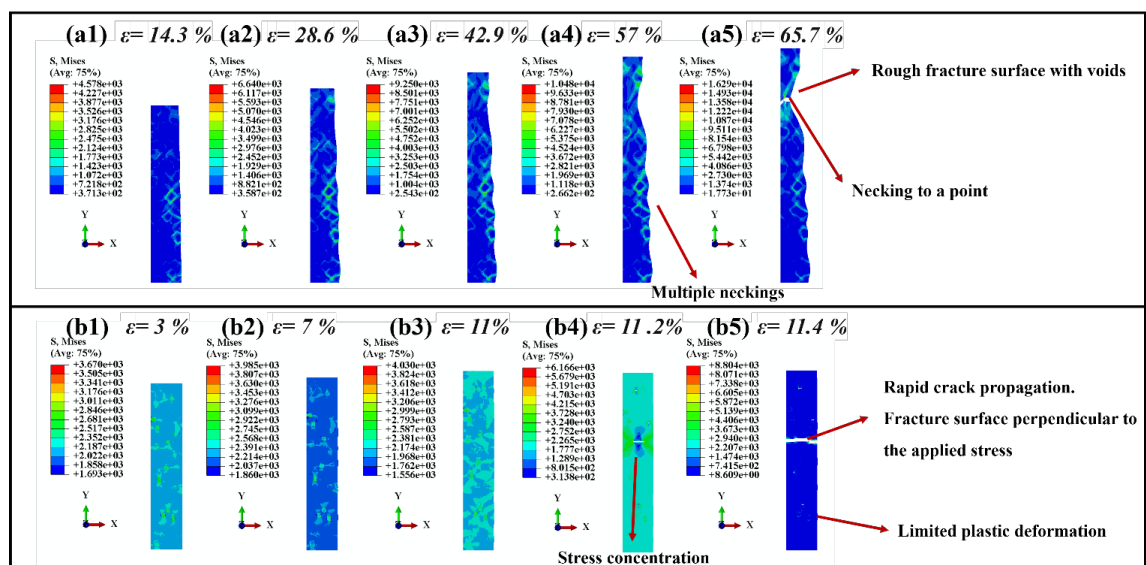


Figure 6.4: Simulated deformation and von Mises stress for (a) TWIP steel and (b) Maraging steel as a function of the strain until fracture.

Finally, Figure 6.5 displays the evolution of the simulated SBs for both standalone TWIP and Maraging steel models. As displayed in Figure 6.5(a), at 64% strain a significant macroscopic SB had formed in the TWIP steel at an angle of about 50° with respect to the thickness of the specimen. This figure also shows that when the strain increased to 65%, this SB intersected with a void in the necking region. This void nucleated within the SB and subsequently elongated along the shear axis. Within a short increase of the strain value i.e., at 65.7%, the specimen fractured revealing a surface formed of jagged cavities. In contrast, the magnitude of the simulated SBs was not significant for the Maraging steel, as displayed in Figure 6.5(b), due its limited strain hardening ability. For the more ductile TWIP steel material, the SB that displayed the largest magnitude coincided with the location of the crack initiation site (see Figure 6.5(a)). This aligns with the experimental findings reported by (Noell et al., 2018) for Cu samples. However, for the more brittle Maraging steel, it is interesting to note that the crack did not initiate at the site where the SB magnitude was the maximum. This implies that solely analysing SB quantitatively could not be used as the only indicator of crack initiation in this case.

In summary, the results provided in this section indicate that the developed non-local CPFEM-CDM model can suitably predict the deformation and fracture behaviour of the individual homogenous TWIP and Maraging steel specimens. Thus, the model can be further used to explore the strengthening mechanisms and the fracture behaviour these materials when arranged as in TWIP/Maraging steel HSL configuration. This is the focus of the next section.

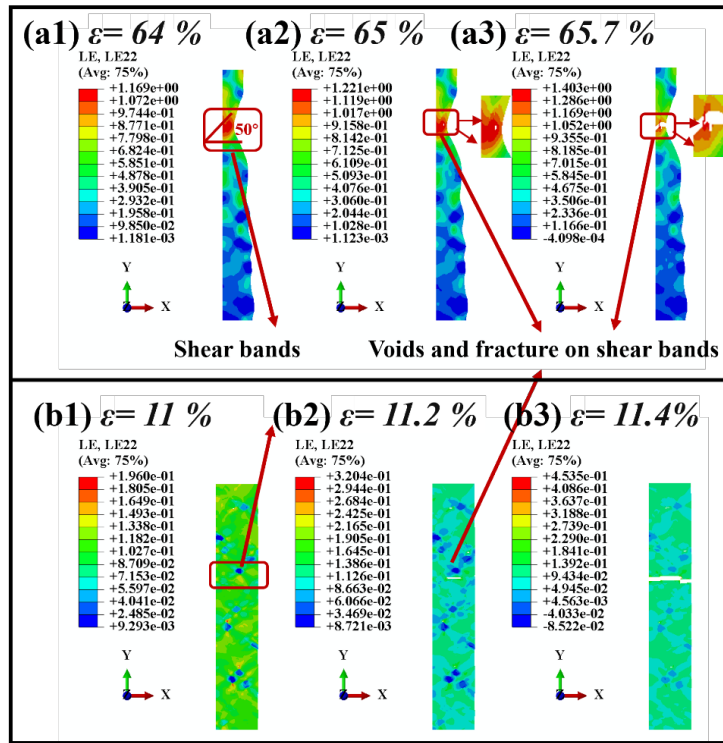


Figure 6.5: Simulated fracture process and evolution of SB for (a) TWIP steel and (b) Maraging steel.

6.3 Results and discussion for the simulated HSL specimen

In this section, the uniaxial tensile response of the TWIP/Maraging steel laminate is simulated until fracture to investigate mechanisms at play during the deformation of this type of HSL. The stress-strain response as well as the stress distribution and the evolution of the GND density are analysed first. Next, the behaviour of SBs is investigated to study their influence on the fracture of the modelled HSL.

6.3.1 Stress-strain response

Figure 6.6, which displays the simulated stress-strain curve, shows that the modelled HSL material exhibits a yield strength of 1246 MPa, an ultimate tensile strength of 1276 MPa and a uniform elongation of 9.4%. Based on the data

reported earlier with Figure 6.3, it was found that the standalone Maraging layer had a simulated yield strength of 2029 MPa, an ultimate tensile strength of 2097 MPa and a uniform elongation of 2.2%. The better ductility of the Maraging steel phase within a HSL configuration is a result of the addition of the softer TWIP layers and the strengthening effect induced by heterogeneous deformation. Compared to the standalone TWIP steel, both the yield strength and the ultimate tensile strength are increased when incorporated in the HSL. As seen in Figure 6.7, the simulated stress-strain curve correlates well with experimental data during the elastic deformation stage as well as for the two discrete points which are characteristic of the onset of plastic deformation and of fracture strain, respectively. However, a discrepancy is noted whereas the experimental HSL sample exhibits strain hardening, while the simulated specimen shows a post-yield behaviour almost perfectly plastic. Although the model is capable of simulating strain hardening, as evidenced earlier in Figure 6.3 for the standalone TWIP steel material, this post-yield observation for the modelled HSL specimen suggests that mechanisms behind further strengthening phenomenon were not captured in the current framework. It is hypothesised that such additional factors may be associated with the fabrication process employed in (Yu et al., 2024) for producing the experimental laminate. More specifically, the hot-rolling necessary for manufacturing the HSL in (Yu et al., 2024) may have introduced grain refinement and phase transitions. Besides, the interface in the numerical framework developed here was simply modelled as perfectly bonded. However, it may be reasonable to assume that the presence of abundant interfaces could induce stress concentration and impede dislocation movement, thus increasing the material strength of the experimental HSL specimens (Gao et al., 2024). In addition, Gao and co-workers noted that existing defects in homogeneous layers might also be reduced during the bonding process when fabricating HSLs, thus resulting in improved material properties (Gao et al., 2024). In spite of this discrepancy in the post-yield stage between the experimental results and the data simulated here, it can

be said that the developed non-local CPFEM-CDM model predicted the evolution of the stress-strain relation for the TWIP/Maraging HSL specimen reasonably well, including the strain at fracture.

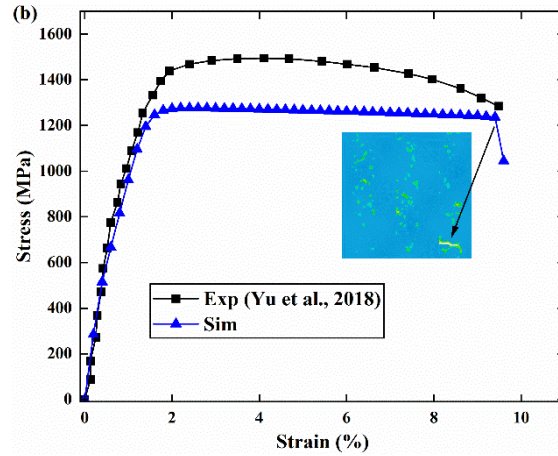


Figure 6.6: Simulated stress-strain curve compared against the experimental data from (Yu et al., 2024) for the multilayer TWIP/Maraging steel HS. The inset figure shows the CDM damage factors of laminates at fracture.

6.3.2 Stress partition and GND distribution

Figures 6.7(a) and 7(b) report the simulated distribution of the von Mises stress for both the entire HSL specimen and along “Path A”, respectively, for a strain of 9.4%. This corresponds to the strain value immediately before fracture. Stress partitioning behaviour has been experimentally observed in previous studies of HSLs and is caused by the non-synchronous deformation between different layers. The model output displayed in Figures 6.7(a) and 7(b) show that stress partitioning was successfully simulated as the stress in the Maraging steel layers is significantly higher than that in the TWIP steel layers. In addition, the inset generated from Figure 6.7(a) illustrates that stress-transfer from the Maraging layer to an adjacent TWIP layer can take place at the interface, which relieves strain localisation. In Figure 6.7(a), stress concentration is observed at numerous locations due to orientation mismatch near grain boundaries. Such stress concentration and stress transfer in HSLs are believed to facilitate the activation of non-basal slip face and consequently results in an enhancement of

strength (H. Zhang et al., 2024). Figures 6.7(c) and 7(d) display the simulated GND density distribution for the entire HSL specimen as well as along “Path A”, respectively, and again for the strain value immediately before fracture i.e., 9.4%. Similar to the distribution of the von Mises stress, the GND density is higher in the Maraging steel layers compared to that in the TWIP steel layers. This result, and the further observation that dislocations accumulate preferentially at the GBs, aligns with the experimental report in (Zhang, Zhao, et al., 2023). Based on the outcome shown in Figure 6.7(d), it is also suggested that the GND density contribution to strengthening is higher in Maraging steel layers. It is also expected that the incompatible deformation between the different microstructure configurations across the interfaces should lead to the generation and accumulation of GNDs. This also leads in extra work hardening and HDI strengthening (Han et al., 2023). However, this behaviour is not detected in the data shown in Figure 6.7(c). This could be due to the fact that the difference in mechanical properties between the TWIP and Maraging steels is not substantial enough.

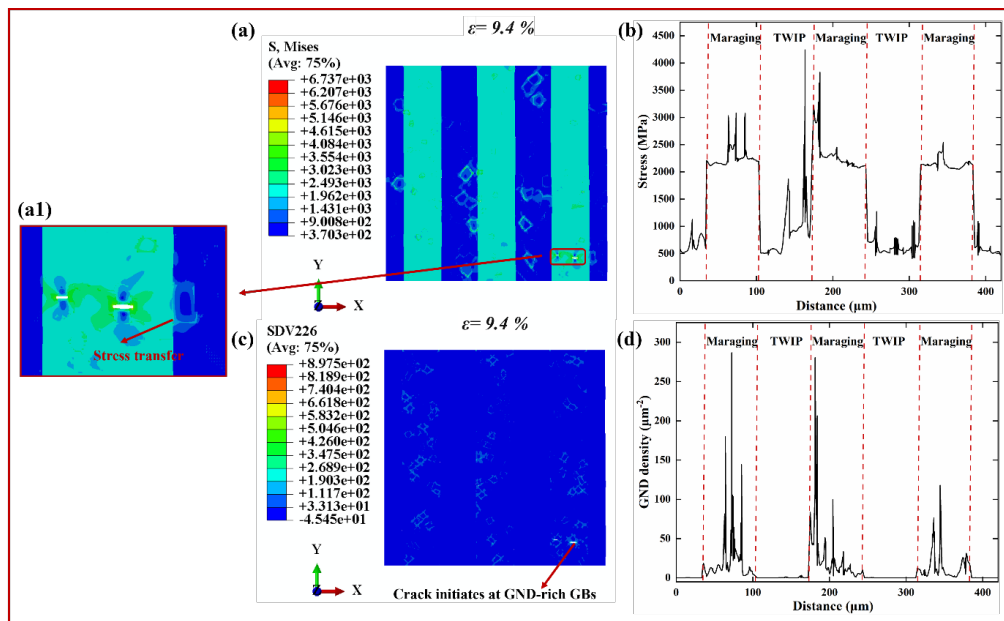


Figure 6.7: Simulated distribution of the von Mises stress for (a) the entire HSL specimen and (b) along “Path A”; simulated GND density for (c) the entire HSL specimen and (d) along “Path A”. Both the von Mises stress and the GND

density data are provided just before fracture, i.e. for a strain of 9.4 %.

6.3.3 Shear band and fracture formation

Figures 6.8(a) to (e) collectively show the predicted evolution of shear bands at various values of strain over the complete HSL model, while Figure 6.8(f) presents the tensile strain profile at fracture along “Path A”. From Figures 6.8(a) to (e), it can be observed that numerous, dispersed and gradually-evolving SBs were simulated over the TWIP/Maraging steel laminate, which correlates well with the experimental findings of (Zheng et al., 2022). It is seen that the amplitude of these dispersed SBs increases continuously with the increase in plastic strain. It is expected that this should result in delayed macroscopic strain localisation and enhanced strain hardening capability and ductility during deformation, as was also reported in (Lai et al., 2023).

As explained in (Yu et al., 2024), SBs form due to insufficient work hardening in the material, which cannot counteract geometric softening, resulting in the onset of such unstable mechanical disturbances. It is known that the process of shear banding in HSLs involves the nucleation of new bands, propagation along the shear plane, increase in width and increase in strain within the band. In this work, the SBs initiates at low strain in both Maraging and TWIP layer simultaneously as displayed in Figure 6.8(f). Their density remains nearly constant while the amplitude keeps increasing with applied tensile strain as confirmed in Figure 6.8(f). This result also aligns with the experimental finding from Fu and co-workers (Fu, Huang, et al., 2022). Besides, it was reported that SB orientations are determined by the macroscopic stress state (Jia et al., 2003). The orientation of the predicted SBs in the presented work are mostly around 45°-50° as displayed in Figure 6.8(a), which was also reported in (Nie et al., 2023; Peng et al., 2023; Sedighiani et al., 2022; Wagner et al., 1995). In addition, the simulated outcomes shown from Figure 6.8(a) to 9(e) indicate that the evolutionary behaviour of SBs in the modelled TWIP/Maraging steel laminates

shows X and W types. This is also aligned with the experimental observations as summarised in (Ma et al., 2023).

The higher density of GBs in the hard maraging layer noted earlier should significantly impede dislocation slip, leading to stress concentration at these boundaries. Consequently, these boundaries should serve as initiation sites for dispersed SBs. As the tensile strain surpasses the uniform elongation, strain localisation becomes increasingly pronounced. This promotes the growth of SBs in the hard maraging layer, causing them to deepen and widen, eventually evolving into micro-ditches, as illustrated in Figure 6.9(a). Fine cracks were found along the SB (see Figure 6.8(d)), which can lead ultimately to a local decrease in the tensile strength and finally to fracture (Baik et al., 2021).

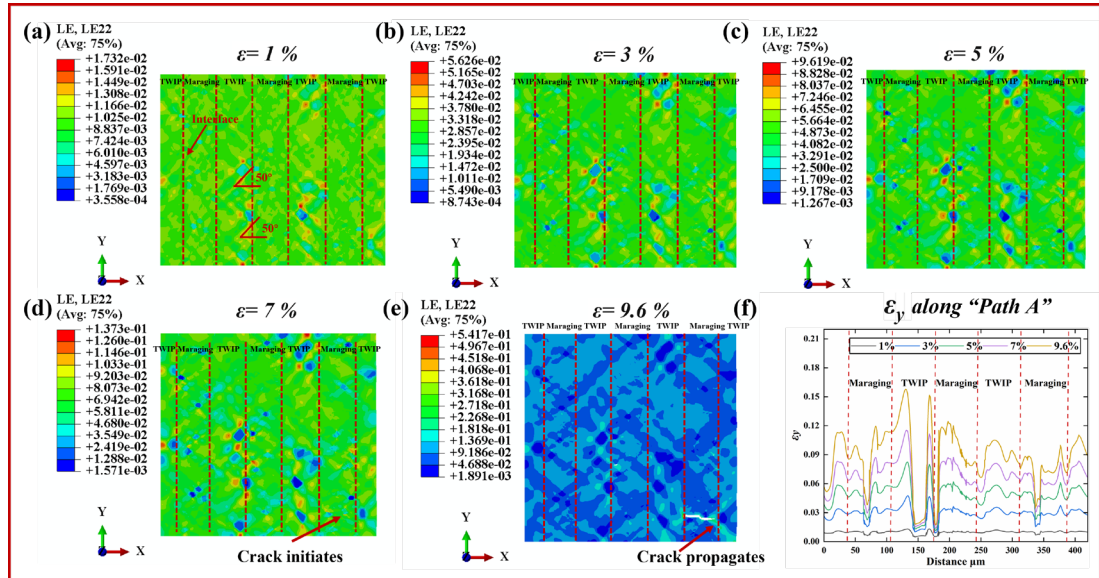


Figure 6.8: Evolutions of ε_y i.e., shear bands, in the simulated TWIP/Maraging steel laminates at strains of (a) 1%, (b) 3%, (c) 5%, (d) 7%, (e) 9.6% and (f) ε_y profile for a strain of 9.6% along “Path A”.

Figures 6.9(a) and 6.9(b) report the value of the CDM damage factor at fracture for the complete HSL model and along “Path A”, respectively. Figures 6.9(c) to 6.9(f) show the evolution of this damage factor for strain values from 7% and until fracture, i.e. 9.6%.

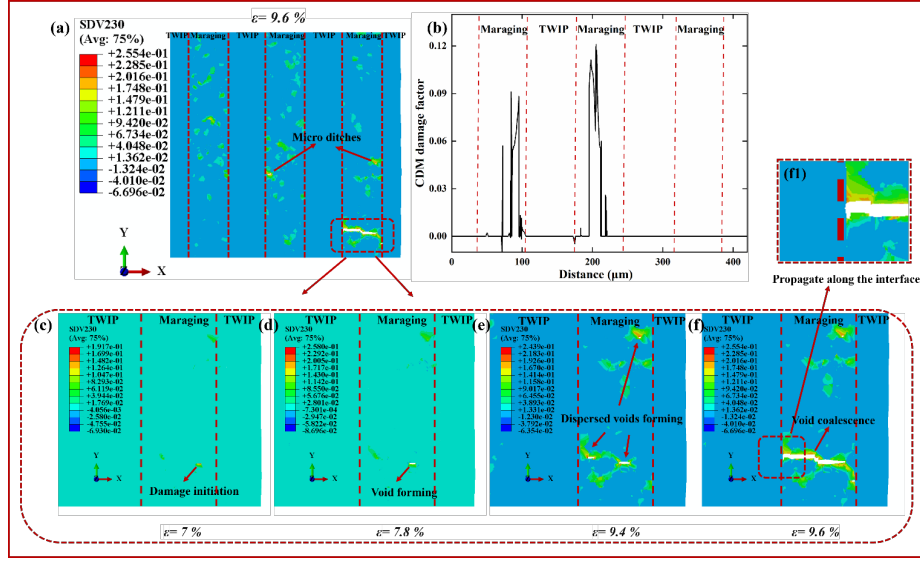


Figure 6.9: Distribution of CDM damage factor values at fracture for (a) the entire HSL specimen and (b) (b) along Path A; locally enlarged regions displaying the evolution of cracks in the simulated TWIP/Maraging steel laminates for strain values between of (c) 7 %, (d) 7.8%, (e) 9.4% and (f) 9.6%.

When the maximum slip becomes greater than a critical value γ_{ini} , damage initiates and accumulates as illustrated in equation (6.11). In this simulation, when the strain reaches 7%, localised damage nucleates in the hard Maraging layer first (see Figure 6.9(c)). This finding aligns well with the experimental study of (Xia et al., 2024) in which microcracks initiated in fine-grained layers of multilayered aluminium laminates. As tensile strain increases, the damaged area expands and new voids initiate, see Figure 6.9(d) and 6.9(e). These voids eventually coalesce leading to the fracture of this layer, see Figure 6.9(f). In contrast, as displayed in Figure 6.9(a) and (b), it is obvious that there is no damaged element in the TWIP layers of the laminates even after catastrophic fracture, exhibiting great ductility. Overall, it is notable that the void nucleation, growth, and coalescence phenomena of TWIP/Maraging laminates were well described by the proposed non-local CPFEM-CDM model.

In (Charpagne et al., 2021), it was revealed via high resolution digital image correlation (HR-DIC) data with 3D electron back-scatter diffraction

tomography (3D EBSD) that slip bands tend to emanate from triple junction of grains in monotonic tension of FCC polycrystals and would become critical crack nucleation sites during loading. In the presented work, it was validated that short microcracks were observed to nucleate at the hard Maraging layer first (Figure 6.9(c)), which is mainly attributed to the accumulation of GNDs (see Figure 6.7(c)), and the resultant stress concentration as also evidenced in the experimental report of (Han et al., 2023). Besides, strain localisation produces multiple uniformly distributed microcracks in the hard Maraging layer, see Figure 6.9 (a), which promote the bifurcation of the main crack and increase the surface energy during the main crack propagation, which further hinder its evolution. When the crack propagates towards the soft TWIP layer, its good ductility can relieve the local higher stress, reduce the rate of crack growth and blunt the crack tip. When the crack reaches the heterogeneous interface (Figure 6.9 (f)), it is interesting to observe that it changes orientation, i.e., along the interface, see Figure 6.9(f1). This increases the crack propagation path, i.e. hinders catastrophic fracture. It was also reported that the interface has a considerable strengthening toughening effect on the heterogeneous matrix composites, which can slow down the crack propagation (Peng et al., 2024). It is argued that the uneven stress partition between hard and soft layers in the TWIP/Maraging steel laminates resulted in the deflection of the main crack at the interfaces during tensile deformation. This delamination at the interfaces reduces triaxial stress conditions that promote crack growth and helps to passivate the crack tip, leading to a significant increase in material toughness (Kum et al., 1983).

Significant stress-drop due to damage softening at a strain of 2.2% was observed for the stand-alone Maraging layer (Figure 6.3). However, stress starts to drop at a strain of 9.4% for the TWIP/Maraging steel laminates (Figure 6.6). Comparing the stand-alone Maraging steel to the Maraging steel in the HSLs, the catastrophic fracture strain was not observed to increase. But the strain from void forming to catastrophic fracture was improved significantly, 11.2%-11.4%,

7%-9.6%. The fracture characteristics of the stand-alone Maraging layer indicates a fully brittle fracture. In contrast, the Maraging layer in the laminates features nucleation, growth, and coalescence of micro voids, classifying it as a mixed-mode fracture (Gao et al., 2024). In summary, the fracture mode of TWIP/Maraging steel laminates during uniaxial tensile loading is a combination of voids nucleation, growth, coalescence and deflection at the interface. The convolution of factors discussed above increases the crack growth path, consume more energy and reduce the crack growth rate (Zhou et al., 2023), which is an important reason for the improvement of the ductility of TWIP/Maraging steel laminates. Therefore, the layered structure design with alternating distribution of high-ductility soft layers and high-strength hard layers can significantly improve the fracture elongation of multilayered composites.

6.4 Conclusions

To date, numerous constitutive models have been devised to characterize the stress-strain behaviour and strengthening mechanisms of HSLs. However, these models often fail to address a wide range of application scenarios due to their homogenized nature, the absence of a well-defined relationship between stress and grain-level activities, and the lack of explicit consideration for fracture mechanisms. Herein, we propose a computational framework that integrates the non-local CPFEM and the CDM model to study the SBs evolution, GNDs and fracture of TWIP/Maraging steel laminates. The constructed non-local CPFEM-CDM framework not only ensure a more accurate grain-level representation of the underlying physical phenomena, but also predict the fracture characteristics which can achieve quantitative and non-empirical design of HSLs. Its effectiveness has been verified by simulating the deformation and fracture behaviour of stand-alone Maraging/TWIP layers and their laminates during the uniaxial tensile. The following conclusions are drawn:

-
- 1) The brittle and ductile fracture of homogeneous stand-alone Maraging/TWIP steel were accurately captured respectively via the progressive CDM criterion based on maximum slip.
 - 2) The predominant failure mechanism shifts from sudden catastrophic failure for stand-alone Maraging layer to void nucleation, coalescence and, ultimately, specimen cracking for Maraging layer in the HSLs. Specifically, the Maraging steel in the HSLs exhibits a higher prevalence of cracking compared to the stand-alone case and exhibits a brittle to ductile transition.
 - 3) The grain-level load transfer and strain partitioning between the two steel phases were distinctly modelled and their effect on the nucleation and growth of cracks within HSLs were investigated. GND was not observed to pile up at the interface. The crack initiates at the SBs in all cases studied but the numerical analysis of SBs alone is not sufficient to predict fracture. Although the magnitude of the SBs is higher in the soft layer, fracture still happened in the hard layer.
 - 4) The numerical results achieved excellent agreement on stress-strain behaviour and match the fracture characteristics within HSLs, displayed a good reliability. The synergistic effect of the two phases in the HSLs, effectively avoided stress/strain concentration, delayed the catastrophic failure.

In summary, although simplified Voronoi-based microstructures may not capture every intricate detail of real microstructures, the numerical model effectively replicates the fracture characteristics of HSLs through carefully chosen assumptions and computational techniques. This model provides a robust foundation for discussing the fracture behaviour of such laminates, as explored in this study. By incorporating grain-scale material responses and offering a systematic approach for identifying fracture parameters in HSLs, the framework enables insights that would otherwise require extensive and unconventional experimental efforts. Moreover, it presents an innovative perspective on improving ductility in these laminates.

Chapter 7 Conclusions and Future Work

7.1 Conclusions

This study focused on the numerical investigation of deformation mechanisms in HSMs, specifically, copper laminates, bi-layered HEA and TWIP/Maraging steel laminates. The primary aim was to quantify the synergistic effects arising from the strategic combination of these materials. The key contributions of this Thesis are as follows:

- I. Development of a MSGP modified JC model for the prediction of size effect and strain rate effect, with explicitly calculation of the strain gradient at each iteration step.
- II. Development and implementation of multiple-physical mechanisms-based FEM framework to quantify strengthening mechanisms and damage of HSLs.
- III. Full-field investigation of grain-level strengthening mechanisms in HSMs via the development of a non-local CPFEM framework.
- IV. Explicit numerical investigation of fracture mode transition of TWIP/Maraging steel laminates via the development a non-local CPFEM-CDM framework.

The specific contributions made, and the corresponding conclusions drawn are detailed below, aligned with the knowledge gaps identified in Chapter 2.

Knowledge gap 1: There is a lack of implementation of methodology to extract an explicit and real-time estimation of the plastic strain gradient within an MSGP-modified JC computational framework.

- A novel 3D MSGP-modified JC framework was developed in Chapter 3 in which the plastic strain gradient value could be extracted explicitly at every simulation time-step. Based on this model, tensile and torsion simulations were also conducted on microscale copper wires for a range of wire diameters and strain rates.
- The outcome of these simulations was shown to compare well against experimental data found in the literature. Based on this model, it was also possible to quantify the respective contribution of strain rate and strain gradient effect on the hardening of small-scale copper wire specimens.
- It is anticipated that this novel approach should not only enable the investigation of size, strain rate and temperature effects on material response to plastic deformation but also contribute to provide practitioners with a methodology for adapting conventional macroscale constitutive models towards performing microscale simulations.

Knowledge gap 2: A constitutive model which could quantitatively investigate the sources of hardening and the internal damage evolution of HSLs and to predict the response of such laminate materials under a range of deformation scenarios, including in tension and during nanoindentation is yet to be developed.

- A 3D multiple mechanism based constitutive model coupled with the JC failure criterion was established in Chapter 4 to investigate the deformation mechanisms of HSLs.

-
- The effect of GBs, dislocations and back stress from both grain level and sample level on the material properties of HSLs during uniaxial tension was investigated using the developed model.
 - Its implementation was realised using the ABAQUS/EXPLICIT subroutine which allows its usage in dynamic metal micro-forming processes.

Knowledge gap 3: While a non-local CPFEM model was developed for the investigation of heterostructured materials in (Zhang, Zhao, et al., 2023; Yong Zhang et al., 2024), grains were not explicitly considered in these studies. As a result, mechanisms such as shear band and grain rotation could not be captured.

- A novel CPFEM framework was developed in Chapter 5 to reproduce and confirm a number of known experimental findings, namely that 1) shear bands and damage propagate among grains sharing similar orientation and 2) significant rotation and slip take place in grains subjected to severe damage. Based on this, it is suggested that the properties of heterostructured materials could be further enhanced not only by controlling the grain size and dislocation density gradients, but also by controlling the initial grouping of grains and their respective orientations as well.
- For the heterostructured bi-layered HEA modelled in Chapter 5, it was interesting to notice that GNDs accumulated at grain boundaries, rather than at the hetero-interface.
- It is suggested that the JC damage criterion could also be employed to characterise shear bands evolution, which in turn could lead to the identification of potential crack nucleation sites.

Knowledge gap 4: The intriguing synergy effect during the deformation process of metallic HSMs is still not fully understood due to the difficulties in accurate description of the real ‘fracture’ process at the microscale.

- The work in Chapter 6 investigated the strengthening mechanisms and fracture modes in HSLs through a full-field non-local CPFEM framework and incorporated progressive continuum damage mechanics (CDM) model for the crack initiation and propagation.
- It was observed that the non-local CPFEM-CDM model based on maximum slip accurately captured the typical brittle and ductile damage of stand-alone Maraging steel and TWIP steel.
- It was further found that the hard Maraging layer reside in the HSLs exhibited a fracture process of void nucleation, coalescence and propagation, displayed a brittle to ductile fracture trend which was in stark contrast to stand-alone Maraging layer where a typical brittle fracture was observed.
- These findings were in good agreement with recent experimental observations in terms of stress-strain responses, SBs evolution and fracture mode. The enhanced ductility of HSLs originated from the heterogeneous deformation-induced (HDI) stable SBs evolution during tension.

7.2 Future work

Based on the research investigations reported in this Thesis, several potential directions for future work, corresponding to Chapter 3, 4, 5 and 6 respectively, have been identified as follows:

1. It is anticipated that the concise mathematical formulation proposed in this work should enable practitioners to re-use readily available material properties for the simulation of small-scale specimens at different strain rates. In this way, efforts in complementing additional

small scale experimental data to fit a pre-existing model may be reduced. In particular, the proposed model provides a straightforward and easy-to-implement pathway to extend the use of continuum plasticity-based finite element simulations package to micro/sub-micro scale effectively. One should notice that while the presented findings in Chapter 3 are aligned with existing experimental data, the work would still benefit from further experimental validations which would more closely match the reported simulations. Besides, for a typical dislocation density on the order of $10^{15}/\text{m}^2$, the average dislocation spacing is around 30 nm such that the MSGP-modified JC flow stress expression holds at a scale above 100 nm. Future work should also focus on studying the influence of the temperature against the contribution of the strain rate and plastic strain gradient based on the presented model.

2. It is anticipated that the developed framework in Chapter 4 could be readily extended to simulate other metallic heterogeneous materials, particularly in the context of dynamic manufacturing processes such as forming. The proposed framework is versatile and should support the application of metallic laminates and, potentially, gradient metallic structures, by enabling the optimal design of such materials. However, to further enhance the predictive capability and physical relevance of the model, more realistic deformation mechanisms should be incorporated. While the current work focuses on dislocation pile-up as a primary factor, yielding a good correlation between numerical and experimental results, it is important to note that the deformation mechanisms in heterogeneous materials are inherently complex. Future efforts should consider additional factors such as grain boundary interactions, twinning, phase transformations, and the role of interfaces, which play a critical role in governing the mechanical behaviour of these materials.

Particular attention should be paid to the interfaces between different material phases or layers, as they often act as sites for stress concentration, crack initiation, and dislocation accumulation. A more detailed representation of interface properties and their evolution during deformation could significantly improve the accuracy and applicability of the framework. By incorporating these aspects, the proposed model could provide deeper insights into the deformation behaviour of heterostructured materials and support the development of advanced materials with tailored mechanical properties for specific applications.

3. Although GNDs were not explicitly observed in the presented work in Chapter 5, prior studies have reported that GNDs tend to accumulate near interfaces, particularly when the grain size ratio between hard and soft phases is significant. This phenomenon is attributed to the strain gradient plasticity effects that arise due to the mechanical incompatibility between regions of differing grain sizes. Specifically, when the grain size ratio exceeds a certain threshold, the strain gradients at the interfaces become more pronounced, leading to a higher density of GNDs near these boundaries compared to the grain interiors. Future work should systematically investigate whether a critical threshold exists for the size ratio between fine and coarse grain regions, beyond which GND accumulation at interfaces becomes dominant over grain-scale GNDs. Such a study would provide valuable insights into the micromechanical mechanisms governing heterostructured materials and could help establish design guidelines for optimizing interface-dominated strengthening effects. Additionally, exploring the role of other factors, such as interface geometry, crystallographic orientation, and loading conditions, in influencing GND distribution would further enhance our understanding of the deformation behaviour in these materials.

4. Explicit modelling of orientation information, including re-orientation effects, of polycrystalline grains should be considered in future research as a complement to Chapter 6. A detailed investigation into the initial crystallographic orientation of grains and their re-orientation during mechanical deformation would provide critical insights into the interplay between microstructure and macroscopic mechanical properties. Such an approach would enable the quantification of how grain orientation gradients, texture evolution, and local strain partitioning influence the overall mechanical response. Indeed, a systematic study on the influence of grain orientation and its evolution under varying loading conditions would pave the way toward a more quantitative understanding of the role of heterogeneous microstructures. This could significantly advance the design and optimization of a broader class of heterostructured materials with tailored mechanical properties.

Appendix: mesh convergence

To demonstrate that the mesh resolution is sufficiently high in this work, a 3D RVE with 10 grains is generated with different mesh numbers: 2304, 3600 and 4624, using Neper. The tensile stress-strain curves with different mesh resolutions are shown in Fig. A1 below. The results indicate that as the element number increases from 2304 to 4624, the stress-strain curves nearly overlap. Therefore, to ensure the accuracy of the results and reduce the computation cost simultaneously, 200 elements per grain are used for mesh in this work.

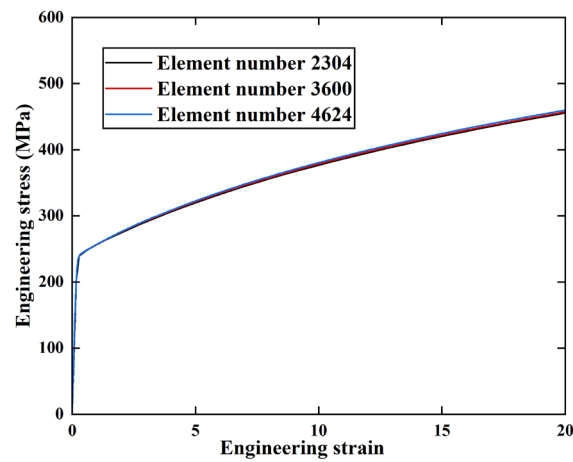


Fig. A1: Mesh convergence study on the developed framework.

Bibliography

- Ahmadikia, B., Kumar, M. A., & Beyerlein, I. J. (2021). Effect of neighboring grain orientation on strain localization in slip bands in HCP materials. *International Journal of Plasticity*, 144. <https://doi.org/10.1016/j.ijplas.2021.103026>
- Antunes, J. M., Fernandes, J. V., Menezes, L. F., & Chaparro, B. M. (2007). A new approach for reverse analyses in depth-sensing indentation using numerical simulation. *Acta Materialia*, 55(1), 69-81. <https://doi.org/https://doi.org/10.1016/j.actamat.2006.08.019>
- Antunes, J. M., Menezes, L. F., & Fernandes, J. V. (2006). Three-dimensional numerical simulation of Vickers indentation tests. *International Journal of Solids and Structures*, 43(3), 784-806. <https://doi.org/https://doi.org/10.1016/j.ijsolstr.2005.02.048>
- Arsenlis, A., & Parks, D. M. (1999). Crystallographic aspects of geometrically-necessary and statistically-stored dislocation density. *Acta Materialia*, 47(5), 1597-1611. [https://doi.org/https://doi.org/10.1016/S1359-6454\(99\)00020-8](https://doi.org/https://doi.org/10.1016/S1359-6454(99)00020-8)
- Ashby, M. F. (1970). The deformation of plastically non-homogeneous materials. *The Philosophical Magazine: A Journal of Theoretical Experimental and Applied Physics*, 21(170), 399-424. <https://doi.org/10.1080/14786437008238426>
- Backes, B., Huang, Y. Y., Göken, M., & Durst, K. (2009). The correlation between the internal material length scale and the microstructure in nanoindentation experiments and simulations using the conventional mechanism-based strain gradient plasticity theory. *Journal of Materials Research*, 24(3), 1197-1207. <https://doi.org/10.1557/jmr.2009.0123>
- Baik, S.-I., Gupta, R. K., Kumar, K. S., & Seidman, D. N. (2021). Temperature increases and thermoplastic microstructural evolution in adiabatic shear bands in a high-strength and high-toughness 10 wt.% Ni steel. *Acta Materialia*, 205. <https://doi.org/10.1016/j.actamat.2020.116568>
- Bandyopadhyay, R., Gustafson, S. E., Kapoor, K., Naragani, D., Pagan, D. C., & Sangid, M. D. (2021). Comparative assessment of backstress models using high-energy X-ray diffraction microscopy experiments and crystal plasticity finite element simulations. *International Journal of Plasticity*, 136. <https://doi.org/10.1016/j.ijplas.2020.102887>
- Beausir, B., Tóth, L. S., & Neale, K. W. (2007). Ideal orientations and persistence characteristics of hexagonal close packed crystals in simple shear. *Acta Materialia*, 55(8), 2695-2705. <https://doi.org/10.1016/j.actamat.2006.12.021>
- Boubaker, H. B., Moufki, A., Nouari, M., Laheurte, P., & Tidu, A. (2021). Thermodynamically consistent formulation coupling crystal plasticity theory and Johnson-Cook damage model to simulate micromachining of copper. *Procedia CIRP*, 102, 506-511. <https://doi.org/https://doi.org/10.1016/j.procir.2021.09.086>
- Byon, S. M., Moon, C. H., & Lee, Y. (2009). Strain gradient plasticity based finite element analysis of ultra-fine wire drawing process. *Journal of Mechanical Science and Technology*, 23(12), 3374-3384. <https://doi.org/10.1007/s12206-009-0926-y>
- Chakrabarty, R., & Song, J. (2020). A modified Johnson-Cook material model with strain gradient plasticity consideration for numerical simulation of cold spray process. *Surface and Coatings Technology*, 397, 125981. <https://doi.org/https://doi.org/10.1016/j.surfcoat.2020.125981>
- Champion, Y., Langlois, C., Guérin-Mailly, S., Langlois, P., Bonnentien, J.-L., & Hÿtch, M. J. (2003). Near-Perfect Elastoplasticity in Pure Nanocrystalline Copper. *Science*,

-
- 300(5617), 310-311. <https://doi.org/10.1126/science.1081042>
- Chang, Y. Q., Kong, L. W., Zhu, X. L., Zhu, X. F., Cao, J., Wen, B., & Li, P. (2022). Investigation on the strengthening behaviour of micro-scale copper fiber. *Materials Science and Engineering: A*, 859, 144186. <https://doi.org/https://doi.org/10.1016/j.msea.2022.144186>
- Charpagne, M. A., Hestroffer, J. M., Polonsky, A. T., Echlin, M. P., Texier, D., Valle, V., Beyerlein, I. J., Pollock, T. M., & Stinville, J. C. (2021). Slip localization in Inconel 718: A three-dimensional and statistical perspective. *Acta Materialia*, 215. <https://doi.org/10.1016/j.actamat.2021.117037>
- Chen, T., & Li, J. (2021). Modelling the Shear Banding in Gradient Nano-Grained Metals. *Nanomaterials*, 11(10).
- Chen, W., Voisin, T., Zhang, Y., Forien, J.-B., Spadaccini, C. M., McDowell, D. L., Zhu, T., & Wang, Y. M. (2019). Microscale residual stresses in additively manufactured stainless steel. *Nature Communications*, 10(1), 4338. <https://doi.org/10.1038/s41467-019-12265-8>
- Chen, W., You, Z. S., Tao, N. R., Jin, Z. H., & Lu, L. (2017). Mechanically-induced grain coarsening in gradient nano-grained copper. *Acta Materialia*, 125, 255-264. <https://doi.org/https://doi.org/10.1016/j.actamat.2016.12.006>
- Cheng, Z., Bu, L., Zhang, Y., Wu, H., Zhu, T., & Lu, L. (2023). Characterization of gradient plastic deformation in gradient nanotwinned Cu. *Acta Materialia*, 246, 118673. <https://doi.org/https://doi.org/10.1016/j.actamat.2023.118673>
- Cheng, Z., Zhou, H., Lu, Q., Gao, H., & Lu, L. (2018). Extra strengthening and work hardening in gradient nanotwinned metals. *Science*, 362(6414), eaau1925. <https://doi.org/10.1126/science.aau1925>
- Das, S., Hofmann, F., & Tarleton, E. (2018). Consistent determination of geometrically necessary dislocation density from simulations and experiments. *International Journal of Plasticity*, 109, 18-42. <https://doi.org/10.1016/j.ijplas.2018.05.001>
- Dasharath, S. M., & Mula, S. (2016). Mechanical properties and fracture mechanisms of ultrafine grained Cu-9.6% Zn alloy processed by multiaxial cryoforging. *Materials Science and Engineering: A*, 675, 403-414. <https://doi.org/https://doi.org/10.1016/j.msea.2016.08.086>
- Demir, E., Martinez-Pechero, A., Hardie, C., & Tarleton, E. (2024a). OXFORD-UMAT: An efficient and versatile crystal plasticity framework. *International Journal of Solids and Structures*. <https://doi.org/10.1016/j.ijsolstr.2024.113110>
- Demir, E., Martinez-Pechero, A., Hardie, C., & Tarleton, E. (2024b). Restraining geometrically-necessary dislocations to the active slip systems in a crystal plasticity-based finite element framework. *International Journal of Plasticity*. <https://doi.org/10.1016/j.ijplas.2024.104013>
- Dève, H., Harren, S., McCullough, C., & Asaro, R. J. (1988). Micro and macroscopic aspects of shear band formation in internally nitrated single crystals of Fe-Ti-Mn alloys. *Acta Metallurgica*, 36(2), 341-365. [https://doi.org/https://doi.org/10.1016/0001-6160\(88\)90011-9](https://doi.org/https://doi.org/10.1016/0001-6160(88)90011-9)
- Ding, K., Zhang, Y., Birnbaum, A. J., Michopoulos, J. G., McDowell, D. L., & Zhu, T. (2021). Strain gradient plasticity modeling of nanoindentation of additively manufactured stainless steel. *Extreme Mechanics Letters*, 49, 101503. <https://doi.org/https://doi.org/10.1016/j.eml.2021.101503>
- Doan, D.-Q., Tran, A.-S., & Vu, N.-C. (2023). Grain and twin boundaries dependent mechanical behavior of FeCoCrNiCu high-entropy alloy. *Materials Today Communications*, 34. <https://doi.org/10.1016/j.mtcomm.2022.104975>

-
- Dunne, F. P. E., Rugg, D., & Walker, A. (2007). Lengthscale-dependent, elastically anisotropic, physically-based hcp crystal plasticity: Application to cold-dwell fatigue in Ti alloys. *International Journal of Plasticity*, 23(6), 1061-1083. <https://doi.org/10.1016/j.ijplas.2006.10.013>
- El-Deiry, P. A., & Vinci, R. P. (2001). Strain Rate Dependent Behavior of Pure Aluminum and Copper Micro-Wires. *MRS Online Proceedings Library (OPL)*, 695, L4.2.1, Article L4.2.1. <https://doi.org/10.1557/PROC-695-L4.2.1>
- Estrin, Y. (1998). Dislocation theory based constitutive modelling: foundations and applications. *Journal of Materials Processing Technology*, 80-81, 33-39. [https://doi.org/https://doi.org/10.1016/S0924-0136\(98\)00208-8](https://doi.org/https://doi.org/10.1016/S0924-0136(98)00208-8)
- Fan, G., Geng, L., Wu, H., Miao, K., Cui, X., Kang, H., Wang, T., Xie, H., & Xiao, T. (2017). Improving the tensile ductility of metal matrix composites by laminated structure: A coupled X-ray tomography and digital image correlation study. *Scripta Materialia*, 135, 63-67. <https://doi.org/https://doi.org/10.1016/j.scriptamat.2017.03.030>
- Fan, M., Domblesky, J., Jin, K., Qin, L., Cui, S., Guo, X., Kim, N., & Tao, J. (2016). Effect of original layer thicknesses on the interface bonding and mechanical properties of TiAl laminate composites. *Materials & Design*, 99, 535-542. <https://doi.org/https://doi.org/10.1016/j.matdes.2016.03.102>
- Fan, P., Goel, S., Luo, X., & Upadhyaya, H. M. (2022). Atomic-Scale Friction Studies on Single-Crystal Gallium Arsenide Using Atomic Force Microscope and Molecular Dynamics Simulation. *Nanomanufacturing and Metrology*, 5(1), 39-49. <https://doi.org/10.1007/s41871-021-00109-3>
- Fan, W., Peng, Y., Qi, Y., Tan, H., Feng, Z., Wang, Y., Zhang, F., & Lin, X. (2023). Partially melted powder in laser based directed energy deposition: Formation mechanism and its influence on microstructure. *International Journal of Machine Tools and Manufacture*, 192. <https://doi.org/10.1016/j.ijmachtools.2023.104072>
- Fan, Y., Xu, Y., Hao, Z., & Lin, J. (2022a). Cutting deformation mechanism of SiCp/Al composites based on strain gradient theory. *Journal of Materials Processing Technology*, 299, 117345. <https://doi.org/https://doi.org/10.1016/j.jmatprotec.2021.117345>
- Fan, Y., Xu, Y., Hao, Z., & Lin, J. (2022b). Cutting deformation mechanism of SiCp/Al composites based on strain gradient theory. *Journal of Materials Processing Technology*, 299. <https://doi.org/10.1016/j.jmatprotec.2021.117345>
- Fang, Q., Chen, Y., Li, J., Jiang, C., Liu, B., Liu, Y., & Liaw, P. K. (2019). Probing the phase transformation and dislocation evolution in dual-phase high-entropy alloys. *International Journal of Plasticity*, 114, 161-173. <https://doi.org/10.1016/j.ijplas.2018.10.014>
- Fang, Q., Li, L., Li, J., & Wu, H. (2018). Strengthening mechanism of gradient nanostructured body-centred cubic iron film: From inverse Hall-Petch to classic Hall-Petch. *Computational Materials Science*, 152, 236-242. <https://doi.org/https://doi.org/10.1016/j.commatsci.2018.06.001>
- Fang, T. H., Li, W. L., Tao, N. R., & Lu, K. (2011). Revealing Extraordinary Intrinsic Tensile Plasticity in Gradient Nano-Grained Copper. *Science*, 331(6024), 1587-1590. <https://doi.org/10.1126/science.1200177>
- Fleck, N. A., & Hutchinson, J. W. (1993). A phenomenological theory for strain gradient effects in plasticity. *Journal of the Mechanics and Physics of Solids*, 41(12), 1825-1857. [https://doi.org/https://doi.org/10.1016/0022-5096\(93\)90072-N](https://doi.org/https://doi.org/10.1016/0022-5096(93)90072-N)
- Fleck, N. A., & Hutchinson, J. W. (1997). Strain gradient plasticity. *Advances in Applied Mechanics*, 33, 295-361.
- Fleck, N. A., Muller, G. M., Ashby, M. F., & Hutchinson, J. W. (1994). Strain gradient

-
- plasticity: Theory and experiment. *Acta Metallurgica et Materialia*, 42(2), 475-487. [https://doi.org/https://doi.org/10.1016/0956-7151\(94\)90502-9](https://doi.org/https://doi.org/10.1016/0956-7151(94)90502-9)
- Fu, W., Huang, Y., Sun, J., & Ngan, A. H. W. (2022). Strengthening CrFeCoNiMn0.75Cu0.25 high entropy alloy via laser shock peening. *International Journal of Plasticity*, 154. <https://doi.org/10.1016/j.ijplas.2022.103296>
- Fu, W., Li, H., Huang, Y., Ning, Z., & Sun, J. (2022). A new strategy to overcome the strength-ductility trade off of high entropy alloy. *Scripta Materialia*, 214. <https://doi.org/10.1016/j.scriptamat.2022.114678>
- Fu, W., Sun, Y., Fan, G., Huang, Y., Ning, Z., Li, X., Wang, K., Sun, J., & Jiang, S. (2023). Strain delocalization in a gradient-structured high entropy alloy under uniaxial tensile loading. *International Journal of Plasticity*, 171. <https://doi.org/10.1016/j.ijplas.2023.103808>
- Gao, G., Liu, B., Feng, J., & Ji, P. (2024). Effect of Multilayer Structure and Column Array Structure on Mechanical Properties and Fracture Behavior of Heterogeneous Steel. *Journal of Materials Engineering and Performance*. <https://doi.org/10.1007/s11665-024-09944-z>
- Gao, H., Huang, Y., Nix, W. D., & Hutchinson, J. W. (1999). Mechanism-based strain gradient plasticity – I. Theory. *Journal of the Mechanics and Physics of Solids*, 47(6), 1239-1263. [https://doi.org/https://doi.org/10.1016/S0022-5096\(98\)00103-3](https://doi.org/https://doi.org/10.1016/S0022-5096(98)00103-3)
- Gao, S., Yoshino, K., Terada, D., Kaneko, Y., & Tsuji, N. (2022). Significant Bauschinger effect and back stress strengthening in an ultrafine grained pure aluminum fabricated by severe plastic deformation process. *Scripta Materialia*, 211. <https://doi.org/10.1016/j.scriptamat.2022.114503>
- Gao, T. J., Zhao, D., Zhang, T. W., Jin, T., Ma, S. G., & Wang, Z. H. (2020). Strain-rate-sensitive mechanical response, twinning, and texture features of NiCoCrFe high-entropy alloy: Experiments, multi-level crystal plasticity and artificial neural networks modeling. *Journal of Alloys and Compounds*, 845. <https://doi.org/10.1016/j.jallcom.2020.155911>
- Geng, Y., Wang, J., Li, Z., Yan, Y., Zhang, J., & Gan, Y. (2022). Comparison of the Indentation Processes Using the Single Indenter and Indenter Array: A Molecular Dynamics Study. *Nanoscale Research Letters*, 17(1), 49. <https://doi.org/10.1186/s11671-022-03686-4>
- Geng, Y., Zhang, J., Yan, Y., Yu, B., Geng, L., & Sun, T. (2015). Experimental and Theoretical Investigation of Crystallographic Orientation Dependence of Nanoscratching of Single Crystalline Copper. *PLOS ONE*, 10(7), e0131886. <https://doi.org/10.1371/journal.pone.0131886>
- Giessen, E. V. d., & Needleman, A. (1995). Discrete dislocation plasticity: a simple planar model. *Modelling and Simulation in Materials Science and Engineering*, 3(5), 689. <https://doi.org/10.1088/0965-0393/3/5/008>
- Goel, S., Chavoshi, S. Z., & Murphy, A. (2017). Molecular dynamics simulation (MDS) to study nanoscale machining processes.
- Griesbach, C., Bronkhorst, C. A., & Thevamaran, R. (2024). Crystal plasticity simulations reveal cooperative plasticity mechanisms leading to enhanced strength and toughness in gradient nanostructured metals. *Acta Materialia*, 270. <https://doi.org/10.1016/j.actamat.2024.119835>
- Gu, D., Shi, X., Poprawe, R., Bourell, D. L., Setchi, R., & Zhu, J. (2021). Material-structure-performance integrated laser-metal additive manufacturing. *Science*, 372(6545), eabg1487. <https://doi.org/10.1126/science.abg1487>
- Güler, B., Şimşek, Ü., Yalçinkaya, T., & Efe, M. (2018). *Grain-scale investigations of deformation heterogeneities in aluminum alloys*

-
- Guo, S., He, Y., Lei, J., Li, Z., & Liu, D. (2017). Individual strain gradient effect on torsional strength of electropolished microscale copper wires. *Scripta Materialia*, 130, 124-127. <https://doi.org/https://doi.org/10.1016/j.scriptamat.2016.11.029>
- Guo, X., Ji, R., Weng, G. J., Zhu, L. L., & Lu, J. (2014). Micromechanical simulation of fracture behavior of bimodal nanostructured metals. *Materials Science and Engineering: A*, 618, 479-489. <https://doi.org/https://doi.org/10.1016/j.msea.2014.09.036>
- Guo, X., Sun, X., Tian, X., Weng, G. J., Ouyang, Q. D., & Zhu, L. L. (2016). Simulation of ballistic performance of a two-layered structure of nanostructured metal and ceramic. *Composite Structures*, 157, 163-173. <https://doi.org/https://doi.org/10.1016/j.compstruct.2016.08.025>
- Guo, X., Yang, G., Weng, G. J., & Zhu, L. L. (2015). Numerical simulation of ballistic performance of bimodal nanostructured metals. *Materials Science and Engineering: A*, 630, 13-26. <https://doi.org/https://doi.org/10.1016/j.msea.2015.01.081>
- Han, F., Jiang, Y., Cao, F., Cai, L., Zhang, H., & Liang, S. (2023). Role of gradient heterogeneous interfaces in synergetic strengthening and toughening of layered CuCrZr/Cu composites. *Materials Science and Engineering: A*, 885. <https://doi.org/10.1016/j.msea.2023.145613>
- Haouala, S., Lucarini, S., Llorca, J., & Segurado, J. (2020). Simulation of the Hall-Petch effect in FCC polycrystals by means of strain gradient crystal plasticity and FFT homogenization. *Journal of the Mechanics and Physics of Solids*, 134, 103755. <https://doi.org/https://doi.org/10.1016/j.jmps.2019.103755>
- Hardie, C., Long, D. J., Demir, E., Tarleton, E., & Dunne, F. P. E. (2023). A robust and efficient hybrid solver for crystal plasticity. *International Journal of Plasticity*, 170. <https://doi.org/10.1016/j.ijplas.2023.103773>
- Harsono, E., Swaddiwudhipong, S., Liu, Z. S., & Shen, L. (2011). Numerical and experimental indentation tests considering size effects. *International Journal of Solids and Structures*, 48(6), 972-978. <https://doi.org/https://doi.org/10.1016/j.ijsolstr.2010.12.002>
- Hasan, M. N., Liu, Y. F., An, X. H., Gu, J., Song, M., Cao, Y., Li, Y. S., Zhu, Y. T., & Liao, X. Z. (2019). Simultaneously enhancing strength and ductility of a high-entropy alloy via gradient hierarchical microstructures. *International Journal of Plasticity*, 123, 178-195. <https://doi.org/10.1016/j.ijplas.2019.07.017>
- Hirth, J. P., Lothe, J., & Mura, T. (1983). Theory of Dislocations (2nd ed.). *Journal of Applied Mechanics*, 50, 476. <https://doi.org/10.1115/1.3167075>
- Hosford, W. F. (1993). The mechanics of crystals and textured polycrystals.
- Hou, Y., Zhang, W., Mi, X., Xie, H., Feng, X., Huang, G., Peng, L., & Yang, Z. (2022). Different response mechanisms of yield strength and ultimate tensile strength in pure copper considering size effect. *Materials Science and Engineering: A*, 849, 143443. <https://doi.org/https://doi.org/10.1016/j.msea.2022.143443>
- Huang, C. X., Wang, Y. F., Ma, X. L., Yin, S., Höppel, H. W., Göken, M., Wu, X. L., Gao, H. J., & Zhu, Y. T. (2018). Interface affected zone for optimal strength and ductility in heterogeneous laminate. *Materials Today*, 21(7), 713-719. <https://doi.org/https://doi.org/10.1016/j.mattod.2018.03.006>
- Huang, K., Sumigawa, T., & Kitamura, T. (2020). Load-dependency of damage process in tension-compression fatigue of microscale single-crystal copper. *International Journal of Fatigue*, 133, 105415. <https://doi.org/https://doi.org/10.1016/j.ijfatigue.2019.105415>
- Huang, M., Xu, C., Fan, G., Maawad, E., Gan, W., Geng, L., Lin, F., Tang, G., Wu, H., Du, Y., Li, D., Miao, K., Zhang, T., Yang, X., Xia, Y., Cao, G., Kang, H., Wang, T., Xiao, T., & Xie, H. (2018). Role of layered structure in ductility improvement of layered Ti-Al

-
- metal composite. *Acta Materialia*, 153, 235-249.
<https://doi.org/https://doi.org/10.1016/j.actamat.2018.05.005>
- Huang, Y., Qu, S., Hwang, K. C., Li, M., & Gao, H. (2004). A conventional theory of mechanism-based strain gradient plasticity. *International Journal of Plasticity*, 20(4), 753-782. <https://doi.org/https://doi.org/10.1016/j.ijplas.2003.08.002>
- Jamalian, M., & Field, D. P. (2020). Effect of gradient microstructures on strengthening and toughening of AZ31. *Materials Science and Engineering: A*, 771. <https://doi.org/10.1016/j.msea.2019.138615>
- Ji, W., Zhou, R., Vivegananthan, P., See Wu, M., Gao, H., & Zhou, K. (2023). Recent progress in gradient-structured metals and alloys. *Progress in Materials Science*, 140, 101194. <https://doi.org/https://doi.org/10.1016/j.pmatsci.2023.101194>
- Jia, D., Ramesh, K. T., & Ma, E. (2003). Effects of nanocrystalline and ultrafine grain sizes on constitutive behavior and shear bands in iron. *Acta Materialia*, 51(12), 3495-3509. [https://doi.org/10.1016/s1359-6454\(03\)00169-1](https://doi.org/10.1016/s1359-6454(03)00169-1)
- Jia, N., Eisenlohr, P., Roters, F., Raabe, D., & Zhao, X. (2012). Orientation dependence of shear banding in face-centered-cubic single crystals. *Acta Materialia*, 60(8), 3415-3434. <https://doi.org/10.1016/j.actamat.2012.03.005>
- Jiang, Y., Feng, Z., & Tao, L. (2023). Deformation mechanisms based on the multiscale molecular dynamics of a gradient TA1 titanium alloy. *Nanoscale*, 16(1), 447-461. <https://doi.org/10.1039/d3nr03600f>
- Johnson, G. R., & Cook, W. H. (1985). Fracture characteristics of three metals subjected to various strains, strain rates, temperatures and pressures. *Engineering Fracture Mechanics*, 21(1), 31-48. [https://doi.org/https://doi.org/10.1016/0013-7944\(85\)90052-9](https://doi.org/https://doi.org/10.1016/0013-7944(85)90052-9)
- Johnson, G. R., & Cook, W. H. (2018). A CONSTITUTIVE MODEL AND DATA FOR METALS SUBJECTED TO LARGE STRAINS, HIGH STRAIN RATES AND HIGH TEMPERATURES.
- Joshi, S. S., & Melkote, S. N. (2005). An Explanation for the Size-Effect in Machining Using Strain Gradient Plasticity. *Journal of Manufacturing Science and Engineering*, 126(4), 679-684. <https://doi.org/10.1115/1.1688375>
- Kapoor, K., Yoo, Y. S. J., Book, T. A., Kacher, J. P., & Sangid, M. D. (2018). Incorporating grain-level residual stresses and validating a crystal plasticity model of a two-phase Ti-6Al-4 V alloy produced via additive manufacturing. *Journal of the Mechanics and Physics of Solids*, 121, 447-462. <https://doi.org/10.1016/j.jmps.2018.07.025>
- Kareer, A., Hou, X. D., Jennett, N. M., & Hainsworth, S. V. (2016a). The existence of a lateral size effect and the relationship between indentation and scratch hardness in copper. *Philosophical Magazine*, 96(32-34), 3396-3413. <https://doi.org/10.1080/14786435.2016.1146828>
- Kareer, A., Hou, X. D., Jennett, N. M., & Hainsworth, S. V. (2016b). The interaction between Lateral size effect and grain size when scratching polycrystalline copper using a Berkovich indenter. *Philosophical Magazine*, 96(32-34), 3414-3429. <https://doi.org/10.1080/14786435.2016.1240881>
- Karimzadeh, A., & Ayatollahi, M. R. (2012). Investigation of mechanical and tribological properties of bone cement by nano-indentation and nano-scratch experiments. *Polymer Testing*, 31(6), 828-833. <https://doi.org/https://doi.org/10.1016/j.polymertesting.2012.06.002>
- Karimzadeh, A., R. Koloor, S. S., Ayatollahi, M. R., Bushroa, A. R., & Yahya, M. Y. (2019). Assessment of Nano-Indentation Method in Mechanical Characterization of Heterogeneous Nanocomposite Materials Using Experimental and Computational

-
- Approaches. *Scientific Reports*, 9(1), 15763. <https://doi.org/10.1038/s41598-019-51904-4>
- Karthik, G. M., & Kim, H. S. (2021). Heterogeneous Aspects of Additive Manufactured Metallic Parts: A Review. *Metals and Materials International*, 27(1), 1-39. <https://doi.org/10.1007/s12540-020-00931-2>
- Kasaei, M. M., Beygi, R., Carbas, R. J. C., Marques, E. A. S., & da Silva, L. F. M. (2023). A review on mechanical and metallurgical joining by plastic deformation. *Discover Mechanical Engineering*, 2(1), 5. <https://doi.org/10.1007/s44245-023-00012-9>
- Kasaeian-Naeini, M., Sedighi, M., & Hashemi, R. (2022). Severe plastic deformation (SPD) of biodegradable magnesium alloys and composites: A review of developments and prospects. *Journal of Magnesium and Alloys*, 10(4), 938-955. <https://doi.org/https://doi.org/10.1016/j.jma.2021.11.006>
- Khandai, D. K., Mathew, J., & Kuriachen, B. (2022). FEM modelling of residual stresses of Ti-6Al-4V during micro-turning considering the scale effect. *Sādhanā*, 47(2), 107. <https://doi.org/10.1007/s12046-022-01865-8>
- Kiener, D., Grosinger, W., Dehm, G., & Pippan, R. (2008). A further step towards an understanding of size-dependent crystal plasticity: In situ tension experiments of miniaturized single-crystal copper samples. *Acta Materialia*, 56(3), 580-592. <https://doi.org/https://doi.org/10.1016/j.actamat.2007.10.015>
- Kiener, D., Motz, C., Schöberl, T., Jenko, M., & Dehm, G. (2006). Determination of Mechanical Properties of Copper at the Micron Scale [<https://doi.org/10.1002/adem.200600129>]. *Advanced Engineering Materials*, 8(11), 1119-1125. <https://doi.org/https://doi.org/10.1002/adem.200600129>
- Kim, J.-B., & Yoon, J. W. (2015). Necking behavior of AA 6022-T4 based on the crystal plasticity and damage models. *International Journal of Plasticity*, 73, 3-23. <https://doi.org/10.1016/j.ijplas.2015.06.013>
- Kocks, U. F. (1976). Laws for Work-Hardening and Low-Temperature Creep. *Journal of Engineering Materials and Technology*, 98(1), 76-85. <https://doi.org/10.1115/1.3443340>
- Kohlhoff, S., Gumbsch, P., & Fischmeister, H. F. (1991). Crack propagation in b.c.c. crystals studied with a combined finite-element and atomistic model. *Philosophical Magazine A*, 64(4), 851-878. <https://doi.org/10.1080/01418619108213953>
- Koumoulos, E. P., Jagadale, P., Lorenzi, A., Tagliaferro, A., & Charitidis, C. A. (2015). Evaluation of surface properties of epoxy-nanodiamonds composites. *Composites Part B: Engineering*, 80, 27-36. <https://doi.org/https://doi.org/10.1016/j.compositesb.2015.05.036>
- Kum, D. W., Oyama, T., Wadsworth, J., & Sherby, O. D. (1983). The impact properties of laminated composites containing ultrahigh carbon (UHC) steels. *Journal of the Mechanics and Physics of Solids*, 31(2), 173-186. [https://doi.org/https://doi.org/10.1016/0022-5096\(83\)90049-2](https://doi.org/https://doi.org/10.1016/0022-5096(83)90049-2)
- Kümmel, F., Kreuz, M., Hausöl, T., Höppel, H. W., & Göken, M. (2016). Microstructure and Mechanical Properties of Accumulative Roll-Bonded AA1050A/AA5005 Laminated Metal Composites. *Metals*, 6(3).
- Lai, X., Li, H., Li, C., Lin, Z., & Ni, J. (2008). Modelling and analysis of micro scale milling considering size effect, micro cutter edge radius and minimum chip thickness. *International Journal of Machine Tools and Manufacture*, 48(1), 1-14. <https://doi.org/https://doi.org/10.1016/j.ijmachtools.2007.08.011>
- Lai, Z., Peng, k., Gao, B., Mai, Y., & Jie, X. (2023). Achieving high strength and high electrical conductivity in Cu-Cr-Zr alloy by modifying shear banding during rolling. *Journal of Alloys and Compounds*, 958. <https://doi.org/10.1016/j.jallcom.2023.170402>

- Lele, S. P., & Anand, L. (2008). A small-deformation strain-gradient theory for isotropic viscoplastic materials. *Philosophical Magazine*, 88(30-32), 3655-3689. <https://doi.org/10.1080/14786430802087031>
- Lele, S. P., & Anand, L. (2009). A large-deformation strain-gradient theory for isotropic viscoplastic materials. *International Journal of Plasticity*, 25(3), 420-453. <https://doi.org/https://doi.org/10.1016/j.ijplas.2008.04.003>
- Li, J., & Soh, A. K. (2012). Modeling of the plastic deformation of nanostructured materials with grain size gradient. *International Journal of Plasticity*, 39, 88-102. <https://doi.org/https://doi.org/10.1016/j.ijplas.2012.06.004>
- Li, J., Wang, S., Mao, Q., Huang, Z., & Li, Y. (2019). Soft/hard copper/bronze laminates with superior mechanical properties. *Materials Science and Engineering: A*, 756, 213-218. <https://doi.org/https://doi.org/10.1016/j.msea.2019.04.069>
- Li, J., Weng, G. J., Chen, S., & Wu, X. (2017). On strain hardening mechanism in gradient nanostructures. *International Journal of Plasticity*, 88, 89-107. <https://doi.org/https://doi.org/10.1016/j.ijplas.2016.10.003>
- Li, S.-H., Zhao, Y., Radhakrishnan, J., & Ramamurty, U. (2022). A micropillar compression investigation into the plastic flow properties of additively manufactured alloys. *Acta Materialia*, 240, 118290. <https://doi.org/https://doi.org/10.1016/j.actamat.2022.118290>
- Li, W., Yuan, F., & Wu, X. (2015). Atomistic tensile deformation mechanisms of Fe with gradient nano-grained structure. *AIP Advances*, 5(8). <https://doi.org/10.1063/1.4928448>
- Li, X., Lu, L., Li, J., Zhang, X., & Gao, H. (2020). Mechanical properties and deformation mechanisms of gradient nanostructured metals and alloys. *Nature Reviews Materials*, 5(9), 706-723. <https://doi.org/10.1038/s41578-020-0212-2>
- Li, X., Zhao, J., Zhang, X., & Jiang, X. (2019). Revealing the inhibition mechanism of grain size gradient on crack growth in gradient nano-grained materials. *International Journal of Solids and Structures*, 172-173, 1-9. <https://doi.org/https://doi.org/10.1016/j.ijsolstr.2019.05.023>
- Liang, F., Luo, X.-M., & Zhang, G.-P. (2019). Interface-coupling-dependent mechanical behaviors of sandwich-structured Ni/Cu/Ni composites. *Materials Science and Engineering: A*, 743, 436-444. <https://doi.org/https://doi.org/10.1016/j.msea.2018.11.107>
- Liang, F., Tan, H.-F., Zhang, B., & Zhang, G.-P. (2017). Maximizing necking-delayed fracture of sandwich-structured Ni/Cu/Ni composites. *Scripta Materialia*, 134, 28-32. <https://doi.org/10.1016/j.scriptamat.2017.02.032>
- Liang, H., & Dunne, F. P. E. (2009). GND accumulation in bi-crystal deformation: Crystal plasticity analysis and comparison with experiments. *International Journal of Mechanical Sciences*, 51(4), 326-333. <https://doi.org/10.1016/j.ijmecsci.2009.03.005>
- Liang, W., & Zhou, M. (2004). Response of copper nanowires in dynamic tensile deformation. *Proceedings of the Institution of Mechanical Engineers, Part C: Journal of Mechanical Engineering Science*, 218(6), 599-606. <https://doi.org/10.1243/095440604774202231>
- Lin, P., Nie, J., & Liu, M. (2020). Study on irradiation effect in stress-strain response with CPFEM during nano-indentation. *Nuclear Materials and Energy*, 22, 100737. <https://doi.org/https://doi.org/10.1016/j.nme.2020.100737>
- Liu, B. X., Huang, L. J., Kaveendran, B., Geng, L., Cui, X. P., Wei, S. L., & Yin, F. X. (2017). Tensile and bending behaviors and characteristics of laminated Ti-(TiBw/Ti) composites with different interface status. *Composites Part B: Engineering*, 108, 377-385. <https://doi.org/10.1016/j.compositesb.2016.10.001>

-
- Liu, D., He, Y., Dunstan, D. J., Zhang, B., Gan, Z., Hu, P., & Ding, H. (2013). Toward a further understanding of size effects in the torsion of thin metal wires: An experimental and theoretical assessment. *International Journal of Plasticity*, 41, 30-52. <https://doi.org/https://doi.org/10.1016/j.ijplas.2012.08.007>
- Liu, D., He, Y., Tang, X., Ding, H., Hu, P., & Cao, P. (2012). Size effects in the torsion of microscale copper wires: Experiment and analysis. *Scripta Materialia*, 66(6), 406-409. <https://doi.org/https://doi.org/10.1016/j.scriptamat.2011.12.003>
- Liu, L.-Y., Yang, Q.-S., Liu, X., & Nian, X.-C. (2021). Crystal cracking of grain-gradient aluminum by a combined CPFEM-CZM method. *Engineering Fracture Mechanics*, 242. <https://doi.org/10.1016/j.engfracmech.2020.107507>
- Liu, L.-Y., Yang, Q.-S., Liu, X., & Shang, J.-J. (2021). Modeling damage evolution of graphene/aluminum composites considering crystal cracking and interface failure. *Composite Structures*, 267. <https://doi.org/10.1016/j.compstruct.2021.113863>
- Liu, Q., Fang, L., Xiong, Z., Yang, J., Tan, Y., Liu, Y., Zhang, Y., Tan, Q., Hao, C., Cao, L., Li, J., & Gao, Z. (2021). The response of dislocations, low angle grain boundaries and high angle grain boundaries at high strain rates. *Materials Science and Engineering: A*, 822, 141704. <https://doi.org/https://doi.org/10.1016/j.msea.2021.141704>
- Loukadakis, V., & Papaefthymiou, S. (2024). Advancements in and Applications of Crystal Plasticity Modelling of Metallic Materials. *Crystals*, 14(10). <https://doi.org/10.3390/cryst14100883>
- Lu, S., Kan, Q., Zhang, B., Yu, C., Kang, G., & Zhang, X. (2022). Size effect in nanoindentation: Taylor hardening or dislocation source-limited effect? *Materials Today Communications*, 33, 104580. <https://doi.org/https://doi.org/10.1016/j.mtcomm.2022.104580>
- Lu, S., Zhang, B., Li, X., Zhao, J., Zaiser, M., Fan, H., & Zhang, X. (2019). Grain boundary effect on nanoindentation: A multiscale discrete dislocation dynamics model. *Journal of the Mechanics and Physics of Solids*, 126, 117-135. <https://doi.org/https://doi.org/10.1016/j.jmps.2019.02.003>
- Lu, S., Zhao, J., Huang, M., Li, Z., Kang, G., & Zhang, X. (2022). Multiscale discrete dislocation dynamics study of gradient nano-grained materials. *International Journal of Plasticity*, 156, 103356. <https://doi.org/https://doi.org/10.1016/j.ijplas.2022.103356>
- Lu, W. Y., & Song, B. (2011). Quasi-Static Torsion Characterization of Micro-diameter Copper Wires. *Experimental Mechanics*, 51(5), 729-737. <https://doi.org/10.1007/s11340-010-9377-8>
- Lu, X., Zhang, X., Shi, M., Roters, F., Kang, G., & Raabe, D. (2019). Dislocation mechanism based size-dependent crystal plasticity modeling and simulation of gradient nano-grained copper. *International Journal of Plasticity*, 113, 52-73. <https://doi.org/https://doi.org/10.1016/j.ijplas.2018.09.007>
- Lu, X., Zhao, J., Wang, Z., Gan, B., Zhao, J., Kang, G., & Zhang, X. (2020). Crystal plasticity finite element analysis of gradient nanostructured TWIP steel. *International Journal of Plasticity*, 130, 102703. <https://doi.org/https://doi.org/10.1016/j.ijplas.2020.102703>
- Luan, Q., Xing, H., Zhang, J., & Jiang, J. (2020). Experimental and crystal plasticity study on deformation bands in single crystal and multi-crystal pure aluminium. *Acta Materialia*, 183, 78-92. <https://doi.org/10.1016/j.actamat.2019.11.006>
- Ma, E., & Zhu, T. (2017). Towards strength-ductility synergy through the design of heterogeneous nanostructures in metals. *Materials Today*, 20(6), 323-331. <https://doi.org/https://doi.org/10.1016/j.mattod.2017.02.003>
- Ma, H., Zhao, Y., Lyu, Z., Wang, X., Zhu, Y., & Gao, Y. (2023). What are the “dispersive shear bands” on the surfaces of layered heterostructured materials? *Journal of the Mechanics*

-
- and *Physics of Solids*, 181. <https://doi.org/10.1016/j.jmps.2023.105467>
- Ma, X., Huang, C., Moering, J., Ruppert, M., Höppel, H. W., Göken, M., Narayan, J., & Zhu, Y. (2016). Mechanical properties of copper/bronze laminates: Role of interfaces. *Acta Materialia*, 116, 43-52. <https://doi.org/https://doi.org/10.1016/j.actamat.2016.06.023>
- Ma, X. L., Huang, C. X., Xu, W. Z., Zhou, H., Wu, X. L., & Zhu, Y. T. (2015). Strain hardening and ductility in a coarse-grain/nanostructure laminate material. *Scripta Materialia*, 103, 57-60. <https://doi.org/https://doi.org/10.1016/j.scriptamat.2015.03.006>
- Mahato, J. K., De, P. S., Sarkar, A., Kundu, A., & Chakraborti, P. C. (2016). Effect of deformation mode and grain size on Bauschinger behavior of annealed copper. *International Journal of Fatigue*, 83, 42-52. <https://doi.org/10.1016/j.ijfatigue.2015.04.023>
- Marano, A., Gélébart, L., & Forest, S. (2019). Intragranular localization induced by softening crystal plasticity: Analysis of slip and kink bands localization modes from high resolution FFT-simulations results. *Acta Materialia*, 175, 262-275. <https://doi.org/10.1016/j.actamat.2019.06.010>
- Martínez-Pañeda, E., & Betegón, C. (2015). Modeling damage and fracture within strain-gradient plasticity. *International Journal of Solids and Structures*, 59, 208-215. <https://doi.org/https://doi.org/10.1016/j.ijsolstr.2015.02.010>
- McCabe, R. J., Capolungo, L., Marshall, P. E., Cady, C. M., & Tomé, C. N. (2010). Deformation of wrought uranium: Experiments and modeling. *Acta Materialia*, 58(16), 5447-5459. <https://doi.org/10.1016/j.actamat.2010.06.021>
- Mecking, H., & Kocks, U. F. (1981). Kinetics of flow and strain-hardening. *Acta Metallurgica*, 29(11), 1865-1875. [https://doi.org/https://doi.org/10.1016/0001-6160\(81\)90112-7](https://doi.org/https://doi.org/10.1016/0001-6160(81)90112-7)
- Meschut, G., Merklein, M., Brosius, A., Drummer, D., Fratini, L., Füssel, U., Gude, M., Homberg, W., Martins, P. A. F., Bobbert, M., Lechner, M., Kupfer, R., Gröger, B., Han, D., Kalich, J., Kappe, F., Kleffel, T., Köhler, D., Kuball, C. M., . . . Wolf, M. (2022). Review on mechanical joining by plastic deformation. *Journal of Advanced Joining Processes*, 5, 100113. <https://doi.org/https://doi.org/10.1016/j.jajp.2022.100113>
- Meyers, M. A., Mishra, A., & Benson, D. J. (2006). Mechanical properties of nanocrystalline materials. *Progress in Materials Science*, 51(4), 427-556. <https://doi.org/https://doi.org/10.1016/j.pmatsci.2005.08.003>
- Miller, R. E., Shilkrot, L. E., & Curtin, W. A. (2004). A coupled atomistics and discrete dislocation plasticity simulation of nanoindentation into single crystal thin films. *Acta Materialia*, 52(2), 271-284. <https://doi.org/https://doi.org/10.1016/j.actamat.2003.09.011>
- Molotnikov, A., Lapovok, R., Davies, C. H. J., Cao, W., & Estrin, Y. (2008). Size effect on the tensile strength of fine-grained copper. *Scripta Materialia*, 59(11), 1182-1185. <https://doi.org/https://doi.org/10.1016/j.scriptamat.2008.08.004>
- Murr, L. E. (2016). Dislocation Ledge Sources: Dispelling the Myth of Frank-Read Source Importance. *Metallurgical and Materials Transactions A*, 47(12), 5811-5826. <https://doi.org/10.1007/s11661-015-3286-5>
- Nie, J., Chen, Y., Song, L., Fan, Y., Cao, Y., Xie, K., Liu, S., Liu, X., Zhao, Y., & Zhu, Y. (2023). Enhancing strength and ductility of Al-matrix composite via a dual-heterostructure strategy. *International Journal of Plasticity*, 171. <https://doi.org/10.1016/j.ijplas.2023.103825>
- Noell, P. J., Carroll, J. D., & Boyce, B. L. (2018). The mechanisms of ductile rupture. *Acta Materialia*, 161, 83-98. <https://doi.org/10.1016/j.actamat.2018.09.006>
- Nye, J. F. (1953). Some geometrical relations in dislocated crystals. *Acta Metallurgica*, 1(2), 153-

-
162. [https://doi.org/https://doi.org/10.1016/0001-6160\(53\)90054-6](https://doi.org/https://doi.org/10.1016/0001-6160(53)90054-6)
- Nyung Lee, D., & Keun Kim, Y. (1988). Tensile properties of stainless steel-clad aluminium sandwich sheet metals. *Journal of Materials Science*, 23(4), 1436-1442. <https://doi.org/10.1007/BF01154614>
- Olfe, J., & Neuhäuser, H. (1988). Dislocation groups, multipoles, and friction stresses in α -CuZn alloys [<https://doi.org/10.1002/pssa.2211090115>]. *physica status solidi (a)*, 109(1), 149-160. <https://doi.org/https://doi.org/10.1002/pssa.2211090115>
- Peirce, D., Asaro, R. J., & Needleman, A. (1982). An analysis of nonuniform and localized deformation in ductile single crystals. *Acta Metallurgica*, 30(6), 1087-1119. [https://doi.org/https://doi.org/10.1016/0001-6160\(82\)90005-0](https://doi.org/https://doi.org/10.1016/0001-6160(82)90005-0)
- Peng, B., Jie, J., Sun, J., Liu, Q., Wang, X., Hang, Z., Ding, H., Muraishi, S., & Li, T. (2023). Synergistic deformation and fracture behavior of heterostructure Cu/1010 steel bimetal laminated composites. *Materials Science and Engineering: A*, 888. <https://doi.org/10.1016/j.msea.2023.145835>
- Peng, C., Zhan, Y., & Lou, J. (2012). Size-Dependent Fracture Mode Transition in Copper Nanowires [<https://doi.org/10.1002/smll.201101911>]. *Small*, 8(12), 1889-1894. <https://doi.org/https://doi.org/10.1002/smll.201101911>
- Peng, Y., Zhao, H., Sun, H., Yuan, M., Li, Z., Ouyang, Q., & Chen, J. a. (2024). Strain-gradient and damage failure behavior in particle reinforced heterogeneous matrix composites. *Engineering Fracture Mechanics*, 311. <https://doi.org/10.1016/j.engfracmech.2024.110548>
- Plimpton, S. (1995). Fast Parallel Algorithms for Short-Range Molecular Dynamics. *Journal of Computational Physics*, 117(1), 1-19. <https://doi.org/https://doi.org/10.1006/jcph.1995.1039>
- Qu, S., Huang, Y., Jiang, H., Liu, C., Wu, P. D., & Hwang, K. C. (2004). Fracture analysis in the conventional theory of mechanism-based strain gradient (MSG) plasticity. *International Journal of Fracture*, 129(3), 199-220. <https://doi.org/10.1023/B:FRAC.0000047786.40200.f8>
- Qu, S., Huang, Y., Pharr, G. M., & Hwang, K. C. (2006). The indentation size effect in the spherical indentation of iridium: A study via the conventional theory of mechanism-based strain gradient plasticity. *International Journal of Plasticity*, 22(7), 1265-1286. <https://doi.org/https://doi.org/10.1016/j.ijplas.2005.07.008>
- Quek, S. S., Wu, Z., Zhang, Y. W., & Srolovitz, D. J. (2014). Polycrystal deformation in a discrete dislocation dynamics framework. *Acta Materialia*, 75, 92-105. <https://doi.org/https://doi.org/10.1016/j.actamat.2014.04.063>
- Quey, R., Dawson, P. R., & Barbe, F. (2011). Large-scale 3D random polycrystals for the finite element method: Generation, meshing and remeshing. *Computer Methods in Applied Mechanics and Engineering*, 200(17-20), 1729-1745. <https://doi.org/10.1016/j.cma.2011.01.002>
- Ren, J., Zhang, Y., Zhao, D., Chen, Y., Guan, S., Liu, Y., Liu, L., Peng, S., Kong, F., Poplawsky, J. D., Gao, G., Voisin, T., An, K., Wang, Y. M., Xie, K. Y., Zhu, T., & Chen, W. (2022). Strong yet ductile nanolamellar high-entropy alloys by additive manufacturing. *Nature*, 608(7921), 62-68. <https://doi.org/10.1038/s41586-022-04914-8>
- Romero-Resendiz, L., El-Tahawy, M., Zhang, T., Rossi, M. C., Marulanda-Cardona, D. M., Yang, T., Amigó-Borrás, V., Huang, Y., Mirzadeh, H., Beyerlein, I. J., Huang, J. C., Langdon, T. G., & Zhu, Y. T. (2022). Heterostructured stainless steel: Properties, current trends, and future perspectives. *Materials Science and Engineering: R: Reports*, 150, 100691. <https://doi.org/https://doi.org/10.1016/j.mser.2022.100691>
- Romero-Resendiz, L., Naeem, M., & Zhu, Y. T. (2023). Heterostructured Materials by Severe

-
- Plastic Deformation: Overview and Perspectives. *MATERIALS TRANSACTIONS*, 64(10), 2346-2360. <https://doi.org/10.2320/matertrans.MT-MF2022010>
- Roters, F., Eisenlohr, P., Hantcherli, L., Tjahjanto, D. D., Bieler, T. R., & Raabe, D. (2010). Overview of constitutive laws, kinematics, homogenization and multiscale methods in crystal plasticity finite-element modeling: Theory, experiments, applications. *Acta Materialia*, 58(4), 1152-1211. <https://doi.org/10.1016/j.actamat.2009.10.058>
- Roters, F., Eisenlohr, P., Kords, C., Tjahjanto, D. D., Diehl, M., & Raabe, D. (2012). DAMASK: the Düsseldorf Advanced MATERIAL Simulation Kit for studying crystal plasticity using an FE based or a spectral numerical solver. *Procedia IUTAM*, 3, 3-10. <https://doi.org/https://doi.org/10.1016/j.piutam.2012.03.001>
- Sakharova, N. A., Fernandes, J. V., Antunes, J. M., & Oliveira, M. C. (2009). Comparison between Berkovich, Vickers and conical indentation tests: A three-dimensional numerical simulation study. *International Journal of Solids and Structures*, 46(5), 1095-1104. <https://doi.org/https://doi.org/10.1016/j.ijsolstr.2008.10.032>
- Sedighiani, K., Traka, K., Roters, F., Sietsma, J., Raabe, D., & Diehl, M. (2022). Crystal plasticity simulation of in-grain microstructural evolution during large deformation of IF-steel. *Acta Materialia*, 237. <https://doi.org/10.1016/j.actamat.2022.118167>
- Semiatin, S. L., & Piehler, H. R. (1979). Deformation of sandwich sheet materials in uniaxial tension. *Metallurgical Transactions A*, 10(1), 85-96. <https://doi.org/10.1007/BF02686411>
- Sinclair, C. W., Poole, W. J., & Bréchet, Y. (2006). A model for the grain size dependent work hardening of copper. *Scripta Materialia*, 55(8), 739-742. <https://doi.org/https://doi.org/10.1016/j.scriptamat.2006.05.018>
- Starink, M. J., & Wang, S. C. (2003). A model for the yield strength of overaged Al-Zn-Mg-Cu alloys. *Acta Materialia*, 51(17), 5131-5150. [https://doi.org/https://doi.org/10.1016/S1359-6454\(03\)00363-X](https://doi.org/https://doi.org/10.1016/S1359-6454(03)00363-X)
- Stinville, J. C., Charpagne, M. A., Maaß, R., Proudhon, H., Ludwig, W., Callahan, P. G., Wang, F., Beyerlein, I. J., Echlin, M. P., & Pollock, T. M. (2023). Insights into Plastic Localization by Crystallographic Slip from Emerging Experimental and Numerical Approaches. *Annual Review of Materials Research*, 53(Volume 53, 2023), 275-317. <https://doi.org/https://doi.org/10.1146/annurev-matsci-080921-102621>
- Tadmor, E. B., Ortiz, M., & Phillips, R. (1996). Quasicontinuum analysis of defects in solids. *Philosophical Magazine A*, 73(6), 1529-1563. <https://doi.org/10.1080/01418619608243000>
- Tang, D., Zhao, L., Wang, H., Li, D., Peng, Y., & Wu, P. (2021). The role of rough surface in the size-dependent behavior upon nano-indentation. *Mechanics of Materials*, 157, 103836. <https://doi.org/https://doi.org/10.1016/j.mechmat.2021.103836>
- Tarleton, E., Balint, D. S., Gong, J., & Wilkinson, A. J. (2015). A discrete dislocation plasticity study of the micro-cantilever size effect. *Acta Materialia*, 88, 271-282. <https://doi.org/10.1016/j.actamat.2015.01.030>
- Taylor, G. I. (1997). The mechanism of plastic deformation of crystals. Part I. – Theoretical. *Proceedings of the Royal Society of London. Series A, Containing Papers of a Mathematical and Physical Character*, 145(855), 362-387. <https://doi.org/10.1098/rspa.1934.0106>
- Thompson, A. P., Aktulga, H. M., Berger, R., Bolintineanu, D. S., Brown, W. M., Crozier, P. S., in 't Veld, P. J., Kohlmeyer, A., Moore, S. G., Nguyen, T. D., Shan, R., Stevens, M. J., Tranchida, J., Trott, C., & Plimpton, S. J. (2022). LAMMPS - a flexible simulation tool for particle-based materials modeling at the atomic, meso, and continuum scales. *Computer Physics Communications*, 271, 108171. <https://doi.org/https://doi.org/10.1016/j.cpc.2021.108171>

- Tvergaard, V., Huang, Y., & Hutchinson, J. W. (1990). *Cavitation instabilities in a power hardening elastic-plastic solid*. Department of Solid Mechanics, Technical University of Denmark.
- Valiev, R. Z., Straumal, B., & Langdon, T. G. (2022). Using Severe Plastic Deformation to Produce Nanostructured Materials with Superior Properties. *Annual Review of Materials Research*, 52(1), 357-382. <https://doi.org/10.1146/annurev-matsci-081720-123248>
- Voyiadjis, G. Z., & Song, Y. (2019). Strain gradient continuum plasticity theories: Theoretical, numerical and experimental investigations. *International Journal of Plasticity*, 121, 21-75. <https://doi.org/https://doi.org/10.1016/j.ijplas.2019.03.002>
- Voyiadjis, G. Z., & Song, Y. (2020). Chapter 4 - Review of numerical approaches using the gradient-enhanced continuum plasticity. In G. Z. Voyiadjis & Y. Song (Eds.), *Gradient-Enhanced Continuum Plasticity* (pp. 95-122). Elsevier. <https://doi.org/https://doi.org/10.1016/B978-0-12-817766-2.00004-8>
- Wagner, G. J., & Liu, W. K. (2003). Coupling of atomistic and continuum simulations using a bridging scale decomposition. *Journal of Computational Physics*, 190(1), 249-274. [https://doi.org/https://doi.org/10.1016/S0021-9991\(03\)00273-0](https://doi.org/https://doi.org/10.1016/S0021-9991(03)00273-0)
- Wagner, P., Engler, O., & Lücke, K. (1995). Formation of Cu-type shear bands and their influence on deformation and texture of rolled f.c.c. {112} <111> single crystals. *Acta Metallurgica et Materialia*, 43(10), 3799-3812. [https://doi.org/https://doi.org/10.1016/0956-7151\(95\)90164-7](https://doi.org/https://doi.org/10.1016/0956-7151(95)90164-7)
- Wang, D., Liu, L., Deng, G., Deng, C., Bai, Y., Yang, Y., Wu, W., Chen, J., Liu, Y., Wang, Y., Lin, X., & Han, C. (2022). Recent progress on additive manufacturing of multi-material structures with laser powder bed fusion. *Virtual and Physical Prototyping*, 17(2), 329-365. <https://doi.org/10.1080/17452759.2022.2028343>
- Wang, H., You, Z., & Lu, L. (2018). Kinematic and isotropic strain hardening in copper with highly aligned nanoscale twins. *Materials Research Letters*, 6(6), 333-338. <https://doi.org/10.1080/21663831.2018.1455752>
- Wang, K., Sun, Y., Yu, H., Huang, Y., Su, S., Ning, Z., Cheng, Z., Fu, W., Sun, J., & Liaw, P. K. (2022). Microstructure evolution and mechanical behavior of a CoCrFeNiMn0.75Cu0.25 high-entropy alloy by thermo-mechanical treatment. *Materials Science and Engineering: A*, 860. <https://doi.org/10.1016/j.msea.2022.144274>
- Wang, S., Chen, Z., & Dong, C. (2017). Tearing failure of ultra-thin sheet-metal involving size effect in blanking process: Analysis based on modified GTN model. *International Journal of Mechanical Sciences*, 133, 288-302. <https://doi.org/https://doi.org/10.1016/j.ijmecsci.2017.08.028>
- Wang, X.-b. (2007). Adiabatic Shear Localization for Steels Based on Johnson-Cook Model and Second- and Fourth-Order Gradient Plasticity Models. *Journal of Iron and Steel Research, International*, 14(5), 56-61. [https://doi.org/https://doi.org/10.1016/S1006-706X\(07\)60075-2](https://doi.org/https://doi.org/10.1016/S1006-706X(07)60075-2)
- Wang, X., Ma, Y., Shen, Z., Gu, Y., Zhang, D., Qiu, T., & Liu, H. (2015). Size effects on formability in microscale laser dynamic forming of copper foil. *Journal of Materials Processing Technology*, 220, 173-183. <https://doi.org/https://doi.org/10.1016/j.jmatprotec.2015.01.020>
- Wang, Y., Huang, C., Li, Y., Guo, F., He, Q., Wang, M., Wu, X., Scattergood, R. O., & Zhu, Y. (2020). Dense dispersed shear bands in gradient-structured Ni. *International Journal of Plasticity*, 124, 186-198. <https://doi.org/https://doi.org/10.1016/j.ijplas.2019.08.012>
- Wang, Y., Huang, C., Li, Z., Fang, X., Wang, M., He, Q., Guo, F., & Zhu, Y. (2020). Shear band stability and uniform elongation of gradient structured material: Role of lateral

-
- constraint. *Extreme Mechanics Letters*, 37. <https://doi.org/10.1016/j.eml.2020.100686>
- Wang, Y., Yang, G., Wang, W., Wang, X., Li, Q., & Wei, Y. (2017). Optimal stress and deformation partition in gradient materials for better strength and tensile ductility: A numerical investigation. *Sci Rep*, 7(1), 10954. <https://doi.org/10.1038/s41598-017-10941-7>
- Wang, Y., Yang, M., Ma, X., Wang, M., Yin, K., Huang, A., & Huang, C. (2018). Improved back stress and synergetic strain hardening in coarse-grain/nanostructure laminates. *Materials Science and Engineering: A*, 727, 113-118. <https://doi.org/10.1016/j.msea.2018.04.107>
- Wang, Y. F., Huang, C. X., He, Q., Guo, F. J., Wang, M. S., Song, L. Y., & Zhu, Y. T. (2019). Heterostructure induced dispersive shear bands in heterostructured Cu. *Scripta Materialia*, 170, 76-80. <https://doi.org/10.1016/j.scriptamat.2019.05.036>
- Wang, Y. F., Wang, M. S., Fang, X. T., Guo, F. J., Liu, H. Q., Scattergood, R. O., Huang, C. X., & Zhu, Y. T. (2019). Extra strengthening in a coarse/ultrafine grained laminate: Role of gradient interfaces. *International Journal of Plasticity*, 123, 196-207. <https://doi.org/10.1016/j.ijplas.2019.07.019>
- Wang, Z., Zhang, H., Li, Z., Li, G., Zhang, J., Zhang, J., Hassan, H. u., Yan, Y., Hartmaier, A., & Sun, T. (2019). Crystal plasticity finite element simulation and experiment investigation of nanoscratching of single crystalline copper. *Wear*, 430-431, 100-107. <https://doi.org/10.1016/j.wear.2019.04.024>
- Woo, W., Em, V. T., Kim, E. Y., Han, S. H., Han, Y. S., & Choi, S. H. (2012). Stress-strain relationship between ferrite and martensite in a dual-phase steel studied by in situ neutron diffraction and crystal plasticity theories. *Acta Materialia*, 60(20), 6972-6981. <https://doi.org/10.1016/j.actamat.2012.08.054>
- Wu, H., Xu, W., Shan, D., Wang, X., Guo, B., & Jin, B. C. (2023). Micromechanical modeling of damage evolution and fracture behavior in particle reinforced metal matrix composites based on the conventional theory of mechanism-based strain gradient plasticity. *Journal of Materials Research and Technology*, 22, 625-641. <https://doi.org/10.1016/j.jmrt.2022.11.139>
- Wu, Q., & Zikry, M. A. (2015). Dynamic fracture predictions of microstructural mechanisms and characteristics in martensitic steels. *Engineering Fracture Mechanics*, 145, 54-66. <https://doi.org/10.1016/j.engfracmech.2015.06.002>
- Wu, X., Jiang, P., Chen, L., Yuan, F., & Zhu, Y. T. (2014). Extraordinary strain hardening by gradient structure. *Proceedings of the National Academy of Sciences*, 111(20), 7197-7201. <https://doi.org/10.1073/pnas.1324069111>
- Wu, X., & Zhu, Y. (2017). Heterogeneous materials: a new class of materials with unprecedented mechanical properties. *Materials Research Letters*, 5(8), 527-532. <https://doi.org/10.1080/21663831.2017.1343208>
- Wu, X., Zhu, Y., & Lu, K. (2020). Ductility and strain hardening in gradient and lamellar structured materials. *Scripta Materialia*, 186, 321-325. <https://doi.org/10.1016/j.scriptamat.2020.05.025>
- Wu, X. L., Jiang, P., Chen, L., Zhang, J. F., Yuan, F. P., & Zhu, Y. T. (2014). Synergetic Strengthening by Gradient Structure. *Materials Research Letters*, 2(4), 185-191. <https://doi.org/10.1080/21663831.2014.935821>
- Wu, Y., Shen, Y., Chen, K., Yu, Y., He, G., & Wu, P. (2017). Multi-scale crystal plasticity finite element method (CPFEM) simulations for shear band development in aluminum alloys. *Journal of Alloys and Compounds*, 711, 495-505. <https://doi.org/10.1016/j.jallcom.2017.03.333>
- Wu, Y., Shen, Y., Wu, P., Chen, K., Yu, Y., & He, G. (2016). A two-step approach to predict

-
- shear band development with crystal plasticity finite element method (CPFEM). *International Journal of Solids and Structures*, 96, 265-273. <https://doi.org/10.1016/j.ijsolstr.2016.06.003>
- Wulfinghoff, S., & Böhlke, T. (2015). Gradient crystal plasticity including dislocation-based work-hardening and dislocation transport. *International Journal of Plasticity*, 69, 152-169. <https://doi.org/10.1016/j.ijplas.2014.12.003>
- Xi, N., Ni, Z., Liu, P., Zhou, Y., Fang, X., Chen, Z., & Huang, K. (2024). Prediction of low-cycle fatigue properties of additive manufactured IN718 by crystal plasticity modelling incorporating effects from crystallographic orientations and defects. *Virtual and Physical Prototyping*, 19(1). <https://doi.org/10.1080/17452759.2024.2328266>
- Xia, Y., Bai, X., Fang, H., Li, X., Ni, X., Wu, H., Miao, K., Li, R., Xie, H., Wu, H., Geng, L., & Fan, G. (2024). Effects of local strain on the plastic deformation and fracture mechanism of heterogeneous multilayered aluminum. *International Journal of Plasticity*, 180. <https://doi.org/10.1016/j.ijplas.2024.104078>
- Xiao, M., Yao, J., & Huang, C. (2024). Fracture Model of Al-Cu Alloys with Gradient Crystals Based on Crystal Plasticity. *Metals*, 14(6). <https://doi.org/10.3390/met14060694>
- Xu, A., Saleh, M., Davis, J., Edwards, L., & Bhattacharyya, D. (2018). In-situ micro-tensile investigation of strain rate response along <100> and <110> directions in single crystal nickel. *International Journal of Plasticity*, 106, 129-144. <https://doi.org/https://doi.org/10.1016/j.ijplas.2018.03.005>
- Yan, Y., Sumigawa, T., Wang, X., Chen, W., Xuan, F., & Kitamura, T. (2020). Fatigue curve of microscale single-crystal copper: An in situ SEM tension-compression study. *International Journal of Mechanical Sciences*, 171, 105361. <https://doi.org/https://doi.org/10.1016/j.ijmecsci.2019.105361>
- Yang, M., Pan, Y., Yuan, F., Zhu, Y., & Wu, X. (2016). Back stress strengthening and strain hardening in gradient structure. *Materials Research Letters*, 4(3), 145-151. <https://doi.org/10.1080/21663831.2016.1153004>
- Yu, W. X., Liu, B. X., Cui, X. P., Dong, Y. C., Zhang, X., He, J. N., Chen, C. X., & Yin, F. X. (2018). Revealing extraordinary strength and toughness of multilayer TWIP/Maraging steels. *Materials Science and Engineering: A*, 727, 70-77. <https://doi.org/10.1016/j.msea.2018.04.097>
- Yu, W. X., Liu, B. X., He, J. N., Chen, C. X., Fang, W., & Yin, F. X. (2019). Microstructure characteristics, strengthening and toughening mechanism of rolled and aged multilayer TWIP/maraging steels. *Materials Science and Engineering: A*, 767. <https://doi.org/10.1016/j.msea.2019.138426>
- Yu, W. X., Liu, B. X., Zhao, J. F., Lin, Z. M., Zheng, S. J., Yin, F. X., & Hu, N. (2024). Improving ductility of multilayer TWIP/Maraging steel through shear band delocalization and periodic multiple necking controlled by layer thickness. *Scripta Materialia*, 241. <https://doi.org/10.1016/j.scriptamat.2023.115865>
- Yuan, F., Yan, D., Sun, J., Zhou, L., Zhu, Y., & Wu, X. (2019). Ductility by shear band delocalization in the nano-layer of gradient structure. *Materials Research Letters*, 7(1), 12-17. <https://doi.org/10.1080/21663831.2018.1546238>
- Yuan, R., & Du, H. (2020). Modeling the effects of interface spacing on the mechanical properties of heterogeneous laminates. *Computational Materials Science*, 173, 109391. <https://doi.org/https://doi.org/10.1016/j.commatsci.2019.109391>
- Zeng, Z., Li, X., Xu, D., Lu, L., Gao, H., & Zhu, T. (2016). Gradient plasticity in gradient nano-grained metals. *Extreme Mechanics Letters*, 8, 213-219. <https://doi.org/10.1016/j.eml.2015.12.005>
- Zha, C., Hu, J., Li, A., Huang, S., Liu, H., Chen, G., Zhang, Z., Li, B., & Wang, Z. (2019).

-
- Nanoindentation study on mechanical properties and curing depth of dental resin nanocomposites [<https://doi.org/10.1002/pc.24886>]. *Polymer Composites*, 40(4), 1473-1480. <https://doi.org/https://doi.org/10.1002/pc.24886>
- Zhang, F., Huang, Y., Hwang, K. C., Qu, S., & Liu, C. (2007). A Three-Dimensional Strain Gradient Plasticity Analysis of Particle Size Effect in Composite Materials. *Materials and Manufacturing Processes*, 22(2), 140-148. <https://doi.org/10.1080/10426910601062032>
- Zhang, H., Ding, Y., Li, R., & Gao, Y. (2024). Enhanced strength-ductility synergy and activation of non-basal slip in as-extruded Mg-Zn-Ca alloy via heterostructure. *Journal of Materials Research and Technology*, 28, 1841-1851. <https://doi.org/10.1016/j.jmrt.2023.12.127>
- Zhang, M., Bridier, F., Villechaise, P., Mendez, J., & McDowell, D. L. (2010). Simulation of slip band evolution in duplex Ti-6Al-4V. *Acta Materialia*, 58(3), 1087-1096. <https://doi.org/10.1016/j.actamat.2009.10.025>
- Zhang, S., Liu, W., Wan, J., Misra, R. D. K., Wang, Q., & Wang, C. (2020). The grain size and orientation dependence of geometrically necessary dislocations in polycrystalline aluminum during monotonic deformation: Relationship to mechanical behavior. *Materials Science and Engineering: A*, 775. <https://doi.org/10.1016/j.msea.2020.138939>
- Zhang, X., Gui, Y., Lai, M., Lu, X., Gu, J., Wang, F., Yang, T., Wang, Z., & Song, M. (2023). Enhanced strength-ductility synergy of medium-entropy alloys via multiple level gradient structures. *International Journal of Plasticity*, 164. <https://doi.org/10.1016/j.ijplas.2023.103592>
- Zhang, X., Zhao, J., Kang, G., & Zaiser, M. (2023). Geometrically necessary dislocations and related kinematic hardening in gradient grained materials: A nonlocal crystal plasticity study. *International Journal of Plasticity*, 163, 103553. <https://doi.org/https://doi.org/10.1016/j.ijplas.2023.103553>
- Zhang, Y., Chen, H., Jia, Y.-F., Li, D.-F., Yuan, G.-J., Zhang, X.-C., & Tu, S.-T. (2021). A modified kinematic hardening model considering hetero-deformation induced hardening for bimodal structure based on crystal plasticity. *International Journal of Mechanical Sciences*, 191. <https://doi.org/10.1016/j.ijmecsci.2020.106068>
- Zhang, Y., Cheng, Z., Lu, L., & Zhu, T. (2020). Strain gradient plasticity in gradient structured metals. *Journal of the Mechanics and Physics of Solids*, 140, 103946. <https://doi.org/https://doi.org/10.1016/j.jmps.2020.103946>
- Zhang, Y., Cheng, Z., Zhu, T., & Lu, L. (2024). Mechanics of gradient nanostructured metals. *Journal of the Mechanics and Physics of Solids*. <https://doi.org/10.1016/j.jmps.2024.105719>
- Zhang, Y., He, C.-Y., Wang, X., Hama, T., Sun, B., Jia, Y.-F., Zhang, X.-C., & Tu, S.-T. (2024). Revealing the fatigue strengthening and damage mechanisms of surface-nanolaminated gradient structure. *International Journal of Plasticity*, 104128. <https://doi.org/https://doi.org/10.1016/j.ijplas.2024.104128>
- Zhang, Y. B., Song, S. J., & Liu, F. (2022). Thermo-kinetic orientation study on interface behavior of polycrystalline Cu-Nb composite by crystal plasticity finite element method. *Materials & Design*, 223. <https://doi.org/10.1016/j.matdes.2022.111215>
- Zhang, Y. B., Song, S. J., & Liu, F. (2024). Thermo-kinetic characteristics on stabilizing hetero-phase interface of metal matrix composites by crystal plasticity finite element method. *Journal of Materials Science & Technology*, 169, 53-67. <https://doi.org/10.1016/j.jmst.2023.06.012>
- Zhang, Z., Shen, F., & Ke, L.-L. (2024). A dislocation density-based crystal plasticity damage model for rolling contact fatigue of gradient grained structures. *International Journal*

-
- of Fatigue*, 179. <https://doi.org/10.1016/j.jifatigue.2023.108038>
- Zhang, Z., Wei, M., & Zhai, T. (2024). Mesoscale study of fatigue damage evolution of polycrystalline Al alloy based on crystal plasticity finite element method coupled with continuum damage mechanics. *Applied Physics A*, 130(11). <https://doi.org/10.1007/s00339-024-07948-z>
- Zhao, J., Kan, Q., Zhou, L., Kang, G., Fan, H., & Zhang, X. (2019). Deformation mechanisms based constitutive modelling and strength-ductility mapping of gradient nano-grained materials. *Materials Science and Engineering: A*, 742, 400-408. <https://doi.org/https://doi.org/10.1016/j.msea.2018.10.096>
- Zhao, J., Liu, B., Wang, Y., Liang, Y., Li, J., & Zhang, X. (2023). Dispersed strain bands promote the ductility of gradient nano-grained material: A strain gradient constitutive modeling considering damage effect. *Mechanics of Materials*, 179, 104599. <https://doi.org/https://doi.org/10.1016/j.mechmat.2023.104599>
- Zhao, J., Lu, X., Liu, J., Bao, C., Kang, G., Zaiser, M., & Zhang, X. (2021). The tension-compression behavior of gradient structured materials: A deformation-mechanism-based strain gradient plasticity model. *Mechanics of Materials*, 159, 103912. <https://doi.org/https://doi.org/10.1016/j.mechmat.2021.103912>
- Zhao, J., Lu, X., Yuan, F., Kan, Q., Qu, S., Kang, G., & Zhang, X. (2020). Multiple mechanism based constitutive modeling of gradient nanograined material. *International Journal of Plasticity*, 125, 314-330. <https://doi.org/https://doi.org/10.1016/j.ijplas.2019.09.018>
- Zhao, J., Zaiser, M., Lu, X., Zhang, B., Huang, C., Kang, G., & Zhang, X. (2021). Size-dependent plasticity of hetero-structured laminates: A constitutive model considering deformation heterogeneities. *International Journal of Plasticity*, 145, 103063. <https://doi.org/https://doi.org/10.1016/j.ijplas.2021.103063>
- Zhao, Y., Wang, T., Gao, B., Gao, Z., Han, J., Zhang, S., & Huang, Q. (2022). Towards enhanced strength-ductility in pure copper by fabricating hetero grain composite laminates. *Journal of Alloys and Compounds*, 928, 167192. <https://doi.org/https://doi.org/10.1016/j.jallcom.2022.167192>
- Zhao, Y., Zhu, Y., Liao, X., Horita, Z., & Langdon, T. G. (2006). Tailoring stacking fault energy for high ductility and high strength in ultrafine grained Cu and its alloy. *Applied Physics Letters*, 89, 121906.
- Zheng, J.-Y., Ran, J. Q., & Fu, M. W. (2022). Constitutive modeling of multiscale polycrystals considering grain structures and orientations. *International Journal of Mechanical Sciences*, 216. <https://doi.org/10.1016/j.ijmecsci.2021.106992>
- Zhou, Z., Li, J., Mao, Q., Yue, Y., Wang, S., & Li, Y. (2023). Heterostructured copper-brass laminates with gradient transition layer. *Journal of Materials Research and Technology*, 23, 5534-5546. <https://doi.org/10.1016/j.jmrt.2023.02.161>
- Zhou, Z., Li, J., Wang, Y., Mao, Q., Liu, Y., Yue, Y., Huang, C., & Li, Y. (2024). Effects of mechanical heterogeneity and dislocation storage capacity on the strength-ductility synergy of heterostructured laminates. *Materials Science and Engineering: A*, 896. <https://doi.org/10.1016/j.msea.2024.146281>
- Zhou, Z., Wang, Y., Li, J., Mao, Q., Liu, Y., Yue, Y., & Li, Y. (2024). Origins of HDI stress in copper-brass laminates with dual-heterostructured interfaces. *Materials Characterization*, 210. <https://doi.org/10.1016/j.matchar.2024.113852>
- Zhu, Y., & Wu, X. (2023). Heterostructured materials. *Progress in Materials Science*, 131, 101019. <https://doi.org/https://doi.org/10.1016/j.pmatsci.2022.101019>